The Effect of Blade Aeroelasticity and Turbine Parameters on Wind Turbine Noise

Daniel Wu

Thesis submitted to the Faculty of the Virginia Polytechnic Institute and State University in partial fulfillment of the requirements for the degree of

Master of Science
in
Mechanical Engineering

Ricardo A. Burdisso, Chair
Pablo Tarazaga
Corina Sandu

July 10th 2017
Blacksburg, Virginia

Keywords: wind turbine noise, aeroelastic blade, flexible blade, outdoor sound propagation

The Effect of Blade Aeroelasticity and Turbine Parameters on Wind Turbine Noise

Daniel Wu

Abstract

In recent years, the demand for wind energy has dramatically increased as well as the number and size of commercial wind turbines. These large turbines are loud and can cause annoyance to nearby communities. Therefore, the prediction of large wind turbine noise over long distances is critical. The wind turbine noise prediction is a very complex problem since it has to account for atmospheric conditions (wind and temperature), ground absorption, un-even terrain, turbine wake, and blade deformation. In these large turbines, the blade deflection is significant and it can potentially influence the noise emissions. However, the effects of blade flexibility on turbine noise predictions have not been addressed yet, i.e. all previous research efforts have assumed rigid blades. To address this shortcoming, the present work merges a wind turbine aeroelastic code, FAST (Fatigue, Aerodynamics, Structures, and Turbulence) to a wind turbine noise code, WTNoise, to compute turbine noise accounting for blade aeroelasticity. Using the newly developed simulation tool, the effects flexible blades on wind turbine noise are investigated, as well as the effects of turbine parameters, e.g. wind conditions, rotor size, tilt, yaw, and pre-cone angles. The acoustic results are shown as long term average overall sound power level distribution over the rotor, ground noise map over a large flat terrain, and noise spectrum at selected locations downwind. To this end, two large wind turbines are modeled. The first one is the NREL 5MW turbine that has a rotor diameter of 126 m. The second wind turbine, the Sandia 13.2MW, has a rotor diameter of 206 m. The results show that the wind condition has strong effects on the noise propagation over long distances, primarily in the upwind direction. In general, the turbine parameters have no significant effects on the average noise level. However, the turbine yaw impacts significantly the turbine noise footprint by affecting the noise propagation paths. The rotor size is also a dominating factor in the turbine noise level. Finally, the blade aeroelasticity has minor effects on the turbine noise. In summary, a comprehensive tool for wind turbine noise prediction including blade aeroelasticity was developed and it was used to address its impact on modern large turbine noise emissions.

The Effect of Blade Aeroelasticity and Turbine Parameters on Wind Turbine Noise

Daniel Wu

General Audience Abstract

Large wind turbines provide sustainable renewable energy but create loud noise that causes annoyance to nearby communities. Therefore, the prediction of large wind turbine noise is critical, but a complex problem, especially for the propagation over a long distance. The noise prediction needs to account for the turbine design, atmospheric factors, terrain, and airflow. Furthermore, in these large turbines, the blade deflection is significant and it can potentially influence the noise prediction. The present work addresses the above factors in the wind turbine noise prediction by merging a wind turbine structural code, FAST (Fatigue, Aerodynamics, Structures, and Turbulence) to a wind turbine noise code, WTNoise, to compute turbine noise accounting for blade deflection. Two turbines that have rotor diameter larger than 100 m were modeled and studied under different wind turbine design specifications, wind conditions, and blade deflection assumptions. The results showed that the rotor size is one of the dominating factor of turbine noise level. The blade deflection only has minor effects on the turbine noise. In summary, a comprehensive tool for wind turbine noise prediction including blade deflection was developed and used to address its impact on modern large turbine noise emissions.

Acknowledgement

I would like to start expressing my gratitude to Dr. Ricardo Burdisso, Professor in the Mechanical Engineering Department, Virginia Tech, who has been my advisor since the beginning of my graduate studies. His guidance and support allowed me to develop my research skills and autonomy. The present work would not have been possible without his patience and constructive suggestions.

I also wish to express my appreciation to Dr. Pablo Tarazaga and Dr. Corina Sandu in the Mechanical Engineering Department, Virginia Tech, who integrated my committee. Their courses in vibration and multibody dynamics provided tremendous helps in the present work. In addition, they made many valuable suggestions and gave constructive advice.

Kind acknowledgements are extended to the National Renewable Energy Laboratory (NREL) and Sandia National Laboratories that provided wind turbine models with great details on their designs and structural properties. The collaboration of Dr. Jason Jonkman who provided the code FAST is also gratefully acknowledged.

Many friends have provided help and support. My appreciation goes to all my fellow graduate students of the Vibrations and Acoustics Laboratory, Virginia Tech. I am especially indebted to Mr. Sterling McBride who provided me of valuable guidance based on his rich experience and knowledge in the wind turbine noise and propagation. I am also grateful to Mr. Mark Hurtado for his friendship and help.

Finally, I want to thank to my family. This thesis would not have been possible without their help and support.

Table of contents

List of Figures

List of Tables

1. Introduction

This section discusses the motivations, literature review, objectives, and structure of this thesis.

1.1 Motivation

The development in wind energy industry is expanding rapidly around the world as one of the main sources of renewable energy. In 2015, wind energy supplied 4.7% of the total electricity in the U.S. and the Department of Energy targets to increase this percentage to 20% by 2030 [1]. To achieve higher yield from wind energy, the size of commercial wind turbines has increased dramatically in the last 25 years as shown in Figure 1. One of the examples is the Haliade 150-6MW wind turbine developed by General Electric (GE). It has a rotor diameter of 150 m with the hub height at 100 m. GE has installed multiple units in a wind farm at Block Island, located off the coast of Rhode Island as shown in Figure 2. This 30 MW project is expected to generate enough power to meet the needs of the island residents. There are even larger wind turbine in Europe, such as Vestas V164 and Adwan AD 8-180 which have rotor diameter 164 m and 180 m, respectively. More wind turbines with larger rotor diameter are under development, such as the 205 m diameter rotor for the Sandia 13.2 MW[2], 252 m diameter rotor for and upwind 20MW turbine from Netherlands Energy Research Centre [3], and 400+ m rotor diameter for the Sandia 50MW turbine [4]. Table 1 shows some example of three-bladed large horizontal axis wind turbines that are in testing or service.

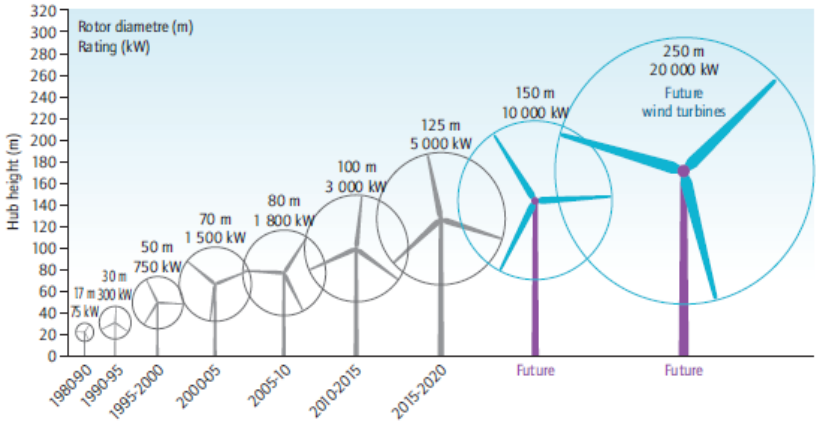

Figure 1: Wind turbine development trend [5].

Figure 2: The GE Wind Turbine in the Block Island wind farm project [6].

Table 1: Examples of Large Wind Turbines.

Model	***Rotor Diameter, m***	***Power Rating, MW***	***Status***
MHI Vestas V164	164	8.00	In Service
Adwen AD-180	180	8.00	Prototype Testing
Siemens SWT-8.0-154	154	8.00	Prototype Testing
Haliade 150	150.8	6.00	In Service

This progression on large wind turbines led to improvements of the wind turbine modeling accuracy on their aerodynamics and structural responses. The aerodynamics of wind turbines provide predictions on their power outputs, flow conditions, and aerodynamic loads on the blades. The aerodynamic loads on large wind turbines often lead to large blade deformation. Therefore, structural responses of wind turbines become a critical concern in wind turbine design. The structural wind turbine modeling must accurately predict the blade deformations and blade dynamic responses to yield a successful wind turbine design. Many of the open-resource wind turbine simulation tools are developed to address the above issues. For example, FAST (Fatigue, Aerodynamics, Structures, and Turbulence) is an aeroelastic computer-aided engineering tool for horizontal axis wind turbines developed by National Renewable Energy Laboratory (NREL) [7]. It models dynamic behavior of major wind turbine components, such as rotor blades, tower, and drivetrain. Similar wind turbine simulators are HAWC2 (Horizontal Axis Wind turbine simulation Code 2nd generation) developed by DTU Risø [8] and QBlade developed by Technische

Universität Berlin [9]. These software helps engineers in wind turbine designs by using efficient tools with moderate computation cost.

However, these simulation tools focus on the structural and mechanical aspects of wind turbines, such as blade design, dynamic responses, and power generation. They do not take into account the environmental impacts of wind turbines. One of the key environmental impact is the wind turbine noise, which has a direct effect on human, especially for residents who live nearby. Noise has subjective effects including annoyance, nuisance, dissatisfaction, interference with sleep, and physiological effects such as anxiety or hearing loss. Although many studies have stated that properly sited wind turbines do not have adverse health effect, the noise is still a concerns for communities and an issue for acceptance of wind energy [10]. Thus, wind turbines noise is still one of the disadvantages of wind energy and is hindering its global usage.

A wind turbine design not only needs to be structurally safe under severe weather conditions, but also has to minimize its environmental impacts. Before a wind turbine goes into production, its prototype must pass IEC 61400 (International Electrotechnical Commission, 2002) standard that regards to wind turbine design requirement, safety, and environmental impacts. Two key design standards related to wind turbine noise are IEC 61400-11 TS (technical specification) and IEC 61400-14. IEC 61400-11 TS focuses on the wind turbine acoustic emissions and measurement approaches. According to IEC 61400-11 TS, wind turbine noise emission is determined by a single microphone on the ground $H + D/2$ m away in the downwind direction, where H is the tower height and D is the rotor diameter. The sound power levels in 1/3rd octave band format at wind speed ranged from 6 to 10 m/s are required to be reported. The objective of IEC 61400-14 is to determine the apparent sound power level and tonality of a wind turbine using sound measurement data that is obtained according to IEC 61400-11TS. The rotor size and rotational speed of most wind turbine designs have been limited by these two standards due to the acoustic emissions from the blades. Unfortunately, the rotor size and rotational speed of a wind turbine have significant impacts on the wind energy output, which is related to the cost effectiveness of the wind turbine design. Therefore, it is critical to predict the aeroacoustic noise for a given turbine in the design process and make design changes before prototypes are built.

There are concerns that as the wind turbines get larger, the noise emitted by the turbines would consequently increases. The low-frequency and infrasonic noise components are expected to increase, resulting in less attenuation and potentially more annoyance. Møller did a comprehensive study focusing on large wind turbines noise emissions [11]. The conclusion of his work was that the relative amount of low-frequency (63-250 Hz) noise is higher for large turbines (2.3 – 3.6 MW) than for small turbines (≤2MW), and the difference is statistically significant. This similar trend is expected to continue in the future large turbines (10 MW range).

Although, there are mechanical and aerodynamic noises generated by a wind turbine, the aerodynamic noise is the main source of wind turbine noise [10]. Aerodynamic noise originates from the air flow around the blades that leads to turbulence and vortex shedding. These disturbances of the flow cause small-scale pressure fluctuations that generate this aerodynamic noise. In addition, aerodynamic noise generally increases with tip speed.

Since wind turbine design tools has progressed to include aeroelastic effects with moderate computational cost, wind turbine acoustic models should also incorporate these aeroelastic effects to yield a more accurate noise prediction. The wind turbine acoustic model should be highly efficient in its computation and able to incorporate current wind turbine simulation tools. *This thesis addresses this issue by coupling a well-known wind turbine aeroelastic code and a wind turbine acoustic code that handle wind turbine aerodynamic noise prediction and propagation.* The focus is on modern large wind turbines that have blade span longer than 50 m. The effects of blade aeroelasticity and wind turbine designs are investigated in terms of wind turbine acoustic emissions. The intention is to bring acoustic aspect into wind turbine design engineering that leads to improvement in the wind turbine noise reduction.

1.2 Literature Review

This section reviews the state-of-art in wind turbine aerodynamics and noise prediction models. In particular, the survey on wind turbine acoustic models is focused on models that include aeroelastic effect. Predicting wind turbine aerodynamic noise requires modeling of wind turbine aerodynamics, so aerodynamics of wind turbine is addressed here briefly. Then, different approaches on wind turbine noise prediction and propagation are reviewed.

Aerodynamics of Wind Turbines

Modeling of the aerodynamics of wind turbines can be performed at different degrees of sophistication and complexity. In increased degrees of complexity, these models range from generalized actuator disc, Blade Element Momentum Method (BEM), panel and vortex models, and the Navier-Stokes (NS) models (fundamental parts of computational fluid dynamic software). In the generalized actuator disc model, the rotor is represented by a permeable disc that allows the flow to pass thought the rotor. It is based on conservation of mass, momentum, and energy. The actuator disc model is one of the conventional analytical tools for analyzing rotor performance, and it can be combined with blade-element analysis to form the BEM theory. The BEM theory is a great approach to predict wind turbine rotors performance due to its low computation overhead and acceptable accuracy of the results However, after applying improvements, such as Glauert empirical correction for large induced velocities and Prantl's tip/hub loss corrections for the flow energy loss, the BEM method has shown to yield very accurate results. A more sophisticated approach to capture the complex flow is the vortex model that is used to calculate the induced velocity field by determining the distribution of vorticity in the wake. However, it has disadvantages for yawed flow and operation subject to three-dimensional boundary layer effect [12]. The most computation expensive method is solving the NS equations implemented in computation fluid dynamics (CFD) software. As more advanced numerical models becomes faster and efficient, using CFD analysis becomes acceptable in more complex situation, such as analyzing yaw or interaction between wind turbines in parks [13]. However, this method still requires significant amount of computational resources and not practical for design studies.

Aeroelastic Simulation Codes of Wind Turbines

FAST is one of the most popular wind turbine computer codes [7]. It is a comprehensive aeroelastic code capable of simulating a horizontal-axis wind turbine's rotor aerodynamics, blade and tower structural responses, nacelle yaw, platform responses, and electrical power generations. The fundamentals are based on multibody dynamics of rigid and flexible bodies, aerodynamic modeling, and structural modeling in the different FAST modules. The multibody dynamics module models the structural responses of wind turbine components such as the tower, platform, and rotor. The aerodynamics module utilizes the BEM method with Glauert empirical, Prandtl's hub-loss, Prandtl tip-loss, and Pitt and Peters skewed-wake corrections to handle more complex

flow dynamics. The blade dynamics module models the aeroelasticity of the blades based on the Geometrically Exact Beam theory (GEBT) that supports composite blades with large deformation. Finally, FAST acts as a driver code that orchestrates the results from the modules to simulate an operating wind turbine. FAST has been heavily used in academic research and approved for calculations of wind turbines for design and certification [10].

Another open-source code used in wind turbine simulation is HAWC2 that is intended for calculating wind turbine responses in time domain [8]. The structural analysis of the code is based on a multibody formulation where each body is an assembly of Timoshenko beam elements, e.g. a wind turbine blade and tower. A wind turbine is modeled by an assembly of bodies connected with constraint equations, where a constraint could be a rigid coupling, a pivot joint, etc. The aerodynamic part of the code is also based on BEM, which has corrections to handle complex flow dynamics such as skew-inflow, shear effects on the inductions, and effects from large blade deflections. HWAC2 has been benchmarked against a two-bladed wind turbine by Kim [14]. Good agreement on the blade structural analysis between the simulated case and the full-scale measured loads was presented. There are also many publications regarding HWAC2 available in the public domain.

QBlade is an open-source software for horizontal or vertical axis wind turbine blade designs. The intention of Qblade is to create a one solution software for the design and aerodynamic calculation of wind turbine blades [15]. Thus, the focus of this code is on the wind turbine blade design in terms of its aerodynamics. Besides the blade design, QBlade has an aerodynamic analysis, which is based on the BEM with the corrections mentioned in FAST and HWAC2. The integration of XFOIL enables the user to design customize airfoils, compute their polars, and directly integrate them into a wind turbine simulation. The latest version of QBlade implemented FAST v7.0, an old version of FAST, to enable aeroelastic simulation. The graphic user interface made this software easy to use, unlike the usual command line interface software tools. As a result, the number of QBlade users is gradually increasing and it may potentially become a mainstream wind turbine blade design tool. However, QBlade is limited to the aerodynamics of the blade, optimizations of the blade twist, curvature, and chord distribution. The blade structural design, skin materials, deflection, and aeroelasticity are not covered in QBlade. The integration of FAST v7.0 also cannot

capture full effects of aeroelasticity for large wind turbine composite blades due to its over-simplified beam modeling approach. Therefore, there is room for improvements for QBlade to become a comprehensive wind turbine simulation code, such as FAST and HWAC2.

Wind Turbine Aerodynamics and Aeroacoustic Noise Models

The number of computational tools for the noise predictions of a wind turbine is much more limited than aeroelasticity codes. Moriarty from NREL developed an semi-empirical aeroacoustic noise prediction code, *NAFNoise* (NREL Airfoil Noise), to predict six different components of airfoil-self noise [16]. They are turbulent boundary layer tailing edge (TBL-TE), separated flow (SF), laminar boundary layer vortex shedding (LBL-VS), trailing edge bluntness vortex shedding (TEB-VS), tip noise, and turbulent inflow(TI). Figure 3 illustrates the aerodynamic noise mentioned above. The first five noise models are based on the work of Brooks, Pope, and Marcolini, who formulated semi-empirical relations for these noise sources[17]. Turbulent inflow noise is based on the works of Lowson [18]. The first assumption is that six different aerodynamic noise sources are uncorrelated, i.e. each of the noise source generates its own noise signature. This is because the mechanism of the noise sources are fundamentally different from each other or occur in different locations along a blade, so no interference between each other occurs. Table 2 list the noise sources described here.

A turbine noise prediction can be computed using *NAFNoise* [19]. As the blades are divided into multiple sections, *NAFNoise* is able to compute the airfoil-self noise from the sections for all the noise components. Finally, the total noise of an operating wind turbine is calculated by superimposing all the aerodynamic noise incoherently.

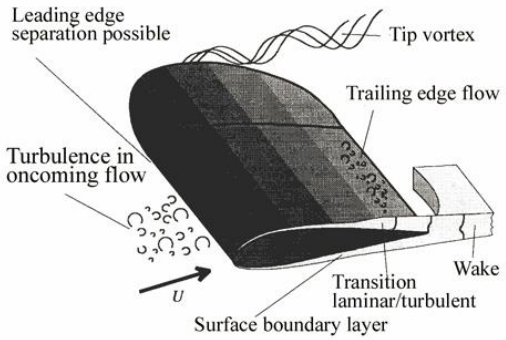

Figure 3: Illustrations of noise mechanisms generated by flow around an airfoil. [20].

Table 2: Wind turbine aerodynamic noise mechanisms [20].

Type or indication	Mechanism	Main Characteristics and importance
Low-frequency noise		
Inflow turbulence noise	Interaction of blades with atmospheric turbulence	Contributing to broadband noise not yet fully quantified
Airfoil self-noise		
Trailing-edge noise	Interaction of boundary layer turbulence with blade trailing edge	Broadband, main source of high frequency noise (770 Hz$<f<$2 kHz)
Tip noise	Interaction of tip turbulence with blade tip surface	Broadband; not fully understood
Stall, separation noise	Interaction of turbulence with blade surface	Broadband
Laminar boundary layer noise	Nonlinear boundary layer instabilities interacting with the blade surface	Tonal, can be avoided
Blunt trailing edge noise	Vortex shedding at blunt trailing edge	Tonal, can be avoided
Noise from flow over holes, slits and intrusions	Unstable shear flows over holes and slits, vortex shedding from intrusion	Tonal, can be avoided.

NAFNoise was validated against acoustic test data of two-dimensional airfoils and a full-size wind turbine. For the airfoil validation, the results have a good agreement with airfoil NACA 0012 at a moderate angle of attack (AoA < 6°) [16]. The Atlantic Orient Corporation (AOC) 15/50 was used in the full-scale turbine validation. It is three-bladed fixed rotational speed (64.6 rpm, independent of mean wind speed) downwind wind turbine that has a rated power of 50 kilowatts (kW), a rotor diameter of 15 m, and hub height of 25 m. The measured OASPL data was taken 32.5 m (close to the wind turbine) away in the downwind direction (according to IEC 61400-11 TS). The noise simulation case used turbulent wind condition to simulate realistic conditions. The predicted overall sound pressure levels (OASPL) were fairly close to the measured data as shown in Figure 4 [16]. Comparing to the measured data for a mean wind speed of 8 m/s of a normal turbulence wind condition, the predicted total noise spectrum shows good agreement in the range between 1k and 5 kHz as shown in Figure 5. Some slight disagreement between the noise predictions and measured test may be due to AOC 15/50 wind turbine design. First, it has no nacelle so mechanical noise had significant contribution to the measured OASPL. Second, the tower shadow of the downwind turbine design introduced turbulent eddies that also contributed significantly to the measured noise. The turbulent eddies may not occur for the upwind turbines, but further research is required.

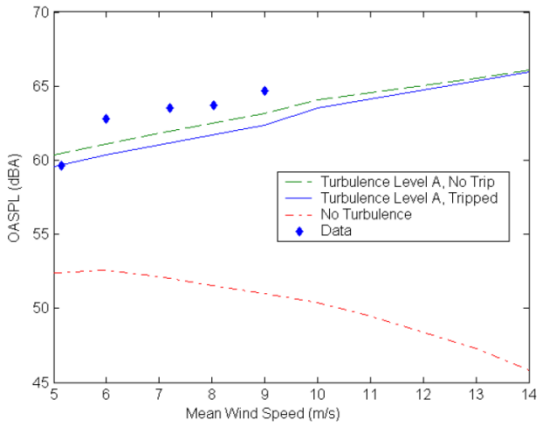

Figure 4: The OASPL vs. wind speeds for the AOC turbine (the noise data was taken according to IEC 61400-11 [21].

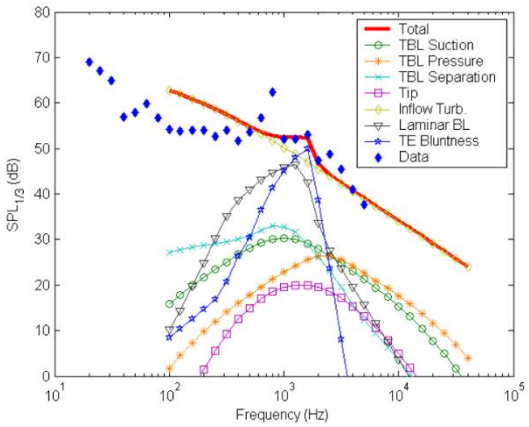

Figure 5: The noise spectrum from FAST v7.0 noise predictions vs. measured data in 8 m/s turbulent wind for the AOC turbine [21].

The *NAFNoise* was implemented into NREL FAST v7.0, an older version of FAST that has lower fidelity of simulating wind turbine operations. It is one of the subroutines of FAST v7.0 that takes the aerodynamic results to compute the wind turbine aerodynamic noise. The noise propagation is not included. Unfortunately, this noise code is not included in the most updated FAST v8.16, which offers high fidelity blade structural analysis. NREL FAST v7.0 employed an over-simplified beam model that is incapable of accurately predicting dynamic responses of a modern wind turbine blade, e.g. large blade span and anisotropic composite materials. ***In addition, this noise code only supported blade designs that use the same airfoil family due to accuracy on predicting boundary layer thickness*** (the validation done on AOC 15/50 has the blade design using the same airfoil family). A single airfoil family blade design is extremely uncommon for large-scale wind turbines. Thus, this noise code is impractical for predicting noise of large wind turbines.

Zhu *et.al.* [22] used a similar approach on wind turbine noise predictions that uses BEM results, such as local relative velocities and boundary layer parameters, as inputs that feed into the semi-empirical acoustic models by Brooks *et.al.* [17]. The noise predictions of a Bonus 300 kW wind turbine (rotor diameter 30.5m) were validated against its measured acoustic data. A single microphone was placed on the ground 40 m downstream of the wind turbine in the experiment. The predictions were based on power-law wind profiles with 8 m/s reference wind speed, and the measured data had a wind speed 8 m/s at 10 m height. The blade was assumed to be rigid and were made of NACA 632xx airfoils. Zhu concluded that the noise model yielded good agreement with the measurements, but the noise prediction models could be improved with accurate boundary layer thickness. In summary, the two individual studies done by Moriarty and Zhu used BEM for aerodynamics and the semi-empirical noise models [17] for wind turbine aerodynamic noise predictions. However, both of these studies only included relatively small turbine that had single airfoil family blade design. Thus, the accuracy of the semi-empirical acoustic models by Brooks *et.al.* [17] on large wind turbine noise predictions requires further research.

A different approach on aerodynamics and noise of wind turbines was used by Son [23]. He used the Wind Turbine Flow, Aeroacoustics and Structure analysis code (WINFAS) to calculate the flow field around a wind turbine blade [23]. WINFAS is an unsteady vortex lattice method based on potential flow. Son stated that vortex lattice method has advantages in capturing rotational wake of turbines. The results from WINFAS were used for predicting tonal noise, turbulence ingestion noise and airfoil self-noise. These noise predictions were based on the semi-empirical noise models by Brooks et.al. [17]. The noise level results were validated against measurement data (taken according to the IEC 61400-11 standards) of two wind turbines: AOC 15/50 and Markham VS-45 (rated power: 600 kW with 45.9 m rotor diameter) with power curve over uniform wind speed which varies from 4 m/s to 12 m/s. Comparisons between the predictions and experimental data showed good agreements. Son also presented a noise propagation model using ray tracing method for a commercial wind turbine, NEG-Micon 1.5 MW (rotor diameter 72m). The noise propagation was performed for NEG-Micon 1.5 MW at rated rotational speed 17.3 RPM with reference wind speed 10 m/s. In the noise propagation cases, the terrain was consider flat, no refracted wave, and neither temperature nor wind speed gradients (straight rats). In addition, the blades were assumed to be rigid in the study.

Kim extended Son's approach by taking consideration of blade flexibility [24]. The aerodynamic analysis was still carried out by WINFAS, but blades are flexibles unlike in Son's study. The nonlinear composite beam theory [25], as known as GEBT, is used for blade dynamic responses and was coupled with WINFAS. The results of WINFAS and GEBT are the inputs for the semi-empirical models based on the work of Brooks et.al. [17], but only the Turbulent Ingestion (TI) noise [18] and TBL-TE noise are modeled. Kim's approach was validated against NREL Phase VI (two-bladed wind turbine with rotor diameter 10.06 m) experiment results, but only on the aerodynamic part. The noise prediction was validated against measurement data of NEG-Micon NM-72 wind turbine (three-bladed upwind wind turbine with rated power 1.5 MW and rotor diameter 72 m) and showed good results against experiment data on sound power level. The noise predictions were performed with uniform flow at reference wind speeds ranging from 5 to 10 m/s. The acoustic measurements were made according to IEC 61400-11 standard, where the microphone was located at ground level at a distance of 100 m away in downwind direction. Some differences were observed in the 1/3 octave band spectrum at reference wind speed 6 m/s as shown in Figure 6. Kim stated that the differences may come from the mechanical noise of the turbine components, such as the gearbox or control actuators.

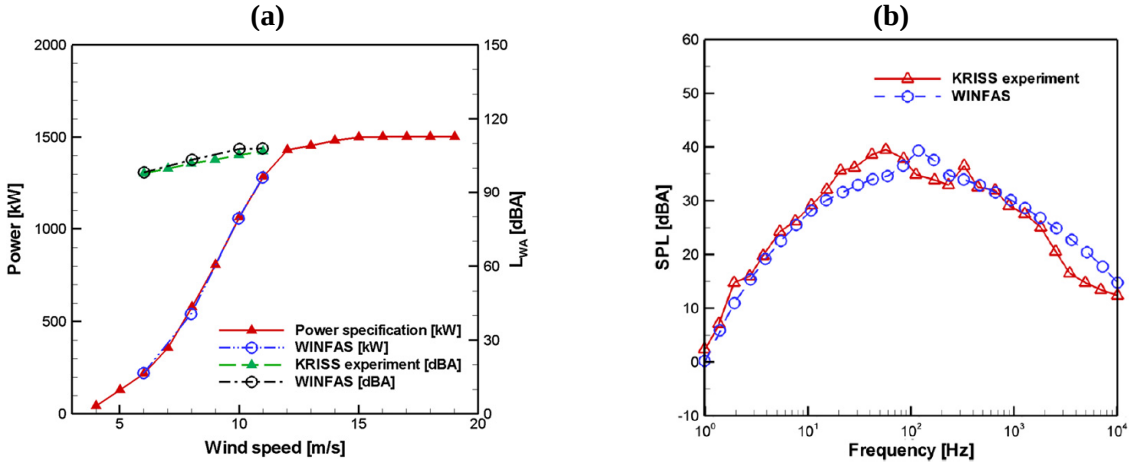

Figure 6: WINFAS noise prediction and experimental data: **(a)** The NM-72 turbine power and sound power level *vs.* wind speeds. **(b)** The SPL spectrum in 1/3rd octave band at wind speed 6 m/s. Note that measurement was performed by Korea Research Institute of Standards and Science (KRISS) [24].

Kim also simulated a 3MW three-bladed turbine with the rotational speed 15.7 RPM under a uniform flow condition at different wind speeds to demonstrate the effects of blade flexibility. The blade span is 45.8 m long and consists of DU series and NACA64-618 airfoils. Aerodynamic

power and noise of the flexible blades and rigid blades were examined. The flexible blades yielded lower aerodynamic power than rigid blades as shown in Figure 7a. There was 5% difference at wind speed of 10.5 m/s. This was due to the blade deformation that changed the effective AoA. In addition, the blade pitching down due to the blade flexibility demonstrated a significant effect on the decrease of the AoA, which highly affects aerodynamics of the rotor. For the aerodynamic noise considering the blade deformation, Kim presented multiple cases at wind speeds ranging from 4 m/s to 18.5 m/s under a uniform wind condition as shown in Figure 7b. The SPL predictions were made at a distance close to the turbine (< 200 m), but the specific distance was not mentioned in the article. The SPL difference considering blade with and without deflection was about 1.5~2 dB at wind speeds at 10.5 m/s and 11.5 m/s. In scales of the predicated OASPL, this difference between rigid and flexible blades was small in terms of the aerodynamics noise level. The SPL footprint on a flat terrain for a rigid and flexible blade assumption is shown in Figure 8. The figure indicates that the sound power level predicted in the rigid blade condition was higher than the flexible blade condition. It also follows the trend of that noise levels of flexible blades are slightly lower than rigid blades over various wind speed as presented in Figure 7b. The conclusion of Kim's work was that aeroelasticity of the blades slightly decreased the wind turbine noise. The main reason was that the blade deformation changed the blade pitching motion, resulting in a decrease in AoA of the blades. Thus, decrease in AoA results in aerodynamic power reduction and noise attenuation [20]. Other reasons for insignificant SPL change was due to the pitch control unit that modern large wind turbines have. For wind speed over 12 m/s, the rated wind speed, the pitch control actuator changed the blade pitch angle to low AoA range, i.e. there are smaller variations of noise level than that in the condition of low AoA (around 0°) than high AoA (around 5°). Kim's research is likely the first, and probably the only, that addressed the effect of blade aeroelasticity in the noise prediction. However, it has some limitations. The noise prediction was limited to 200 m away from the wind turbine. In addition, Kim stated that "*With respect to noise assessment, this method take too long to predict the noise produced by a modern large wind turbine*." In other words, there should be a more efficient way to predict large wind turbine noise that takes into consideration the present of aeroelasticity, different wind conditions (other than steady uniform flow), turbine design (other than pitch-controlled variable speed wind turbines), and propagation over long distances.

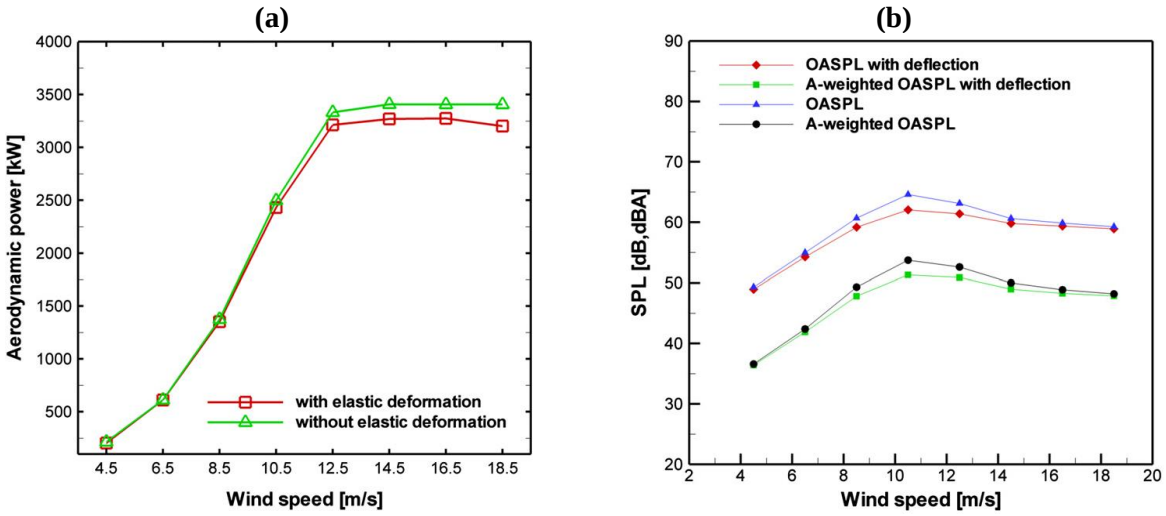

Figure 7: (a) The NM-72 turbine aerodynamic power with blade deformation. **(b)** The NM-72 turbine SPL *vs.* uniform wind speeds with blade deflection [24].

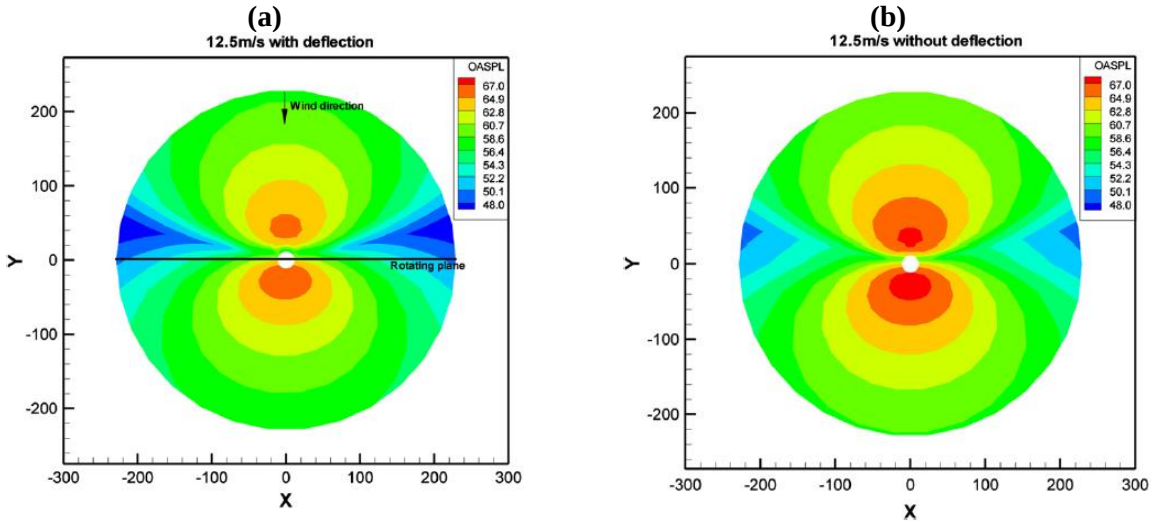

Figure 8: The NM-72 turbine OASPL footprints at wind speed of 12.5 m/s: **(a)** flexible and **(b)** rigid blade [24].

Arakawa performed the first direct noise simulation of a full wind turbine, WINDMELIII (two-bladed turbine with the rotor diameter of 15 m), using a Large Eddy Simulation (LES) based CFD solver for the aerodynamic noise prediction [26]. The noise propagation was based on the finite difference method using a supercomputer, The Earth Simulator. The flow condition was uniform wind at 8 m/s without wind speed and temperature variations. Arakawa's approach required very fine computational meshes and hence large amounts of computational resources. The simulation time was 300 CPU hours with 112 processors in parallel. The result showed a good agreement with the noise measurements in the near-filed only (< 60 m away from the wind turbine). However, large differences were observed in the far field. This was due to the insufficient span-wise grid

resolution. Tadamasa followed a similar approach and argued that semi-empirical methods from Brooks et.al. [17] has limitations on capturing 3D effects [27]. He utilized Reynolds-averaged Navier-Stokes (RANS) based CFD solver (ANSYS CFX 11.0) to calculate aerodynamic parameters that were used inputs for the Ffowcs Williams-Hawkings (FW-H) equations to predict aerodynamic noise. The noise prediction of NREL Phase VI wind turbine was validated against the measured data. The wind turbine operated at 72 RPM with a uniform flow at different wind speeds in all cases. At wind speed 7 m/s, the blade pressure distributions from the CFD simulation showed good agreement with the experimental data [28-30]. However, slight discrepancies were observed for wind speed over 7 m/s. The discrepancies occurred on the suction surface of the blade due to the error caused by the flow separation prediction in the CFD simulations. It is important to mention that the acoustic results were not included in the validations. In addition, due to decoupling of aerodynamics and structural dynamic of CFD software, the blade was assumed to be rigid in his study.

Wasala used a similar approach that uses FE-W equations for noise prediction but based on results of LES CFD solver (ANSYS Fluent) [31]. Instead of modeling an entire blade, Wasala only modeled a certain section of a blade of the CART-2 (Control Advanced Research Turbine, a two-bladed wind turbine with rated power 600 kW and the rotor diameter 42m). He performed CFD simulations on 75% to 95% of blade span sections that consists of a modified LS(1)-04XX airfoil. The reason for modeling only part of the blade is based on Oerlemans's acoustic camera measurement suggesting that the majority of noise sources are located at 75-95% span section of a wind turbine blade, where local flow velocities are relative high [32]. In addition, Wasala assumed there was no radial flow on the blade to reduce computational cost. The CFD simulation was conducted for the case where the blade pitch was 3° and rotating at 41.7 RPM. The inflow had uniform wind at 10.8 m/s and the upwind turbulence intensity was 10.3%. Only a single rotating blade section was numerically simulated, but the noise calculation took account for the second blade by placing an extra identical source at its relative location. The validation against acoustic measurements [16] and the semi-empirical code [16] also showed good agreements as shown in Figure 9a. The acoustic measurements were made according to IEC 61400-11 standard. Figure 9b shows the acoustic footprint at a 58 m radius at ground level around the wind turbine with selected frequency bands. The noise levels from the CFD simulation agreed with the semi-

empirical code. However, the noise levels from CFD simulation in the upward direction were slightly higher than for downwind due to the Doppler effect caused by the onset wind. Rigid blade assumption was applied along with other assumptions. These assumptions may not hold for a modern large wind turbine (blade span > 50m), as its blade span is significantly longer than CART-2 blade (blade span ~20m). Although the computational cost is reduced by modeling only 75% to 95% of the blade, the simulation time was not mentioned.

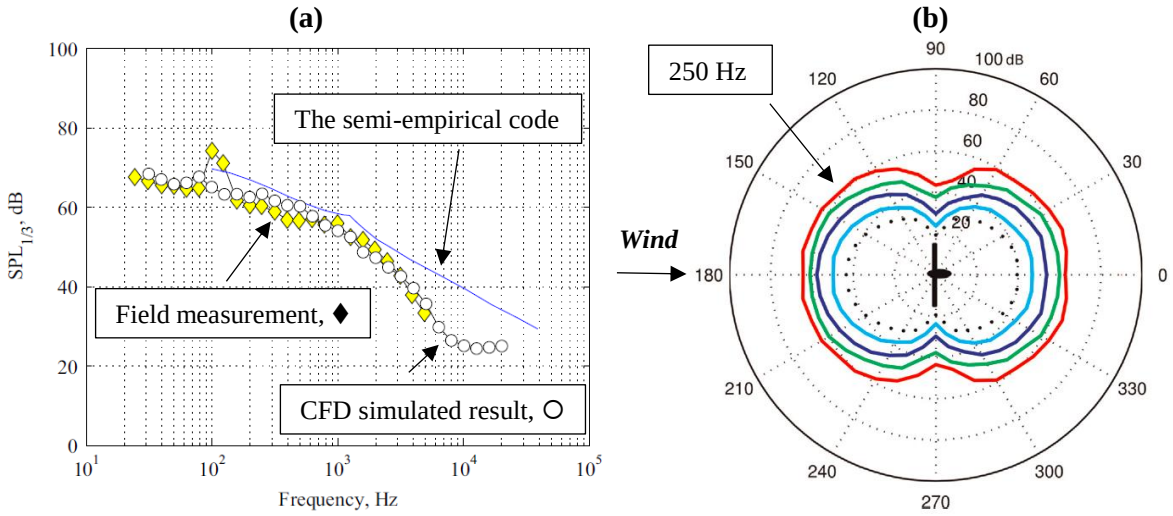

Figure 9: (a) Comparison of predicted and measured noise spectrum for CART-2 wind turbine and **(b)** the directivity at 250 Hz, 500 Hz, 1 kHz, 2kHz, and 4kHZ [31].

Table 3 shows a list of all the wind turbines that have been used for validations or modeling. An interesting trend is that most studies still employed the semi-empirical noise model from Brooks et.al. [17]. However, the noise propagation were not included in the wind turbine noise prediction.

Table 3: List of wind turbines cases studied in past publications.

Paper	***Year***	***Wind Turbine***	***Rotor dia. , m***	***Aerodynamic Noise Model***	***Noise Propagation***
Moriarty	2003	AOC 15/50	15.00	*Semi-empirical	Not Included
Zhu	2005	Bonus 300/33	30.50	*Semi-empirical	Not Included
Son	2009	Markham VS-45	45.90	*Semi-empirical	Ray Theory
Kim	2011	NREL Phase VI	10.06	*Semi-empirical	Not Included
		NEG-Micon NM-72	72.00		
Tadamasa	2011	NREL Phase VI	10.06	CFD, FW-H	Not Included
Wasala	2015	CART-2	42.00	CFD, FW-H	Not Included

*The semi-empirical aeroacoustic models are based on work of Brooks, Pope, and Marcolini

Table 4 shows the different approaches discussed for modeling wind turbine aerodynamics. An interesting trend is that these approaches become more sophisticated as time progresses, but flexibility of blades were excluded in many studies except in Kim's work. In addition, most of these studies validated their results with relatively small rotors. Rigid blade assumption may be sufficient and practical for small rotors (the diameter < 100 m) due to the relatively smaller bending loads than large rotors experience. For a modern large wind turbine, the rigid blade assumption cannot be held since their blades undergo large deformation. This aeroelastic effect may have a significant influence on the wind turbine noise. In Kim's work, using GEBT to model wind turbine blade deformation and aerodynamic noise is a practical approach since large wind turbine blades are made out of composites and have large deformations. However, his approach was not efficient in terms of computation due to the more sophisticated aerodynamic modeling. Therefore, from the literature review above, there is an obvious need for modeling wind turbine noise and propagation in a more efficient way.

Table 4: Different approaches to model wind turbine aerodynamics.

Approach of Aerodynamics	Literature	
BEM	Moriarty, 2003 FAST v7 implantation of a semi-empirical noise model based on Brooks, Pope, and Marcolini (1989).	Zhu, 2005 Validation of the semi-empirical noise model against 800 kW wind turbine.
Vortex lattice method	Son, 2009 Extended the semi-empirical noise model for long range noise propagation.	Kim, 2011 Introduced nonlinear beam theory for flexible blade. Used the same semi-empirical noise model.
CFD	Tadamasa, 2011 Used FW-H equations for the noise based on CFD, Reynolds-Averaged-Navier-Stokes Simulation result.	Wasala, 2015 Used FW-H equations for the noise based on CFD, Large Eddy Simulation results.

: Indicates the blade is rigid
: Indicate the blade is flexible

Wind Turbine Noise Propagation

For wind turbine projects, the installation permits are subject to compliance with local noise restrictions, i.e., maximum allowable sound pressure levels at the wind turbine boundaries or residential locations at typical distances from 600 to 2000 m [33]. Therefore, an upfront simulation of wind turbine noise propagation is a key factor in wind turbine siting and receiving installation permissions from local government. An improperly sited wind turbine will cause annoyance and complaint as the noise propagates to the near-by residents. For example, Gabriel reported acoustic studies and surveys of local residents around a small wind farm in northern Germany [34]. The wind farm consists of nine 2-MW wind turbines with a hub height of 108 m. The local residents are located approximately 1500 m away from the wind farm. The most common noise complaint was related to the amplitude-modulated aerodynamic noise, as known as “swishing” sound. These

negative feedback from the communities may prevent wind turbine being installed in some areas, or potentially decrease acceptance of wind energy in general. ISO 9613-2 is one of standards that regulates propagation of industrial noise and has been widely applied for wind turbine noise propagations. Other methods that have been used for the wind turbine noise propagations are briefly presented here.

ISO 9613-2 utilizes empirical sound propagation models to predict wind turbine noise in the far-field. It is used to simulate noise disturbances to residents near a wind turbine. For example, a recommendation to the Canadian Wind Energy Association mentioned that prediction of sound level should be made using an accepted methodology that takes into account the layout of the wind farm and the topography of the surrounding area, e.g. ISO 9613-2, *Acoustics-Attenuation of sound during propagation outdoors* [1]. The general characteristics of ISO 9613-2 models are that they are valid for flat terrain and moderate downwind speed (wind speed at around 12 m/s). In addition, this method was developed on basis of empirical data for medium noise source heights (< 100 m). Therefore, ISO 9613-2 is not perfectly suitable to predict far-filed noise levels for the large modern wind turbines (large noise source height) in other wind conditions or complex terrain [35].

More advanced models for noise propagations are the parabolic equation (PE) and ray acoustic model. The PE method is a numerical method for computing the sound field of a monopole source. The approach is to solve a parabolic equation, which follows from the wave equation with varying wavenumber or the speed of sound. It is able to capture effects of sound speed variation, ground impedance variation, atmospheric turbulence, and irregular terrain. In addition, the PE method is not limited to a layered atmosphere and a homogenous ground surface. The disadvantages of the PE method are the high computation time (numerically intensive) and meshing limitation (using finite differences scheme or finite element analysis). To reduce computing time, the computations are usually performed in 2-dimensions, in the vertical plane through the source and the receiver. This approach is based on axisymmetric approximation, which neglects the variation of the sound field with the azimuthal angle (the angle around the vertical axis through the source). Lee utilized the PE model that used CFD results (wake flow velocity profiles that vary as a function of the distance and height) to accurately predict wind turbine noise propagation for complex flows [33]. The PE model has been validated against analytic solutions, benchmark problems, and

experimental data. The experimental results were obtained with a B&K omni-directional speaker that generated pure tone sound at 20 or 80 m height. The data were collected at National Wind Technology Center of the NREL. However, Lee's PE model under-predicted the noise levels compared to the experimental data at the far-field in the upwind direction due to lack of turbulence scattering effect. The wind turbine noise propagation was done by assuming a point monopole source at the rotor center (rotor diameter was not mentioned in the context) for propagation range of 3 km at the downwind direction. The wind turbine wake flows were simulated in ANSYS CFX using an actuator disk (AD). The PE model showed that turbine wake flow significantly modified the sound propagation characteristics, but the finding was slightly different from the conclusion of Heimann *et al.* that claimed the wake flows increase the noise levels at large distance ($\leq$1 km) [36]. Lee's results demonstrated that the effect of wake flows led to a large change in the noise levels beyond 1.5 km in the propagation. Lee's approach excluded the effects of the directivity and was limited to 2D propagation, flat ground, and non-turbulent atmosphere. However, these effects have significant influences on the accuracy of wind turbine noise propagation. Therefore, there are improvements to be made for PE models in wind turbine noise propagations.

The ray acoustic models are highly popular for predicating wind turbine noise propagation. Prospathopoulos and Voutsinas conducted a comprehensive study on their ray tracing propagation model against other sound propagation models (IEA model, NORDFORSK model, CONCAWE model, and ENM model) with measurement data on different terrains [37]. The ray tracing propagation model could not only accurately simulate the ground and atmospheric effect, but it also takes into account the spatial variation of the terrain, wind velocity and temperature profiles. There are four validation cases: 1.) a loudspeaker 29 m above ground level on a smooth terrain at the Carland Cross site, England, 2.) a MONOPTEROS 50 wind turbine of 60 m hub height and 56 rotor diameter on a flat terrain at the Tammhausen site, Germany, 3.) a Tacke 500 kW wind turbine of 35 m hub height and 36 m rotor diameter on a complex terrain (the hills and slopes varying from 3° to 20°) at the Toplou site, Greece, 4.) an NWP 400 wind turbine of 40 m hub height and 35 m rotor diameter with a rocky terrain at the Lyse site, Sweden. The acoustic measurements were taken from 1.5 m above the ground level at various directions and distances from the noise sources. In the theoretical noise predictions, the wind turbine noise was assumed to be a point source at the rotor center. Prospathopoulos's model successfully yielded good agreements with the

measurements from Case 1 and 2. The results also demonstrated that simple models, IEA and NORDFORSK, gave satisfied predictions for flat terrains. In the cases of complex terrains, such as Case 3 and 4, the simple models could not accurately predict the wind turbine noise propagation. Prospathopoulos's model had satisfied results compared to the measurements, but the low-frequency noise amplification in the measurement was not observed in the prediction. The reasons may due to the local topographic or weather effects, or the inability of the ray tracing model to perform well at low frequencies. His study has demonstrated that ray tracing models are capable of predicting wind turbine noise propagation with satisfied agreements with the actual acoustic measurements.

Other ray tracing based commercial codes for predicting wind turbine noise at long distance (a few kilometers away) are also available. They are SoundPLAN, CadnaA, Predictor-LIMA, WindPRO, NORD2000 and so forth for predicting wind turbine noise propagation with models of increasing degree of sophistication. The most advanced sound propagation code is NORD2000. It implemented a simplified ray tracing method that supports moderate atmospheric refraction by assuming linear sound speed profile. The atmospheric absorption for refracting and non-refracting media are being accounted for as well. Other factors, such as atmospheric conditions including thermal stratification, humidity, and uneven terrain are included in their propagation models. However, for all the noise propagation models, the wind turbine noise is assumed to be a monopole at the hub, which does not consider the actual radiation characteristics of the wind turbine noise. These methods rely on the wind turbine's SPLs from manufacturers' databases or user inputs [38].

Plovsing conducted a series of studies on the accuracy of the NORD2000 propagation model when used to predict noise from high elevation, such as wind turbine noise [35]. The experimental results have been used to compare with NORD2000 simulation results. The NORD2000 results showed good agreement against loudspeakers at 50 m and 70 m above flat and non-flat terrain. However, the agreement between these results are not good for the upwind propagation. The noise measurement of a 70m high wind turbine (the wind turbine specification is not mentioned, but top of the nacelle is 70 m height) in non-flat terrain is also compared to the NORD2000 prediction. The results shows bad agreement in both upwind and downwind propagation. The reasons may be the noise measurement procedure (IEC 61400 measurement procedure) and oversimplified point

source at the hub height. Therefore, there are improvements to be made to accurately predict wind turbine noise propagation.

It is important to state that the noise propagation models mentioned above are individual codes that is performed after SPLs of a wind turbine is determined via theoretical prediction or actual noise measurement. In addition, it is difficult to differentiate wind turbine noise measurement data from mechanical and aerodynamic noise, which can be predicated through many approaches. The wind turbine noise prediction can be significantly efficient if a noise propagation model is coupled with a wind turbine aeroacoustic model. In this way, engineers are able to properly design rotor blades that minimize their aeroacoustic noise in the preliminary design phase. Furthermore, they can gain valuable insights on the estimated wind turbine aerodynamic noise and how it propagates to the far-field. These analysis tools may help wind turbine companies in terms of designs, wind turbine siting, and also passing the standards and regulations from local governments. If a wind turbine aeroelastic code is coupled with aeroacoustic code and sound propagation code, an accurate noise prediction of a modern large wind turbine may be feasible.

1.3 Thesis Objectives

The primary goal of this thesis is to investigate the influence of blade aeroelasticity on the wind turbine noise primarily over long distances (> 0.5 km). The influence of wind turbine parameters, such as the rotor size, yaw, tilt, and pre-cone angles as shown in Figure 10, are also investigated in this thesis. To achieve these objectives, the proposed approach is to couple the aeroelastic code (FAST v8) or a stand-alone version of FAST submodule (AeroDyn v15.03) with a wind turbine aeroacoustic noise code, WTNoise [38], as shown in Figure 11.

First, the stand-alone *AeroDyn* [39] (*AeroDyn* v15.03) is incorporated to compute the turbine aerodynamics for rigid blade cases. Second, FAST is incorporated to account for blade elasticity (flexible blade) in the calculation of aerodynamic parameters. Then, WTNoise takes the aerodynamic parameters (either from FAST or *AeroDyn*), such as AoA, inflow wind speed, and inflow angles, as inputs to compute airfoil-self noise of each section of the blades using *NAFNoise*. Finally, the wind turbine noise propagation is carried out by an Hamiltonian ray tracing technique based on the work of McBride [40]. It is able to account for the atmospheric conditions in

propagation, e.g. the wind and temperature gradients. The inputs are the airfoil noise that accounts for the actual radiation characteristics of the wind turbine, i.e. wind turbine noise source has a strength and radiation pattern that is a function of the azimuth position of the rotor. Therefore, a wind turbine noise prediction and propagation code that account for the blade aeroelasticity, turbine parameters, and radiation characteristics are achieved by coupling FAST with WTNoise.

Multiple noise predictions with different turbine parameters and blade flexibility assumptions are conducted using the above approach. Tasks that are performed in this thesis are:

a. *Noise predictions for non-uniform wind field near and far away from the turbine to investigate each turbine parameter independently (yaw, tilt, or pre-cone angles)*
b. *Noise predictions for elastic blades and compared to rigid ones.*
c. *Noise predictions for two turbines of different sizes.*

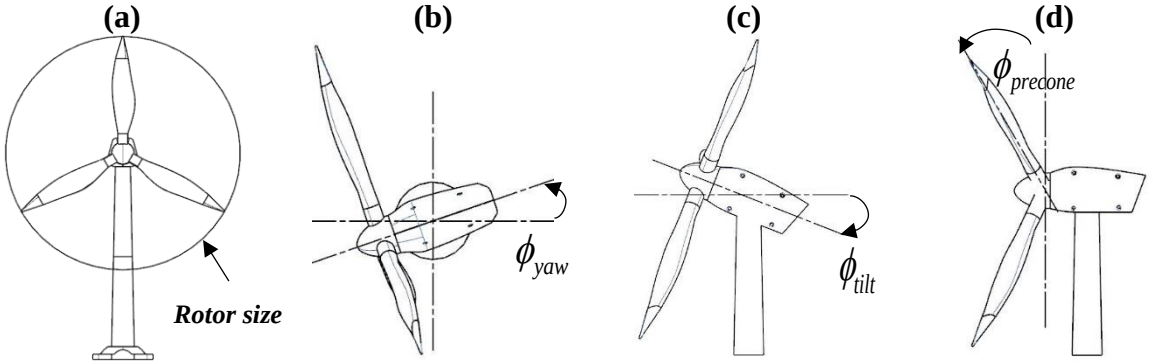

Figure 10: Illustrations of the wind turbine parameters investigated in this study, **(a)** rotor size, **(b)** yaw angle, **(c)** tilt angle, and **(d)** blade pre-cone angle.

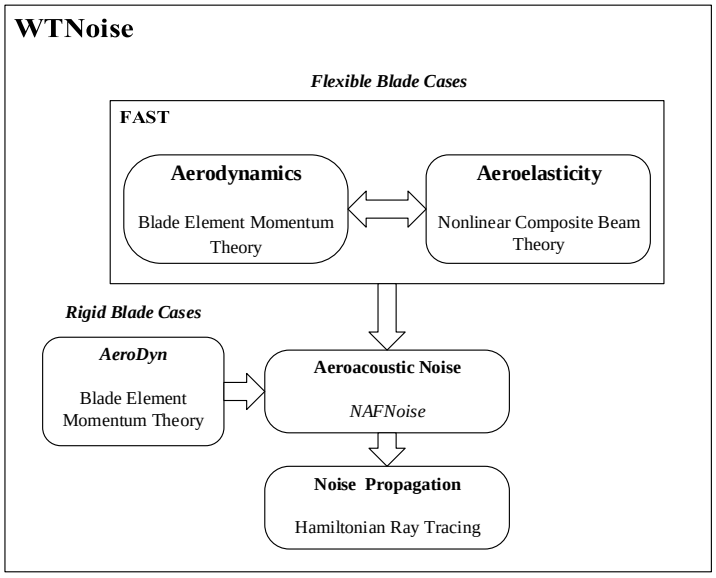

Figure 11: Proposing approach on large wind turbine prediction.

This study focuses on modern large wind turbines that have blade span ranging from 60 to 100 m. More specifically, the turbine ***average*** noise and propagation in the steady state condition at its rated operating condition are modeled. The potential influences on the rotor aerodynamics due to the tower are excluded such as tower potential-flow. The wind turbine foundation, tower, and nacelle are assumed rigid in this research. Several factors of wind turbine noise prediction and propagation will not be accounted for, such as the vertical wind component, and effects of uneven terrain. In addition, the influence of turbulence wind conditions on wind turbine noise are beyond the objectives of this thesis, but may be considered in future work. In this study, steady wind condition with vertical and shear profile is used.

The proposed approach overcomes many drawbacks that are mentioned in the literature, such as rigid blade assumption, high computational cost on the vortex lattice or CFD methods, uniform wind profiles, and a monopole source assumption for the turbine noise modeling and propagation. As the literature review mentioned, most of the wind turbine noise predictions are under rigid blade assumption. This assumption is applied on calculations of a wind turbine's aerodynamic parameters, which has significant influences on the wind turbine noise prediction. Unfortunately, this assumption is not valid for modern large wind turbines (rotor diameter > 80 m) due to large deflections of the blades. The blade deflections may significantly change the aerodynamic parameters that lead to large changes in the wind turbine noise prediction and the propagation

characteristics. Kim's [24] approach has the fluid-structure interaction which enables the blade aeroelasticity, but the computational cost was too large to be an efficient approach on wind turbine noise prediction. The high computational cost on wind turbine aerodynamics is overcome by using BEM that has efficient computational time and yields satisfied results [13, 41, 42]. In addition, FAST's BEM algorithm supports a non-uniform wind profile that may contain vertical or shear wind components. A 30 second FAST simulation on NREL 5MW only takes less than 5 minutes to yield all the necessary aerodynamic parameters for the wind turbine noise prediction. Therefore, the proposed approach significantly improves the computational time required and yields satisfied aerodynamic calculations for a wind turbine noise prediction.

In terms of noise propagation, the proposed Hamiltonian ray tracing averts many of the setbacks presented by other common approaches, such as parabolic equation [40]. The Hamiltonian ray tracing technique also showed good agreements against other common approaches, such as PE, and other ray acoustic models [40]. In addition, the wind turbine noise model no longer assumes a monopole source at the rotor center as a usual practice in the wind turbine industry.

The proposed approach significantly reduced computational time and offers great flexibilities by supporting different wind conditions, blade flexibility assumptions, and wind turbine parameters. In addition, wind turbine noise and its propagation can be efficiently and accurately predicted. These advantages allow engineers to have the first insight of the wind turbine noise on their designs. A better understanding on the influences of aeroelasticity and wind turbine parameters on wind turbine noise potentially help in large wind turbine developments by minimizing wind turbine aeroacoustic noise. Potentially, this proposed approach and study will contribute to large wind turbine developments and the acceptance of wind energy.

1.4 Thesis Organization

The structure of this paper consists of five chapters. Chapter 1 is an introduction that presents the motivation, literature review, and objective of this study. Chapter 2 explains the fundamentals of FAST, its submodules, and an example case of NREL 5MW turbine. Chapter 3 presents the WTNoise, in which the wind turbine noise and the propagation models are implemented. Chapter 4 presents the designs of wind turbine blades, weather, and terrain properties that are used in the

simulations. In addition, the results of this thesis are presents. Chapter 0 presents the main conclusion of the present and recommendations for future work.

The appendixes provide more theoretical details on the codes that are used. Appendix A presents the conventional BEM theory and the modified BEM in the *AeroDyn*. Appendix B presents the GEBT formulation and the *BeamDyn* fundamentals. Appendix C presents the aerodynamic noise models in the *NAFNoise*. Appendix D shows tables of the NREL 5MW blade sectional airfoil designs and structural properties. Appendix E presents the Sandia SNL100-02 blade sectional airfoil designs and structural properties as tables.

2. Aeroelastic Code FAST

This chapter presents the fundamentals of the wind turbine simulation code, FAST. The latest version of FAST (FAST v8.16.00a, July 26, 2016) is used in this study [7]. Each module used in FAST and its theories are briefly presented.

2.1 Coordinate systems of FAST

This section introduces the various coordinate systems in FAST. It has a inertial frame coordinate system (global coordinate system) and other coordinate systems for the wind turbine's tower, nacelle, shaft, hub, and blades as shown in Figure 12a [43]. The (x, y, z) global and tower coordinate systems are the same. The origin is at the center of the tower bottom with the x-axis pointing in the downwind direction, the y-axis pointing to the port, and the z-axis pointing vertically upward. Both of these two coordinate systems are fixed in this study, i.e. no translational and rotational displacement. The nacelle coordinate system translates and rotates with the top of the tower, and it yaws with the nacelle. The origin is at the top of the tower (tower axis) with the x-axis pointing downwind end of the nacelle, the y-axis pointing to the port, and the z-axis perpendicular to these two axes.

Figure 12b shows the shaft, hub, and blades coordinate systems. The shaft coordinate system does not rotate with the rotor, but it does translate and rotate with the tower and yaws with the nacelle. The origin is on an intersection of the cross-sectional plane and shaft axis, with the x-axis pointing along the shaft in downwind, the y-axis pointing to the left when looking toward the downwind, and the z-axis orthogonal with these two axes. The hub coordinate system rotates with the rotor and provides azimuth position of the blades. The origin locates at an intersection of the rotor axis and the plane of rotation with the x-axis pointing along the hub centerline in downwind direction, the y-axis orthogonal with the x-axis and z-axis, which the z-axis is perpendicular to the hub centerline. Finally, there is a blade coordinate system for each blade that rotates with the rotor. It pitches with the blade and the origin is at an intersection of the blade pitch axis and the blade root. The x-axis is orthogonal with the y-axis and z-axis. The y-axis points toward the trailing edge of the blade at the zero-twist blade station. The z-axis points along the pitch axis toward the tip of blade.

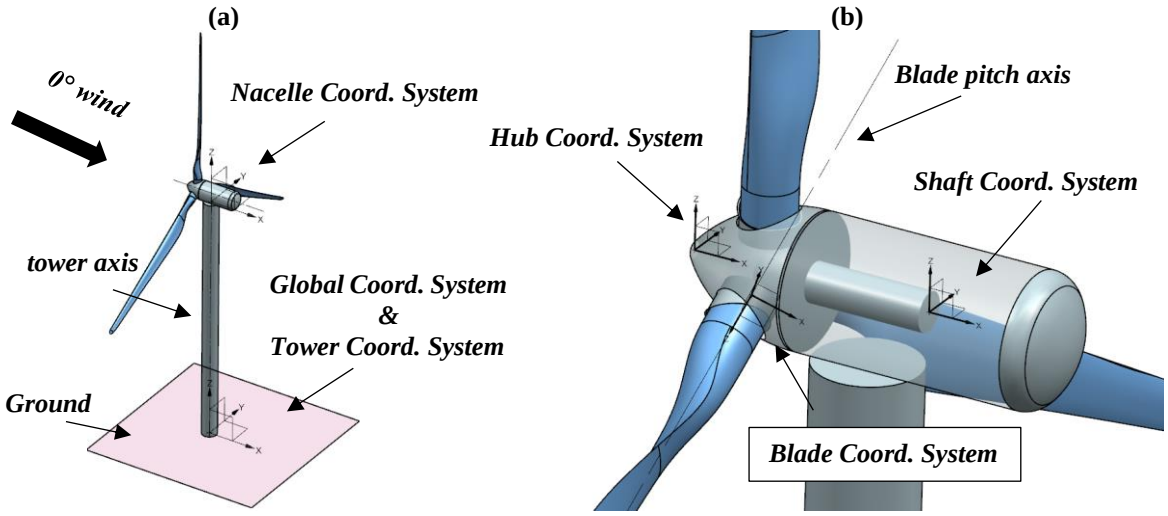

Figure 12: FAST coordinate systems of a 3-bladed wind turbine: **(a)** global, tower, and nacelle coordinate systems **(b)** shaft, rotor, and blade coordinate systems (identical to the IEC standards) [43].

2.2 NREL FAST

FAST is a driver code that couples various modules to simulate aerodynamic and dynamic responses of a wind turbine as shown in Figure 13. It has the capability of simulating a 2-bladed or 3-bladed wind turbine with a fixed-bottom or floating system.

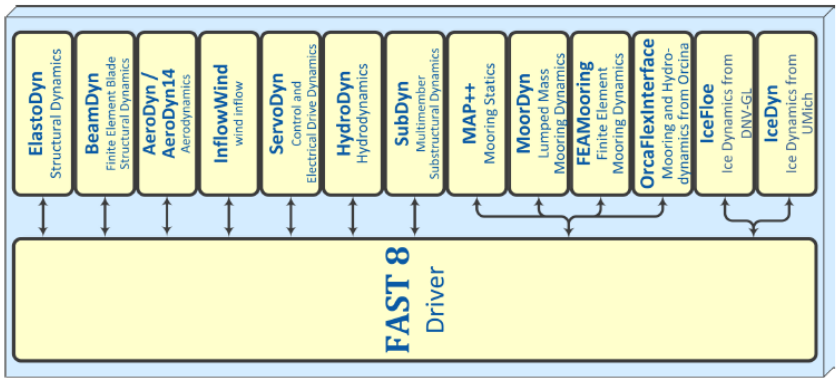

Figure 13: FAST v8.0 Architecture and list of all the modules [7].

FAST is a powerful tool for wind turbine simulations due to its modularity. The users can freely choose the modules to enable. The users need to prepare primary input files for each module and request desired outputs. Since this study focuses on aerodynamic noise of an operating turbine rotor, only four modules are used in FAST: *InflowWind* (v3.03.00a), *AeroDyn* (v15.03.00), and *BeamDyn* (v1.01.04), and *ElastoDyn* (v1.04.00a). Therefore, the FAST v8.0 architecture used specifically for this study is shown in Figure 14. It is important to mention that when integrated

with WTNoise, *InflowWind* takes parameters (wind speed, reference height, and power-law exponent) from the numerical data on the wind profile in WTNoise. The figure shows that *InflowWind* generates wind profile as an input for *AeroDyn*. The blade aerodynamics are then computed and transferred back to FAST for *BeamDyn* blade aeroelastic calculations. *ElastoDyn* performs motion simulations of the wind turbine rotor (blade rotational motion). *BeamDyn* takes the rotor motion from *ElastoDyn* and aerodynamic loads from *AeroDyn* to perform structural dynamic modeling on the blades. FAST orchestrates these 4 modules and transfers loads and responses between *AeroDyn*, *BeamDyn*, and *ElastoDyn* to enable fluid-structural interactions at each computation time step [7]. Therefore, the blade becomes flexible while using FAST for wind turbine noise predictions. For the cases of rigid blades, a standalone version of *AeroDyn* (v.15.03.00) is able to compute required aerodynamic parameters for wind turbine noise predictions.

The FAST simulation is performed in the time domain, where a wind turbine rotor undergoes transient and steady states in terms of aerodynamics, blade deflection, or power generation. There are transient responses until the rotor reaches the steady state. The noise calculation is performed using the FAST result in the steady state condition, i.e. the steady-state wind turbine noise prediction. A typical simulation requires the rotor to make 2~3 revaluations to achieve its steady-state condition. However, for a large wind turbine simulation, such as NREL 5MW wind turbine (rotor diameter 128 m), it reaches a steady-state condition after 20 seconds of simulation time or after 4^{th} revolution at the rated rotor speed. Therefore, the simulation time is long enough to ensure the transient responses has died out. In addition, the result (aerodynamic parameters and blade deflections) are only collected from the last revolution of a wind turbine rotor within the simulation time.

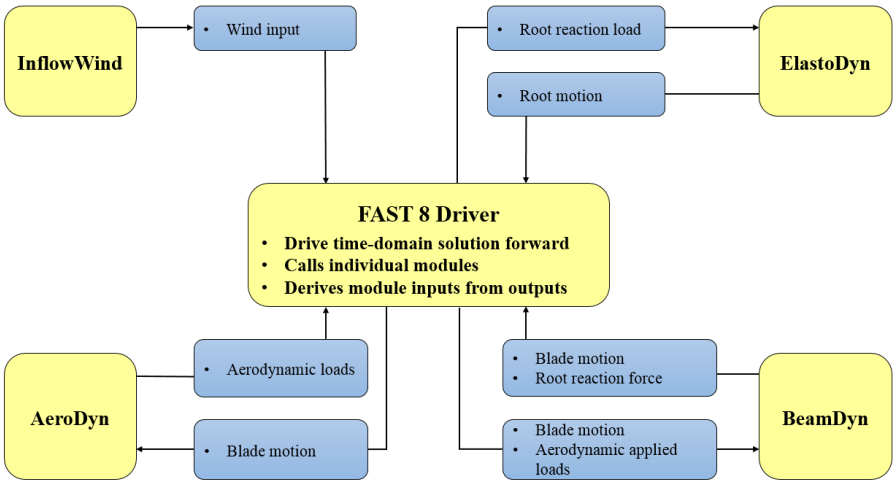

Figure 14: FAST v.8 modules used in this study.

All modules require several input files as listed in Table 5. The FAST itself requires a primary input files that set the simulation configurations and modules to use. All the modules require a primary input file that establishes modeling configurations and parameters, or paths to other required files. For example, although the wind turbine tower dynamics is not an interest of this study, *ElastoDyn* still requires a tower model as a separated file and a primary file that specifies the wind turbine configurations (number of blades, hub radius and height, etc.) and initial conditions (initial blade pitch angle, rotor speed, etc.) in order to execute a FAST simulation. For *AeroDyn*, besides its primary input file that specifies the modeling options and environmental conditions, there are other two important input files: several Airfoil data files and a single Blade data input file. Each Airfoil data file contains coefficients of lift, drag and pitching-moment (optional) versus AoA (from -180° to 180°) for a particular airfoil. The number of Airfoil data files depends on the blade design, i.e., if a blade is designed with 3 airfoils, *AeroDyn* requires 3 Airfoil data files. An *AeroDyn* blade data input file contains the nodal discretization, geometry, twist, chord, and airfoil identifier (identifying the airfoil type from the Airfoil data files) for a blade. For *BeamDyn*, the primary input file defines the blade axis with initial twist angles, FEA modeling and simulation options. A *BeamDyn* Blade input file is required to perform FEA of the blade. It defines the cross-sectional properties at various stations along the blade and six damping coefficient for the whole blade. Details of each input file from these modules are discussed in the following subsections.

Table 5: List of required input files for FAST v8 modules used in this study.

FAST v8		
Module	**Input file**	**Content**
FAST	Primary Input file	● Simulation control, e.g. run time and time-step ● Module switch ● Paths of the module input files
InflowWind	Primary input file	● Wind profile parameters: flow velocity, reference height, power law exponent. ● Output request
AeroDyn	Primary input file	● BEM correction options ● Environmental condition: air density, air viscosity, speed of sound. ● Path to other input files. ● Output request
	Airfoil data files	● Table of coefficient of lift force, drag force, and pitching moment versus angle of attack of an airfoil. Each airfoil requires one data file.
	Blade data input file	● Number of blade nodes for analysis ● Blade span, out-of-plane offset distance and angle for blade curvature, in-plane offset for blade sweep, aerodynamic twist angle, airfoil chord length, airfoil type at each node
BeamDyn	Primary input file	● Simulation control: number of iteration and tolerance ● Beam axis parameter: key point coordinates and number of element ● Order of shape function for each element ● Path to blade input file ● Output request
	Blade input file	● Blade structure damping coefficient ● Number of cross-sectional station along the blade axis ● Sectional 6X6 mass and stiffness properties
ElastoDyn	Primary input file	● Wind turbine DoFs. ● Wind turbine initial conditions and configuration ● Wind turbine component mass and inertia ● Path to the tower model file ● Output request
	Tower model file*	● Tower sectional properties: mass density, fore-aft, stiffness, side to side stiffness. ● Tower fore-aft mode shape ● Tower side-to-side mode shape

*Tower model file is required but has no influences on any of the numerical predictions.

The code FAST can generate large amounts of output data. However, Table 6 shows a list of the required outputs that are used in the proposed approach for wind turbine noise predictions in this thesis. Wind velocity at the reference height, e.g. the wind turbine hub height, is requested from *InflowWind* for validating the correct wind profile. Rotor azimuth angle (the azimuth angle of the first blade) is requested from *ElastoDyn* to obtain azimuth positions of the blades. The first blade

is pointing vertically when $\varphi = 0$ and positive in clockwise rotation, looking from the upwind. Aerodynamic parameters, e.g. inflow wind speed and AoA are requested from *AeroDyn* for the airfoil-self noise modeling. Finally, the blade deflection from *BeamDyn* is requested not only for visualizing blade deformation, but also aeroacoustic noise modeling that may be affected by the blade deflections.

Table 6. Desire outputs from FAST v8 for the noise modeling.

FAST v8		
Module	**Desire Outputs**	**Purpose**
InflowWind	Wind velocity at reference height	Checking on wind profile
ElastoDyn	Rotor azimuth angle	Noise modeling, Visual
AeroDyn v15.0	Inflow wind speed Angle of attack	Noise modeling
*BeamDyn**	Translational deflection (x, y, z in IEC standard blade coordinate system)	Blade deformation, Visual

*BeamDyn is capable of giving rotational deflections in Wiener-Milenković parameters, but these outputs are incorrect due to bugs in BeamDyn. NREL is looking into it and plan to release a correction soon [44].

2.2.1 *InflowWind*

InflowWind is a module for processing wind inflow data. It can either create a steady wind condition or read other wind files, such as binary *TurbSim* full-field (FF), binary Bladed-style FF, and HAWC formatted binary FF wind files [45]. These wind files are often generated from *TurbSim*, a preprocessor for a full-field and turbulence wind field by NREL [46]. In *InflowWind* the power-law wind profile is given as

$$V_h(z) = V_r\left(\frac{z}{z_r}\right)^{\alpha} \tag{1}$$

where V_r is wind speed at reference height, z_r, and α is power-law exponent. *InflowWind* also allows users to change the angle of wind. The principle is to rotate the wind field about the z-axis as shown in Figure 15. In this study, there is no vertical component (in the z-axis) of the wind.

Figure 15: The coordinate system used in *InflowWind* [45].

2.2.2 *AeroDyn v15*

AeroDyn is a code that calculates aerodynamics of wind turbine blades. The principle is based on the classical BEM model that was developed from Galuert [47]. BEM model is the most common method for calculating wind turbine aerodynamics due to its accuracy and computational efficiency. AeroDyn v15 employs an unconventional BEM solving algorithm that is a modification of the classical BEM theory based on Ning's work [48]. The new BEM solving algorithm that implemented in AeroDyn v15 has advantages of faster solution time and guaranteed convergence. Instead of having the BEM equations as a function of the axial and tangential induction factors and solving the fixed point problem $(a, a') = f(a, a')$ using iteration scheme of Newton's method (the conventional BEM solving algorithm), Ning reduces the BEM equations into one equation. The unknowns in the BEM equations change from the traditional axial and tangential induction factors to only the local inflow angle, φ. In addition, *AeroDyn* includes more details to capture the complexity of flow dynamics, such as corrections on tip-loss, hub-loss, skewed-wake, etc. Besides the blade aerodynamic calculation, it also accommodates tower shadow, vertical wind shear, horizontal wind shear, and unsteady inflow (turbulence) effects. *AeroDyn* v.15 and this new BEM solving algorithm have been validated and have a good agreement with experimental data [42] . The result showed that yawed or tilted inflow, e.g. vertical sheared or horizontal sheared wind components, could be accounted for in the calculation. The formulations and details of the classical BEM and Ning's solving algorithm can be found in Appendix A: Classical BEM and AeroDyn v15 and [42, 48].

AeroDyn uses the BEM that is based on the principles of actuator lines, in which the three-dimensional (3D) flow around a blade is approximated by local two-dimensional (2D) flow at the cross sections, and the distributed pressure and shear are approximated by lift, drag, and pitching moments lumped at a node in a 2D cross section. The analysis nodes are distributed along the blade span by as shown in Figure 16 depending on how the blade is modeled. *AeroDyn* is used for both rigid and flexible assumptions. For cases of rigid blade assumption, a standalone version of *AeroDyn* is utilized. It has the same capability of capturing fluid dynamics of complex flows without considering the blade aeroelasticity. When used in FAST, *AeroDyn* takes into account blade aeroelasticity in the aerodynamic calculations, i.e. the deformation of the blade as it rotates is incorporated in to the aerodynamic calculation. When *AeroDyn* is used in FAST, *AeroDyn* receives the instantaneous undisturbed inflow wind, deflected blade structural position, and orientation to compute the aerodynamics on the analysis nodes of the blade. The wind and blade structural calculations are computed from *InflowWind* and *BeamDyn*, respectively, and passed as inputs to *AeroDyn* by FAST. The motions of blades are provided at each simulation time step and then *AeroDyn* calculates the nodal aerodynamic loads and returns them back to *BeamDyn* as part of the blade aeroelastic calculation [39].

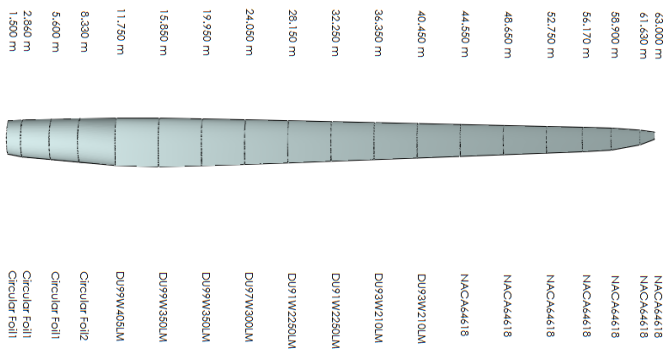

Figure 16: Illustration of AeroDyn analysis nodes on an NREL 5MW blade. Each node along the blade span corresponds to a particular airfoil as shown on the bottom.

When using the standalone version of *AeroDyn*, it requires four input files: a driver input file, a primary input file, airfoil data files, and a blade data input file. The driver input file is only required in the standalone version of *AeroDyn.* The purpose is to specify the wind condition (power-law wind profile only) and the turbine configuration (number of blades, hub height and radius, overhang, tilt, etc.). Using *AeroDyn* with FAST does not require a driver input file because the

wind condition and the turbine configuration are specified in the *InflowWind* and *ElastoDyn*. In the primary input file, the BEM theory with Prandtl's tip loss is enabled to account for energy losses from the blade tip. The airfoil data file contains a table of lift, drag, and pitch moment (optional) force coefficients versus angle of attack for the airfoil. This file can be generated using a pre-processor, *AirfoilPrep*, from NREL [49].

The *AeroDyn* blade data input file contains the blade nodal location, geometry, twist, chord, and airfoil identifier for a blade as shown in Figure 16. The blade analysis is done by dividing the blade into multiple nodes. Each node requires specifications of the local span along the blade pitch axis from the root, local out-of-plane offset and angle for blade curvature, local in-plane offset for blade sweep, local twist angle of airfoil, local chord length, and indicator of airfoils. The parameters that define blade curvature and sweep are illustrated in Figure 17. ***It is important to mention that influences of blade sweep and curvature are eliminated in this study, i.e. wind turbine noise predictions are based on straight blades that only have varying pitch angles and chord lengths.***

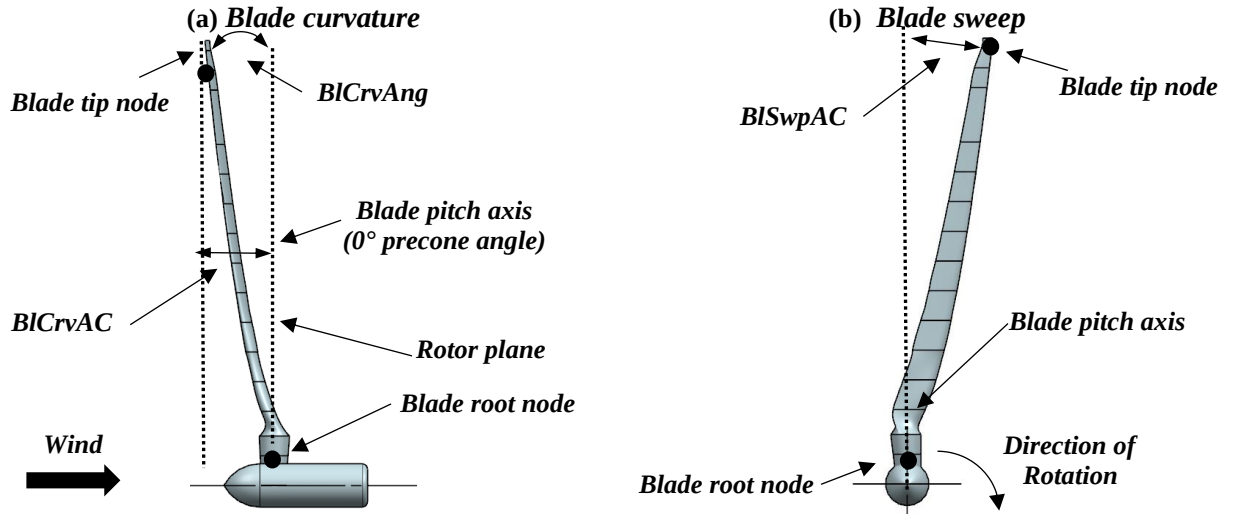

Figure 17: Illustrations of blade curvature and sweep: **(a)** local out-of-plane offset *(BlCrvAC)* and angle *(BlCrvAng)* and **(b)** local in-plane offset *(BlSwpAC)* (front view). The blade curvature and sweep are not included in this study.

2.2.3 *BeamDyn*

BeamDyn is a time-domain structural-dynamic module for rotor blades developed by Wang [50]. It calculates the blade deflections (translational and rotational displacements) and responses (forces and moments) by taking inputs (aerodynamic loads) from *AeroDyn*. *BeamDyn* models turbine blades as cantilevered beams fixed at the blade roots. This is a common modeling approach

for wind turbine blade analysis. *BeamDyn* employs Geometrically Exact Beam Theory (GEBT) based on the work of Hodges [25]. GEBT models the beam geometric nonlinearity and large deflection including bending, torsion, and shear. The key concept of GEBT is that a 3D nonlinear beam problem is decoupled into a linear 2D cross-sectional problem over the cross-section and a nonlinear 1D geometrically exact beam analysis over the beam reference line. The 2D cross-sectional analysis creates sectional properties in the form of 6X6 mass and stiffness matrices of a non-uniform cross-section beam. The sectional properties and loads are inputs to the 1D GEBT beam model to compute the dynamic responses of a blade. *BeamDyn* also supports a blade that is initially curved or swept as shown in Figure 17. In addition, it supports anisotropy material of a beam by using the sectional properties that are able to capture bending and twist coupling effects in composite materials typically used in most large wind turbine blades. The GEBT beam model's spatial discretization is accomplished with Legendre Spectral Finite Elements (LSFEs), resulting in high accuracy with few elements that have high order of the element shape functions [51]. *BeamDyn* developers and Wang have done numerical predictions and validations that confirm a long, flexible, composite blade can be modeled with a single element with high order of the element shape functions and few nodes (<10 nodes). [50-52]. BeamDyn is able to output six displacements (three translations and three rotations), velocities, and accelerations, as well as the resultant forces and moments at the beam nodes laying on the model axis. ***These displacements are used in AeroDyn via FAST, i.e. the resultant aerodynamic parameters take account of the aeroelastic effects.*** For calculations and visualization purposes, the blade deformation is used and plotted using the *BeamDyn* displacement output in this thesis. However, *BeamDyn* has an error where the rotational displacement outputs by the code are wrong. ***In other words, the calculation of aerodynamic parameters that incorporate the blade deformation is computed correctly by AeroDyn with FAST. Only the rotational displacement output from BeamDyn is incorrect.*** Since the rotational displacement is needed in the orientation of the noise sources, in this thesis the rotational displacements are estimated using the BeamDyn outputs as explained next.

The three sectional rotations for a deformed blade are about its *x*-axis, *y*-axis, and *z*-axis in the local blade coordinate system as shown in Figure 12b. The rotational displacement about the blade *x*-axis is neglected due to its high stiffness. Only the rotational displacements about *y* and *z*-axis are of interest. The rotational displacement about *y*-axis is due to the deflection of the blade axis

in the downwind direction. As shown in Figure 18, the blade axis is no longer straight and curved in the downwind direction. Therefore, the blade cross-sections rotates which in turns affect the directivity of the airfoil noise source. This rotation can be understood as an additional local blade cone angle as a function of the blade span, i.e. the value depends on how much the blade deflected along the blade span. To determine this deflection angle, the approach is to estimate the slope of the deflected beam axis as defined as

$$\psi(z) = \frac{dv(z)}{dz}$$

where $v(z)$ is the deflection in the downwind direction. For ease of visualization, the deflection in Figure 18 is amplified by a factor of 5. For example, a 100 m long turbine blade has *y*-axis rotational displacement, 9.2°, under a 14 m/s uniform wind.

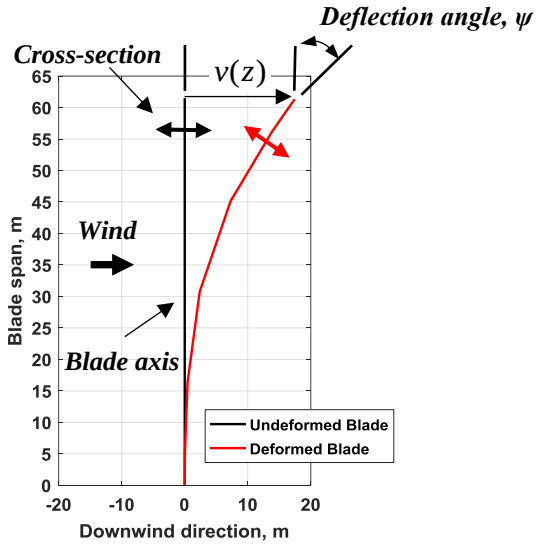

Figure 18: Illusions of the blade deflection angle due to blade axis deformation. The deflection is scaled up by a factor of 5 for illustration purposes.

The rotational displacement about the blade *z*-axis can be understood as an additional twist deformation of the airfoil. It is due to the aerodynamic moment on the airfoil that causes the cross-section to rotate along the blade *z*-axis. Figure 19 shows a blade cross-section and the definition of several aerodynamic angles. For rigid blade cases, the blade twist is constant. However, for a flexible blade case, as the blade deforms the blade twist is no longer a constant, which leads to change in AoA (captured in *AeroDyn*) and the noise source orientation. In this thesis, the rotational

displacement along the blade *z*-axis is estimated as the change in AoA between the rigid and flexible blade cases. The deformed twist angle, θ, is estimated as

$$\theta \cong \alpha_{rigid} - \alpha_{flexible}$$

where α_{rigid} and $\alpha_{flexible}$ are AoAs of the rigid case blade and flexible blade, respectively. For the NREL 5MW blade under a uniform wind at speed 11 m/s, the *z*-axis rotational displacement at the blade tip is very small (~1°). This is a very small angle and thus this rotation is ignored in the formulation.

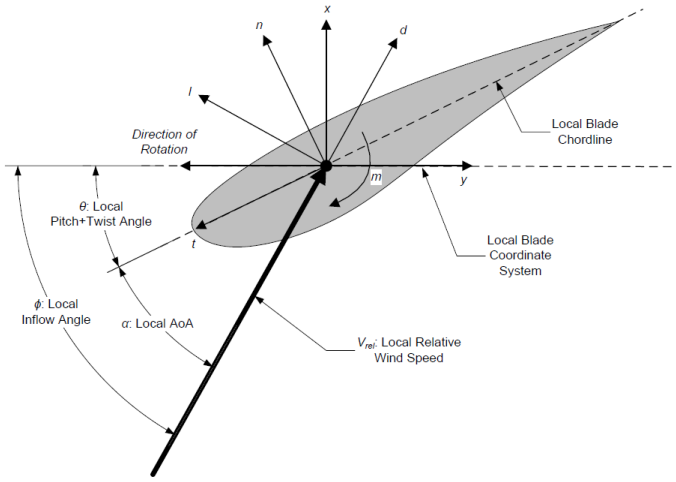

Figure 19: Local blade coordinate system looking from the blade root (z-axis is pointing into the page) [39].

BeamDyn requires two input files: primary and blade input file. In the primary input file, there are three important user inputs: key points that define the beam reference line, order of shape function for each finite element (related to the number of FE nodes), and *BeamDyn* blade input file path that contains sectional 6×6 mass and stiffness matrices at each station.

It is important to mention the differences between the key points, FE nodes, and stations in *BeamDyn*. ***The key points only define the geometry of the beam reference line, e.g. blade pitch axis.*** They are unrelated and independent from the FE nodes and stations. A beam reference line is used for the 1D GEBT governing equations. An example of how the key points define a beam reference axis as a single FE member (element) is shown in Figure 20a. Each key point is defined by three physical coordinates (*k_x*, *k_y*, and *k_z*, [50]) in the IEC standard blade coordinate (shown in Figure 12b) along with a structural twist angle. For an initially curved or swept blade, *k_x* and

k_y are non-zeros, indicating that the blade axis is not straight. A straight blade will have *k_z* values distributed along the blade span. Figure 17 shows illustrations of a blade with curvature or sweep. Again, blades are assumed to be straight without sweep and curvature in this study.

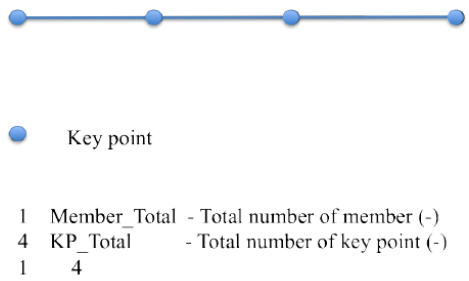

Figure 20: Illustration of a beam axis defined by the key points in BeamDyn [50].

The order of the shape function is related to the number of FE nodes and time-step size in the FAST simulation. The number of *BeamDyn* FE nodes, *n*, depends on the order of shape function, *p*, in a finite element. Based on the characteristics of LSFEs, the number of the FE nodes is defined as $n = p + 1$. ***In LSFE approach, the shape functions are pth-order Lagrangian interpolants, where nodes are located at the Gauss-Lobatto-Legendre points as Figure 98 shows. The user cannot change the location of the nodes.*** Higher order of the shape function leads to higher number of the nodes, but also requires smaller time-steps. For example, a reference FAST simulation of NREL 5MW turbine that has $p = 5$ (6 FE nodes), requires a time-step equal or smaller than 0.08 second. For a simulation case of $p = 8$, the time-step may need to be refined to at least 10^{-3} second [53]. Studies has shown that additional *BeamDyn* FE nodes would not the increase accuracy of a result. Wang has demonstrated that the convergence of tip-displacement on NREL 5MW blade can be achieved with only 6 nodes (in one single element) [53].

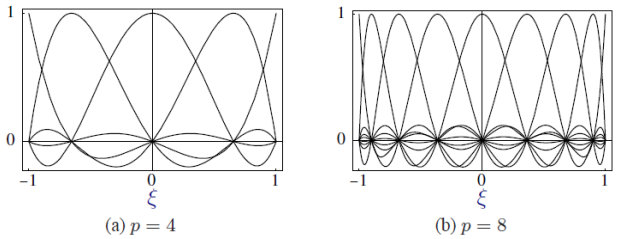

Figure 21: Illustrations of Lagranigant shape functions in the element natural coordinates for **(a)** fourth- and **(b)** eight-order LSFEs, where nodes are located at the Gauss-Lobatto-Legendre points [51].

In *BeamDyn*, a station is related to the numerical integration (quadrature) of the GEBT finite element analysis. Each station represent a quadrature point that is applied to the integrations of LSFEs, e.g. stiffness matrix. ***The material sectional properties, e.g. 6X6 mass and stiffness matrices, are defined at stations along the beam axis.*** The stations are distributed along the blade axis, but the number of stations and their locations along the blade span are based on the user input. *BeamDyn* employs trapezoidal-rule (TR) quadrature that is able to capture dramatic changes of sectional material properties along a modern turbine blade with few FE nodes. Wang has yielded an accurate blade deflection results that used 6 FE nodes and 49 stations distributed along a NREL 5MW blade [53].

Therefore, the blades in this thesis are modeled as a single element with 6^{th} order of shape functions, i.e. 7 FE nodes along the blade. However, the number of stations is not consistent between each blade design. It is depended on the structural properties provided by the designer. For example, Jonkman divided the NREL 5MW blade into 49 sections along the blade span and provided the sectional structural properties (see Appendix D: The NREL Blade Properties for the full table) [54]. Thus, 49 stations are created using these sectional structural properties of the NREL 5MW blade.

The *BeamDyn* blade input file indicates locations of the stations and the sectional material properties associate with them. For example, if a blade axis consists of 49 station, the user has to provide 49 sets of sectional material properties. For a blade cross-section without consideration of the composite coupling effects, the stiffness matrix at each station is defined as

$$M_i = \begin{bmatrix} K_{ShrFlp} & 0 & 0 & 0 & 0 & 0 \\ 0 & K_{ShrEdg} & 0 & 0 & 0 & 0 \\ 0 & 0 & EA & 0 & 0 & 0 \\ 0 & 0 & 0 & EI_{Edg} & 0 & 0 \\ 0 & 0 & 0 & 0 & EI_{Flp} & 0 \\ 0 & 0 & 0 & 0 & 0 & GJ \end{bmatrix} \quad (2)$$

where K_{ShrFlp} and K_{ShrEdg} are the flap and edge shear stiffness, respectively; EA is the extension stiffness; EI_{Edg} and EI_{Flp} are the edge and flap stiffness, respectively; and GJ is the torsional stiffness. The flap and edge shear stiffness associate with flap-wise and edge-wise shear deformations in the cross-section of the blade as shown in Figure 22a. The extension stiffness associates with the blade *z-axis* deformation. The torsional stiffness associate with the rotational deformation of the entire blade. The edge and flap stiffness associate with the flap-wise and edge wise deformation of the entire blade as shown Figure 22b. For a blade cross-section with a consideration of the composite coupling effect, the stiffness in all the DoFs may be coupled, i.e. the stiffness matrix may be fully populated. *BeamDyn* implemented 6 DoFs viscous damping coefficients (not damping ratio), where the damping forces are proportional to the stiffness matrix. The damping has benefits of convergence and stability during simulation, especially for computing blade deflections [52]. The damping coefficient matrix is defined as

$$\underline{\underline{\mu}} = \begin{bmatrix} u_{11} & 0 & 0 & 0 & 0 & 0 \\ 0 & u_{22} & 0 & 0 & 0 & 0 \\ 0 & 0 & u_{33} & 0 & 0 & 0 \\ 0 & 0 & 0 & u_{44} & 0 & 0 \\ 0 & 0 & 0 & 0 & u_{55} & 0 \\ 0 & 0 & 0 & 0 & 0 & u_{66} \end{bmatrix} \tag{3}$$

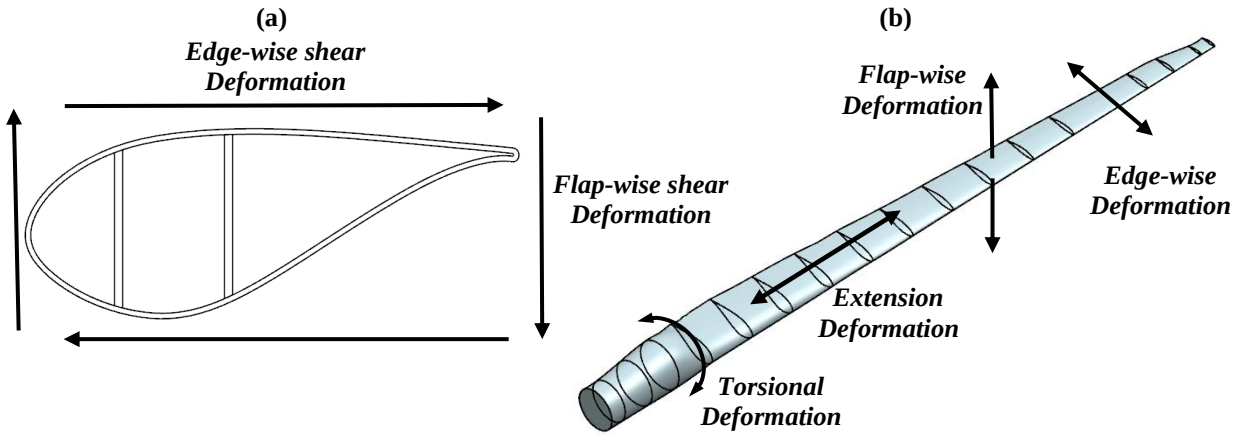

Figure 22: Illustration of stiffness DoFs in the *BeamDyn* 6X6 stiffness matrix.

BeamDyn defines a generalized sectional mass matrix by,

$$K_i = \begin{bmatrix} m & 0 & 0 & 0 & 0 & -mY_{cm} \\ 0 & m & 0 & 0 & 0 & mX_{cm} \\ 0 & 0 & m & mY_{cm} & -mX_{cm} & 0 \\ 0 & 0 & mY_{cm} & i_{Edg} & -i_{cp} & 0 \\ 0 & 0 & -mX_{cm} & -i_{cp} & i_{Flp} & 0 \\ -mY_{cm} & mX_{cm} & 0 & 0 & 0 & i_{plr} \end{bmatrix} \quad (4)$$

where m is the mass density per unit span; X_{cm} and Y_{cm} are the local coordinate of the sectional center of mass, respectively; i_{Edg} and i_{Flp} are the edge and flap mass moment of inertia per unit span, respectively; i_{cp} is the sectional cross-product of inertia per unit span; i_{plr} is the polar moment of inertia per unit span being defined as $i_{plr} = i_{Edg} + i_{Flp}$ for beam structure. For a blade with no curve, sweep, and sectional offset, mX_{cm}, mY_{cm}, and i_{cp} are set to zero, i.e. the blade modeled in this thesis have these parameters set to zero due to the straight blade assumption.

Note that the sectional material properties can be derived from several 2D sectional analysis tools, such as Variational Asymptotic Beam Sectional Analysis (VABS by Hodges [25]), BECAS (by Technical University of Denmark [55]), and NuMAD/BPE (by Sandia National Laboratories [56]). These methods are able to capture the composite coupling effects of a blade in its sectional stiffness matrices, as well as computing the mass matrices. However, these methods require detailed information on the blade design, such as the materials, blade structure (spar and shear web), and blade skin layout. This information is usually not publically available or requires other tools to obtain. Therefore, in this study, the dynamic modeling of the blade deflection does not account for the coupling effect due to insufficient information. The blade sectional properties are constructed based on publically available information that is discussed in Chapter 5.

2.2.4 *ElastoDyn*

ElastoDyn is a horizontal-axis wind turbine structural-dynamic module that employs a combination of modal and multibody formulations, i.e. combination of rigid and flexible bodies [43]. The primary purpose is to assemble wind turbine components via a series of equations of motion and constraints equations. The *ElastoDyn is* also capable of performing structural-dynamic

analysis (translational or rotational displacements, forces, or moments) on wind turbine components (nacelle, tower, platform, etc.) In addition, all the wind turbine configurations (i.e. 2 or 3-bladed, hub radius, and tip radius, etc.), turbine parameters (tilt, yaw, and pre-cone angles), and initial conditions (i.e. initial rotor speed, blade position, and pitch angle, etc.) are specified in this module via its primary input file. Besides the primary input file, *ElastoDyn* mandatory requires a tower model file that contains two important parameters: distributed tower properties and tower mode shape for the structural analysis.

In this thesis, ElastoDyn is used as a "motion simulation" of a wind turbine, i.e. only the kinematics of wind turbine components (rotor, drivetrain, nacelle, tower, and platform, etc.) are captured. The *ElastoDyn* is configured to that the turbine components are rigid, i.e. no translational or rotational displacement. By doing so, the effects of structural responses of wind turbine components will not influence the aerodynamics of the rotor due to FAST's fluid-structure coupling. The wind turbine will rotate constantly at the initial speed during the simulation time. The dynamic responses of the blades are computed by *BeamDyn*, so that *ElastoDyn* only handle the rotation of the blade.

In this thesis, the initial conditions are the initial, rotor speed, blade pitch and position (indicated as the generator azimuth angle), and nacelle yaw angles as shown in Figure 23a. Other initial condition parameters, such as initial translational and rotational displacements of the tower and platform, are set to zero to eliminate their influences on aerodynamics of the wind turbine. For the turbine configuration, number of blades, tip radius (distance from the rotor apex to the blade tip), hub radius, blade pre-cone angles, over-hang (distance along the rotor shaft from the rotor apex to the tower axis), shaft tilt angle, and tower height are also being specified. Figure 23b shows a schematics of these variables used in this study.

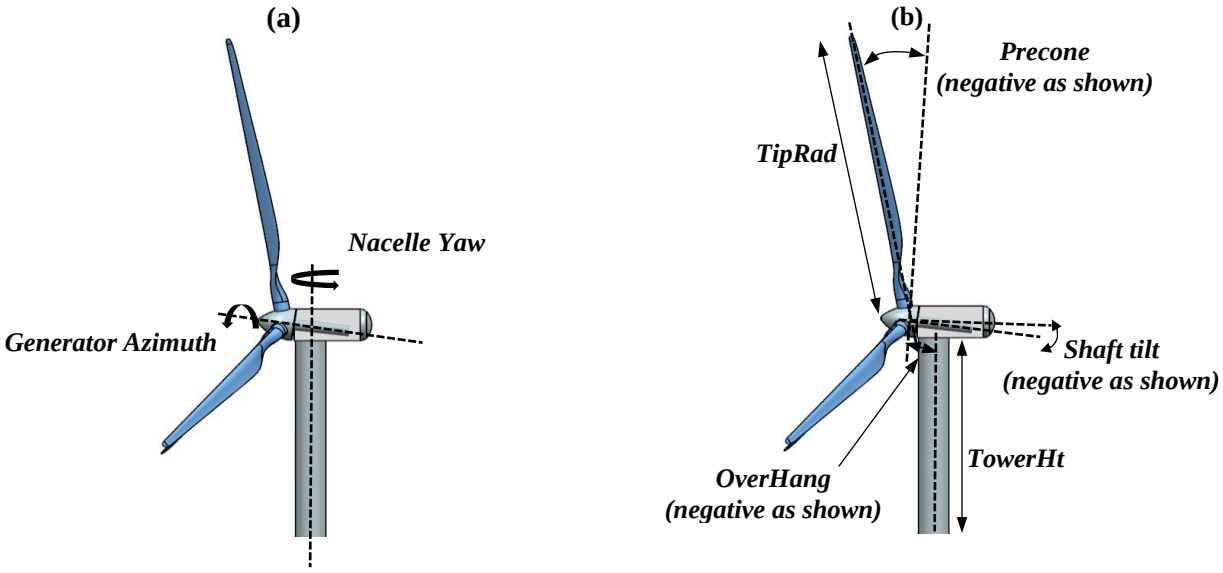

Figure 23: *ElastoDyn* turbine parameters for a 3-bladed wind turbine. See [43] for the parameter definitions.

The multibody kinematics and kinetics formulation of *ElastoDyn* is out of scope in this study. Many of its outputs are not used, such as displacements of the tower and nacelle. The desired output in this study is the azimuth angle of the first blade. It is used to indicate the blade position on the rotor plane for the noise calculation. In addition, the required tower file is simplified to a uniform cylinder instead of the conventional truncated cone shape. The structural properties is scaled based on the NREL 5MW tower. It is important to mention that the tower file has no significance in the turbine aerodynamics and noise predication. It is just one of the requirements to execute FAST properly.

2.3 FAST Example Case

For the sake of completeness, this section presents illustrative results of a FAST example case. These results were obtained by executing FAST independently from WTNoise. The case is based on the NREL 5MW wind turbine with 0° blade pitch, tilt of -5 °and pre-cone of -2.5° (see Figure 23 for the definitions). The tower and nacelle are assumed rigid and fixed at the ground. The stand-alone *AeroDyn* v15.0 was also utilized for the rigid blade case. The intention is to demonstrate how the aeroelasticity affects the aerodynamic parameters, e.g. AoA, and the blade deformation in the steady-state condition. The wind condition is uniform flow at the rated wind speed of 11.4 m/s without turbulence. Figure 24 illustrates the NREL 5MW turbine tip blade displacement for the rigid and flexible blade cases, respectively. For the rigid blade case, the blades do not deform when

they encountered incoming flow (shown in Figure 24a). In the flexible blade case, the blades go through a transient until they reach the steady-state condition as shown in Figure 24b.

The *BeamDyn* code computed the blade translational displacements. The average tip blade deflections in the *x*, *y* and *z* directions are 4.94, -0.61 m and -0.33 m, respectively. Therefore, the deflections in the blade *y*-axis and *z*-axis are disregarded. Figure 25a shows the steady-state blade tip deflection in the downwind direction (*x*-axis) as a function of blade 1 azimuth position. Notice that there are variations of the tip deflections (shown in dash lines) due to the rotor tilt angle that results in non-uniform loads over the blades even though the wind is uniform. For the case of zero tilt, pre-cone, and yaw angles, the blade deflection is constant over a revolution. The maximum tip deflection in the steady-state condition is 5.06 m using FAST v8.0, which is within 10% of the reported value, 5.5m (under the same wind condition and turbine configuration) by Jonkman *et.al* using FAST v7.0 [54]. It is important to mention that FAST v7.0 and FAST v8.0 employ different blade dynamic models, so that a slight difference is expected. For visualization purpose, Figure 25b shows the deformed blade 1 in 3 dimensions without amplification.

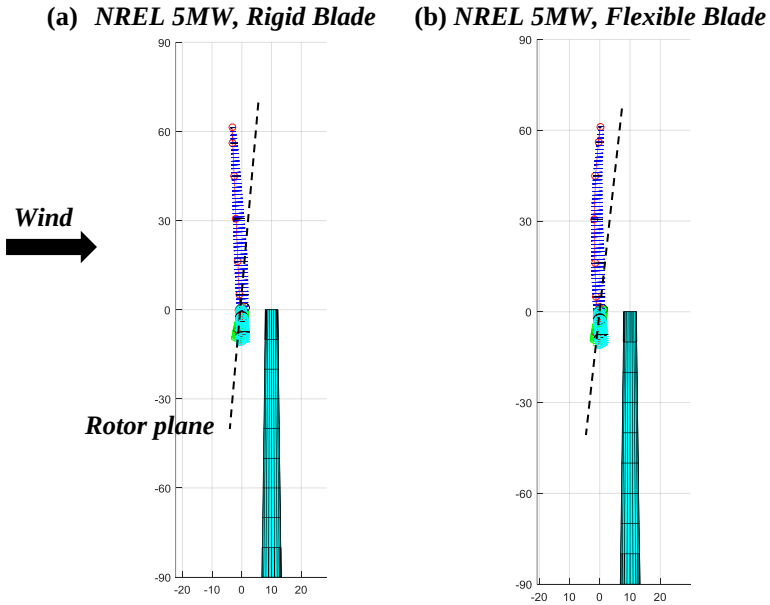

Figure 24: Illuminations of a NREL 5MW turbine with **(a)** rigid blade and **(b)** flexible blade cases.

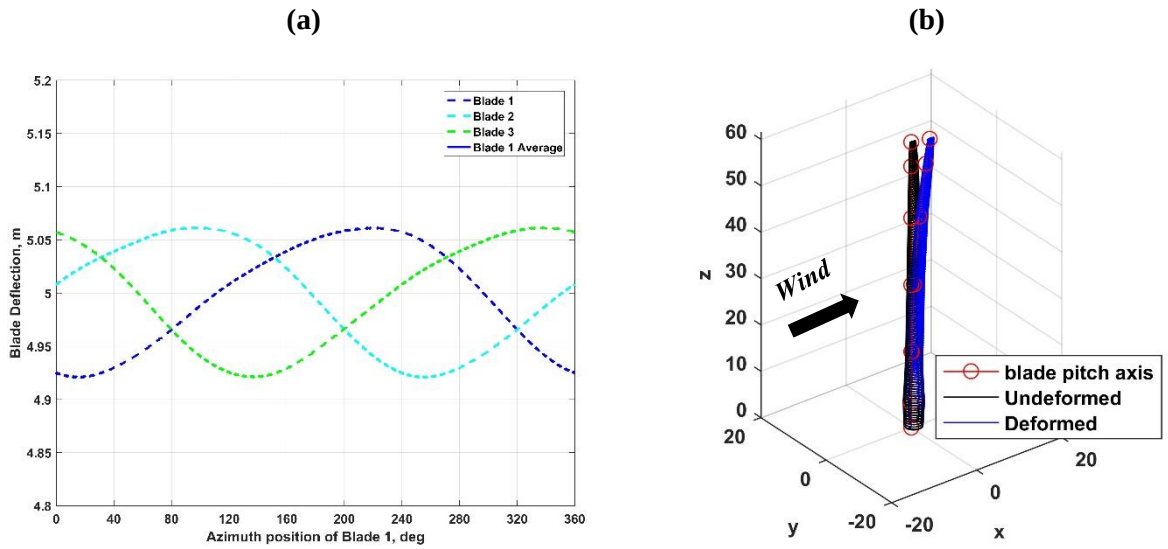

Figure 25: NREL 5MW blade translational displacements in **(a)** the x-axis (downwind) and **(b)** 3-dimensional without any amplification.

The rotational displacements are estimated using the methods described in Chapter 2.2.3. Figure 26a shows the deflection angle (rotation about the blade *y*-axis), ψ, at the blade tip *vs.* blade azimuth position. This angle varies from 8.85° to 7.85° in the steady-state condition. Figure 26b shows the AoA at the blade tip for the rigid and flexible cases computed by *AeroDyn* (rigid blade) and FAST (flexible blade), respectively. As expected, the AoA for the rigid blade is at a constant 4.9°. On the other hand, due to the blade flexibility the AoA fluctuates from 4.4 to 5.0°. Thus, the blade twist angle due to the blade flexibility (rotational displacement about the blade z-axis, which is estimated from changes in the AoA) is less than 1°.

For the noise prediction, blade deflection angles $\psi(z) > 5°$ may be important to consider in the noise source orientation. However, the change in twist angle due to the blade flexibility (rotational displacement along the blade *z*-axis) is too small (<1°) to have significant influence on the noise predictions.

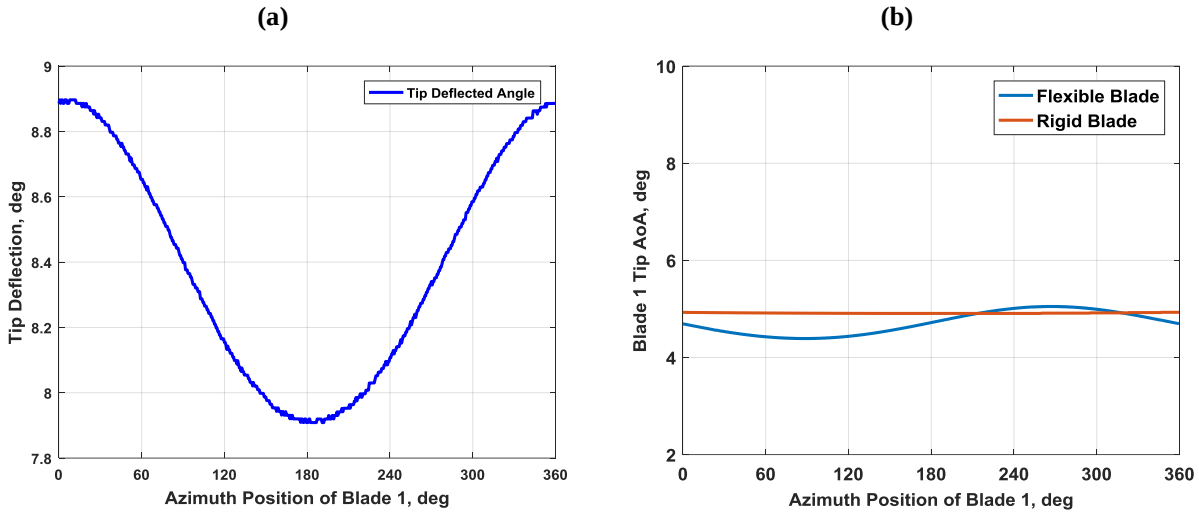

Figure 26: NREL 5MW blade **(a)** tip deflection angle (rotation about the *y*-axis) and **(b)** AoA for flexible and rigid blades.

Figure 27 shows the AoA distribution (from the blade span 30% to 100%) over the rotor plane for a revolution. Notice that AoA distributions in Figure 27 are axisymmetric and changes radially due to the uniform wind condition. If there is non-uniform inflow wind, the wind velocity variations will result in variations in the AoA distribution.

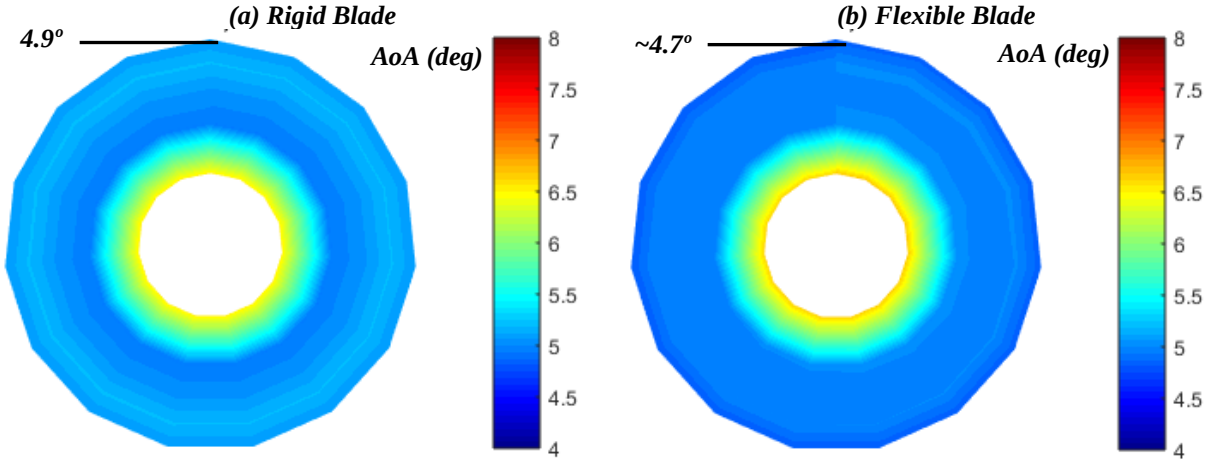

Figure 27: The AoA distribution over the rotor plane for **(a)** the rigid blade and **(b)** the flexible blade cases from 30% to 100% of the blade span (18.45 m to 61.5 m).

To demonstrate this, a flexible blade case with a non-uniform wind is performed. The turbine configurations and initial conditions are the same as the previous case, but the incoming wind has power-law profile with $\alpha = 0.4$ as shown in Figure 28a. The rotor top experiences high wind velocity, 14.1 m/s, which is higher than the rated wind speed (11.4 m/s) and leads to higher blade

deflections. This illustrates this phenomenon in Figure 28b. This figure shows the blade tip deflection over a revolution. At the blade top position, the blade deflection is the highest. The lowest blade deflection occurs at the bottom position where the wind velocity decreased to 6.9 m/s. The variation. The aerodynamic parameters experience the same trend throughout the blade azimuth position. For example, the AoA distribution (shown in Figure 29b) has higher value at the rotor top compared to the bottom.

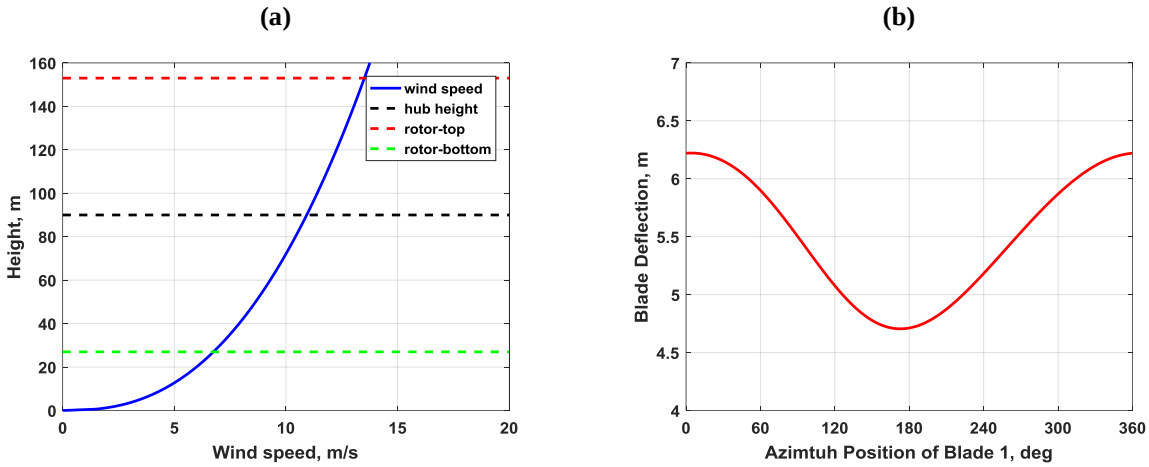

Figure 28: The flexible blade case under **(a)** non-uniform wind profile and **(b)** the blade tip deflection in the downwind direction.

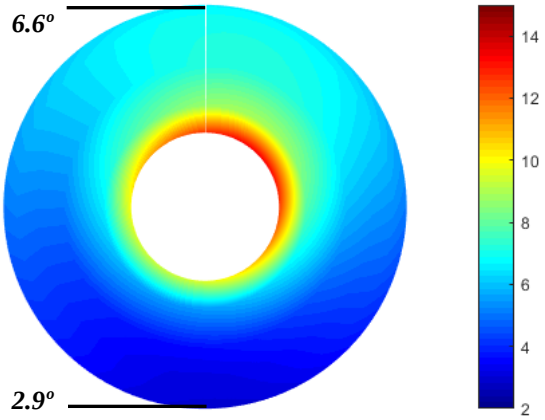

Figure 29: The flexible blade AoA distribution over the rotor plane under the non-uniform wind.

These cases have demonstrated that there are significant differences between rigid and flexible blade assumptions in the aerodynamic parameter calculation for large wind turbines.

3. WTNoise and Implementation of AeroDyn and FAST

WTNoise is a wind turbine noise modeling tool that included sound propagation in arbitrary weather over a flat terrain based on the work by Mcbride [38]. This section presents the acoustic models used in the tool and their fundamentals.

3.1 Introduction

The WTNoise consists of five modules as shown in Figure 30. The input to the code consists of the turbine and blade geometry, operating condition, atmospheric data, ground impedance, and execution control parameters.

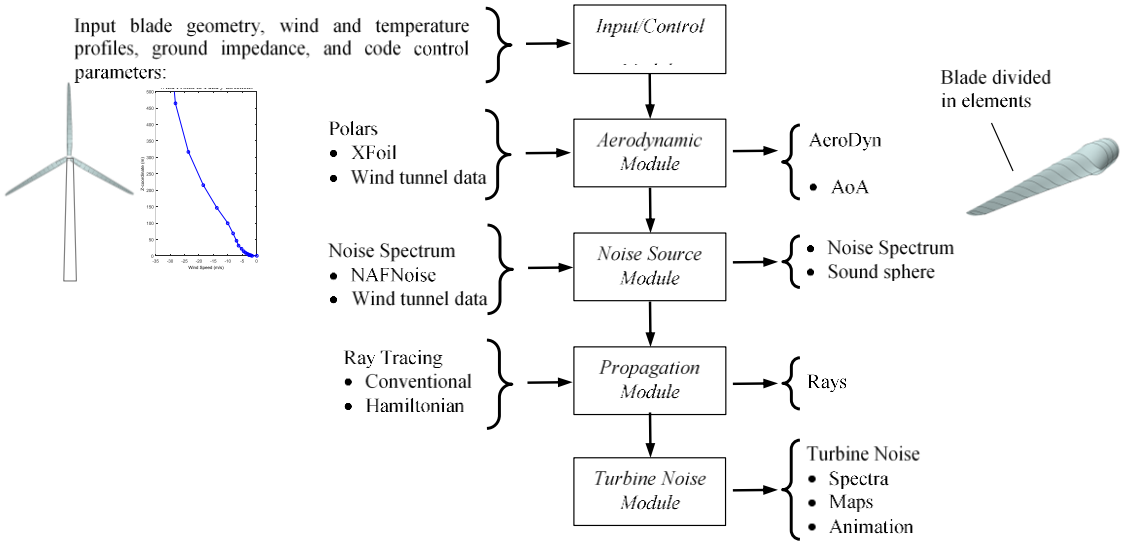

Figure 30: The schematics of WTNoise's turbine noise modeling approach [40].

The blades are then divided in span-wise direction elements and the blade rotation approximated as a discrete set of azimuth positions. As the result, this approach have a finite number of positions on the rotor plane to perform aerodynamic and noise calculations as shown in Figure 31a. The sound sources characterizing the turbine noise radiation will be defined at these points.

The second module is the *Aerodynamic Module*, which uses the BEM to compute the aerodynamic parameters needed for noise calculations [39]. The airfoil section polars are either computed using

XFoil [57] or taken from wind tunnel data [58]. Figure 31b illustrates the resulting AoA for all the positions shown in Figure 31a for a particular wind profile. The aerodynamic calculation in WTNoise was only an approximation that did not include the induction effects. In addition, it could not handle the turbine parameters, e.g. turbine tilt, pre-cone, and yaw.

The wind turbine aerodynamic noise generation mechanisms are governed by the flow conditions around the blades. In the *Noise Source Module*, the aerodynamic noise sources (leading and trailing edge noise) are computed for the selected blade elements in a set of azimuth blade position. This module uses the code *NAFNoise* [19] or wind tunnel data [58, 59] to predict the aerodynamic noise in 1/3rd octave bands at a single point in the direction normal to the airfoil chord line at a distance of 1 meter. The radiation directivity of the sources proposed by Brooks *et.al.* [17] is applied to define sound spheres to couple with the propagation module. Figure 31c shows an example of the resulting noise spectrum computed by *NAFNoise* for the position 4 in Figure 31a. As shown in Figure 31d, the resulting sound spheres centred at the trailing (or leading) edge of the airfoil elements are obtained by implementing the radiation directivity. The sound spheres show varying strength and directivity from the hub to the tip as consequences of the changing inflow, blade twist and airfoil geometry along the blade.

The next stage is the *Propagation Module* that implements a Hamiltonian ray tracing technique (HRT) for the noise propagation from the sound spheres shown in Figure 31d. For this module, it is compelling to implement all atmospheric meteorological conditions and their variability in order to simulate real physical phenomena. The critical parameters are temperature, wind, and relative humidity distributions. They affect the propagation behavior of sound in terms of the energy attenuation, absorption and sound propagation path. In addition, the terrain type and shape affect wind behavior, especially near the ground surface (induced turbulent flows). The HRT code's output includes the ray paths starting from the noise sources and propagating through the atmosphere (see Figure 31e) and the noise levels distribution in space. The WTNoise code currently has the limitation that atmospheric conditions are uniform over the domain but arbitrary with height.

The final module, *Turbine Noise*, concatenates ground level noise produced by the wind turbine sound sources as a noise map shown in Figure 31f. The noise from the different sources is summed incoherently at the ground microphone locations and binned according to arrival time. The noise spectrum at the microphone is computed over a uniform time sequence.

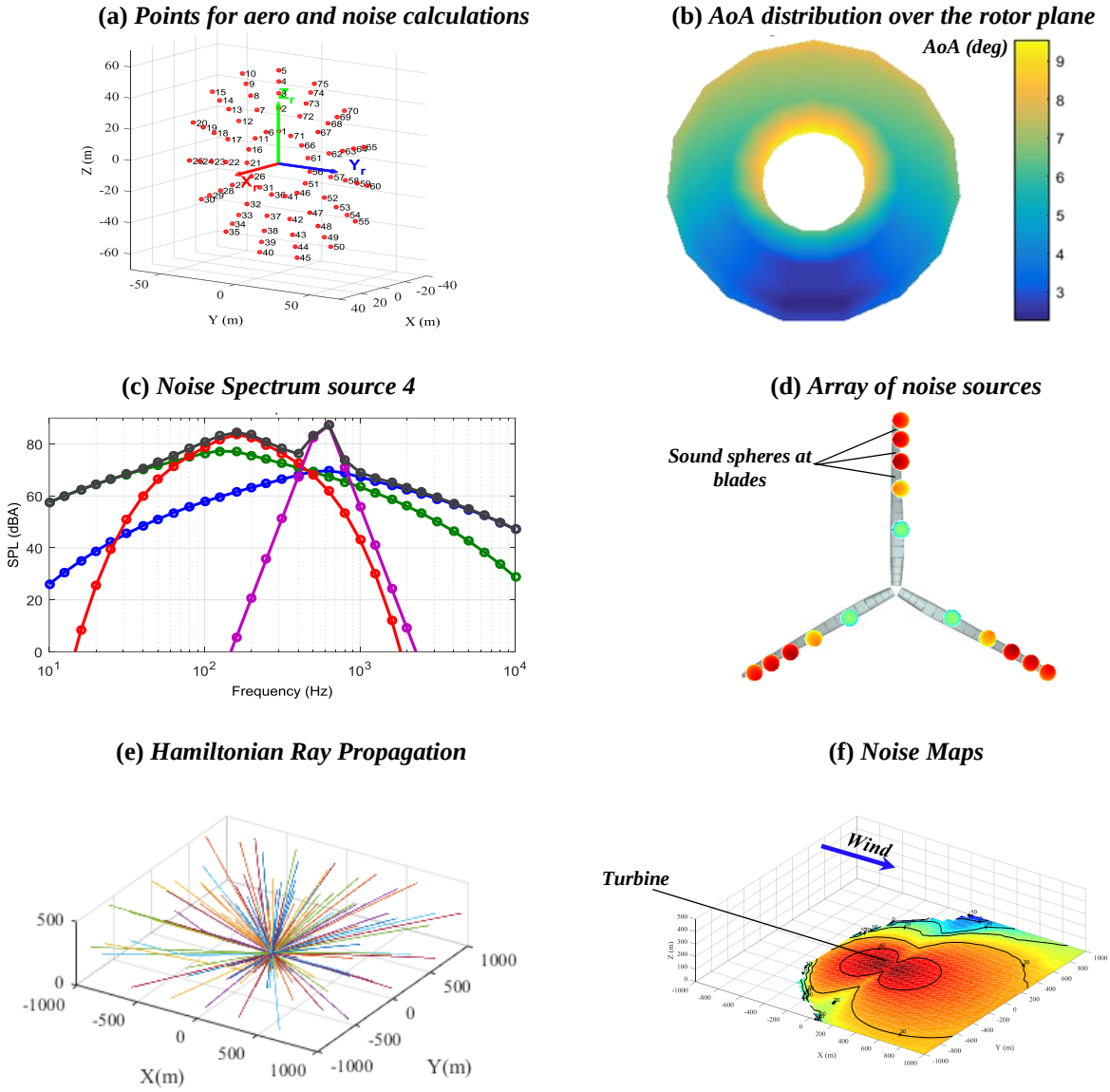

Figure 31: (a) Points on a rotor plane for the aerodynamic and noise calculation. **(b)** The AoA distribution over the rotor for one full rotation in a non-uniform flow. **(c)** Noise source spectrum computed by *NAFNoise* at position 4. **(d)** Sound spheres array for the wind turbine blades. **(e)** Ray paths of the Hamiltonian ray propagation. **(f)** The resulting OASPL noise map due to the turbine at 48° azimuth position.

The current version of WTNoise assumes rigid blades without rotor tilt or pre-cone and uses an approximate formulation for aerodynamic calculations. To extend the capabilities of WTNoise,

the stand-alone *AeroDyn* is implemented into the WTNoise for rigid blade cases. The stand-alone *AeroDyn*'s capabilities (mentioned in Chapter 1.2) improve the WTNoise aerodynamic calculation by including induction effects, empirical corrections, and the turbine's tilt, pre-cone, and yaw angles. Then FAST is implemented into the WTNoise *Aerodynamic Module* for flexible blade cases.

In the following subsections, some of the key aspects of WTNoise are presented to understand the integration of the stand-alone *AeroDyn* and FAST.

3.2 WTNoise Coordinate systems and rotation matrices

As shown in Figure 32, there are four coordinate systems in the WTNoise code: global, rotor, airfoil, and directivity. The global and rotor coordinate systems follows the IEC standard for wind turbines (Figure 32a). The global coordinate system (x_g, y_g, z_g) has its origin in at the tower center on ground with z-axis pointing upward, x-axis pointing downwind, and y-axis is perpendicular to them in accordance with the right hand rule. The rotor coordinate system (x_r, y_r, z_r) is located at the center of the rotor plane. This rotor coordinate system rotates with the rotor. Thus, for the case of zero tilt, yaw, and azimuth angles, the rotor and global coordinate systems are the same (no rotation relative to each other).

The WTNoise airfoil and directivity coordinate systems are needed to orient the aerodynamic noise source relative to the blade. The airfoil coordinate system (x_a, y_a, z_a) is shown in Figure 32b. The origin is located at the center of the blade element on the blade pitch axis. The z_a axis is aligned with the blade pitch axis pointing outward. The y_a is in the rotor plane for the pre-conned blade with x_a pointing downwind. Finally, the airfoil coordinate is attached to the blade and thus with the rotor. Thus, when the blade is in the up vertical position the airfoil and rotor coordinate system are essentially the same (no rotation relative to each other). The radiation directivity of the noise sources (TE and LE) is defined in terms of a local coordinate system (x_d, y_d, z_d) positioned at the TE as shown in Figure 32c. This system is denoted as directivity coordinate system, which is used in NAFNoise to define the noise source directivity relative to the airfoil (one of the blade elements). As an illustration, Figure 32d shows the baffled dipole directivity in terms of (x_d, y_d, z_d).

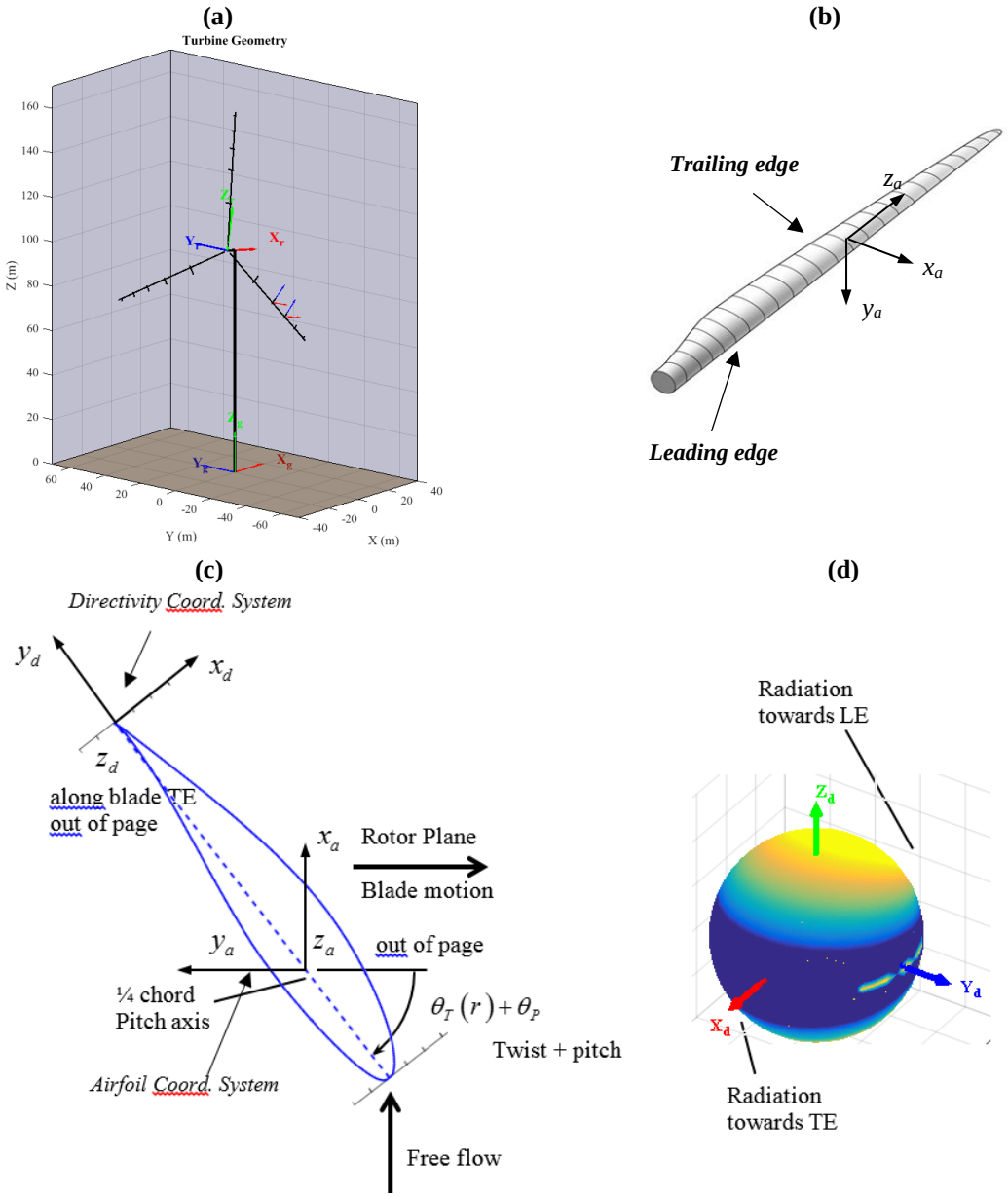

Figure 32: WTNoise coordinate systems: **(a)** global and rotor coordinate systems, **(b)** airfoil coordinate system for one of the blade elements, **(c)** directivity coordinate system on the airfoil element (the blade at zero azimuth angle looking from the negative z_g direction). **(d)** A baffled dipole sound spheres in the directivity coordinate system.

The four coordinate systems described allow for easily accounting for the yaw, tilt, pre-cone, azimuth, twist, and pitch angles when orienting the source radiation directivity. For sound propagation (propagation module), the directivity of the noise sources has to be expressed in the global coordinate system. To this end, a number of rotation matrices that links the four coordinate systems must be defined.

Global to Rotor Rotation

To account for the rotor yaw and tilt, the global and rotor coordinate systems are related by two rotation matrices as follows

$$\begin{Bmatrix} x_g \\ y_g \\ z_g \end{Bmatrix} = \begin{bmatrix} \cos(\phi_{yaw}) & -\sin(\phi_{yaw}) & 0 \\ \sin(\phi_{yaw}) & \cos(\phi_{yaw}) & 0 \\ 0 & 0 & 1 \end{bmatrix} \begin{Bmatrix} x_r \\ y_r \\ z_r \end{Bmatrix} = \left[R_{gr}^{yaw} \right] \begin{Bmatrix} x_r \\ y_r \\ z_r \end{Bmatrix} \tag{5}$$

$$\begin{Bmatrix} x_g \\ y_g \\ z_g \end{Bmatrix} = \begin{bmatrix} \cos(\phi_{tilt}) & 0 & \sin(\phi_{tilt}) \\ 0 & 1 & 0 \\ -\sin(\phi_{tilt}) & 0 & \cos(\phi_{tilt}) \end{bmatrix} \begin{Bmatrix} x_r \\ y_r \\ z_r \end{Bmatrix} = \left[R_{gr}^{tilt} \right] \begin{Bmatrix} x_r \\ y_r \\ z_r \end{Bmatrix} \tag{6}$$

where ϕ_{yaw} and ϕ_{tilt} are the yaw and tilt angles. The transformation from rotor to global is then

$$\begin{Bmatrix} x_g \\ y_g \\ z_g \end{Bmatrix} = \left[R_{gr}^{yaw} \right] \left[R_{gr}^{tilt} \right] \begin{Bmatrix} x_r \\ y_r \\ z_r \end{Bmatrix} \tag{7}$$

Rotor to Airfoil Rotation

The rotor and airfoil coordinate systems are related by the rotor pre-cone and the blade azimuth angle. When the blade is in the up vertical position, the pre-cone angle is a rotation about y_r. Then, the rotation of the airfoil coordinate system due to conning is given as follows

$$\begin{Bmatrix} x_r \\ y_r \\ z_r \end{Bmatrix} = \begin{bmatrix} \cos(\phi_{cone}) & 0 & -\sin(\phi_{cone}) \\ 0 & 1 & 0 \\ \sin(\phi_{cone}) & 0 & \cos(\phi_{cone}) \end{bmatrix} \begin{Bmatrix} x_a \\ y_a \\ z_a \end{Bmatrix} = \left[R_{r-a}^{cone} \right] \begin{Bmatrix} x_a \\ y_a \\ z_a \end{Bmatrix} \tag{8}$$

The blade then rotates about the axis x_r by the azimuth angle. Then rotation matrix that accounts for the azimuth angle is as follows

$$\begin{Bmatrix} x_r \\ y_r \\ z_r \end{Bmatrix} = \begin{bmatrix} 1 & 0 & 0 \\ 0 & \cos(\phi_{azimuth}) & -\sin(\phi_{azimuth}) \\ 0 & \sin(\phi_{azimuth}) & \cos(\phi_{azimuth}) \end{bmatrix} \begin{Bmatrix} x_a \\ y_a \\ z_a \end{Bmatrix} = \left[R_{r-a}^{azimuth} \right] \begin{Bmatrix} x_a \\ y_a \\ z_a \end{Bmatrix} \tag{9}$$

Therefore, the rotation matrix between the rotor and airfoil coordinate systems is

$$\begin{Bmatrix} x_r \\ y_r \\ z_r \end{Bmatrix} = \left[R_{r-a}^{azimuth} \right] \left[R_{r-a}^{cone} \right] \begin{Bmatrix} x_a \\ y_a \\ z_a \end{Bmatrix} \tag{10}$$

Directivity to Airfoil Rotation

The airfoil and directivity coordinate systems are related by the blade pitch and twist angles given by $\theta_T(r) + \theta_P$ where $\theta_T(r)$ and θ_P are the section twist and blade pitch angles and r is the radial position of the airfoil. Figure 32c shows the relationship of the airfoil and directivity coordinate systems. The rotation aligns the y_a axis with the y_d by rotating the airfoil coordinate system by $\theta_T(r) + \theta_P$ about the negative z_a axis. Then

$$\begin{Bmatrix} x_a \\ y_a \\ z_a \end{Bmatrix} = \begin{bmatrix} \cos(\tau(r)) & \sin(\tau(r)) & 0 \\ -\sin(\tau(r)) & \cos(\tau(r)) & 0 \\ 0 & 0 & 1 \end{bmatrix} \begin{Bmatrix} x_d \\ y_d \\ z_d \end{Bmatrix} = \left[R_{ad}^{pitch+twist}(r) \right] \begin{Bmatrix} x_d \\ y_d \\ z_d \end{Bmatrix} \tag{11}$$

where $\tau(r) = \theta_T(r) + \theta_P$. Note that because the twist angle depends on the radial position of the airfoil section, matrix $\left[R_{ad}(r) \right]$ is also a function of this variable. Finally, the transformation from directivity to global is given as

$$\begin{Bmatrix} x_g \\ y_g \\ z_g \end{Bmatrix} = \left[R_{gr}^{yaw} \right] \left[R_{gr}^{tilt} \right] \left[R_{ra}^{azimuth} \right] \left[R_{ra}^{cone} \right] \left[R_{ad}^{pitch+twist}(r) \right] \begin{Bmatrix} x_d \\ y_d \\ z_d \end{Bmatrix} \tag{12}$$

This equation is used to transform the source directivity from the directivity to the global coordinate system.

3.3 Implementation of AeroDyn and FAST

The stand-alone *AeroDyn* and FAST are implemented in the *Aerodynamic Module* to predict the aerodynamic parameters required by WTNoise, i.e. AoA and relative flow velocity. The *Noise Source Module* is modified to account for blade aeroelasticity in the noise prediction and propagation. The standalone *AeroDyn* v15.03 is utilized to calculate aerodynamic parameters for rigid blade cases. FAST is for the flexible blade cases, where the blade deflections affects the noise source placements and orientation. This section explains their implementations and how the blade elasticity affects the noise source directivity (orientation).

3.3.1 Standalone AeroDyn Option

The stand-alone *AeroDyn* essentially is an improved BEM algorithm than the one originally developed in the WTNoise. Its employs the same assumption of rigid turbine blades, but *AeroDyn* has more modeling capabilities (mentioned in Chapter 2.2.2). The WTNoise creates the required files for the stand-alone *AeroDyn*, such as its driver file, primary file, and blade input file. The driver file is responsible for the turbine configurations, initial conditions, and wind conditions. The primary file specifies the BEM modeling options and paths of the airfoil polars and blade input file. Lastly, the blade input file indicates the blade design (chore and structural twist for a particular blade element) along the blade span and the airfoil for each blade element. Once the aerodynamic parameters are computed by the stand-alone *AeroDyn*, the airfoil self-noise is carried out by the *Noise Source Module* and follow the routines shown in Figure 30.

3.3.2 FAST Option

For flexible blade case, FAST computes the aerodynamic parameters and deflections as the blades rotate. The WTNoise creates all the necessary input files for FAST as mentioned in Chapter 2.2.

Although aerodynamic parameters computed by FAST already accounted for the blade deflection, the blade translational and rotational displacements can affect the turbine noise predictions. FAST outputs the translational displacements (x, y, and z-axis of blade coordinates in Figure 12) relative

to the un-deflected blade axis, e.g. blade pitch axis. As mentioned in Chapter 2.3, the *x*-axis displacement is the dominant component while the *y* and *z*-axis displacements are disregarded. As consequences, the *x*-axis displacement (the deflection in the turbine downwind direction) is used to place the noise source at the correct position. More specifically, the noise sources along the blade would be behind the initial positions as the blades deflected in the downwind direction. The new position of the noise source is probably not of significance for the noise at long distances, e.g. > 0.5 km.

For the rotational displacements, only the rotational displacements along the blade y_a-axis is accounted for the noise prediction. The rotational displacement along the y_a-axis can be understood as a local additional blade cone angle due to the blade deflection as illustrated in Figure 18. The effect of the blade deflection angle, $\psi(z)$, is accounted for in the cone rotation matrix, $\left[\hat{R}_{ra}^{cone}(r)\right]$, where the angle $\phi_{cone}(r)$ is the addition of the pre-cone angle and the rotational displacement along the y_a-axis, $\psi(r)$. If to be included, the effect of the airfoil twist due to blade flexibility would be accounted for in the directivity to airfoil rotation matrix, $\left[\hat{R}_{ad}^{pitch+twist}(r)\right]$, in eq.(11) where the angle $\tau(r)$ in the matrix is the addition of the pitch, twist and rotational displacement along the z_a-axis due to blade elasticity, $\hat{\tau}(r)=\theta_T(r)+\theta_P+\theta(r)$. The example case in Chapter 2.3 demonstrates that the rotation along the y_a-axis (the cone angle due to the blade deflection) may have more influence in the noise source directivity than the rotation along the z_a-axis. Specifically, the rotation matrix from the directivity to the WTN global coordinate system is now given as

$$\begin{Bmatrix} x_g \\ y_g \\ z_g \end{Bmatrix} = \left[R_{gr}^{yaw}\right]\left[R_{gr}^{tilt}\right]\left[R_{ra}^{azimuth}\right]\left[\hat{R}_{ra}^{cone}(r)\right]\left[\hat{R}_{ad}^{pitch+twist}(r)\right]\begin{Bmatrix} x_d \\ y_d \\ z_d \end{Bmatrix} \tag{13}$$

where matrices $\left[\hat{R}_{ra}^{cone}(r)\right]$ and $\left[\hat{R}_{ad}^{pitch+twist}(r)\right]$ are changed to account for the blade deformation.

They are now given as follows

$$\left[\hat{R}_{r-a}^{cone}\right]=\begin{bmatrix}\cos(\phi_{cone}+\psi(r)) & 0 & -\sin(\phi_{cone}+\psi(r))\\ 0 & 1 & 0\\ \sin(\phi_{cone}+\psi(r)) & 0 & \cos(\phi_{cone}+\psi(r))\end{bmatrix} \tag{14}$$

where ϕ_{cone} is the initial pre-cone angle and $\phi_{pitch}(r)$ is the rotational displacement along the y_a-axis as a function of blade span, r. Due to the blade flexibility, $\phi_{pitch}(r)$ has different values along the blade span.

$$\left[\hat{R}_{ad}^{pitch+twist}(r)\right]=\begin{bmatrix}\cos\left(\hat{\tau}(r)\right) & \sin\left(\hat{\tau}(r)\right) & 0\\ -\sin\left(\hat{\tau}(r)\right) & \cos\left(\hat{\tau}(r)\right) & 0\\ 0 & 0 & 1\end{bmatrix} \tag{15}$$

where $\hat{\tau}\left(r\right)=\theta_T\left(r\right)+\theta_P+\theta\left(r\right)$.

Thus, modifications are made in the WTN *Noise Source Module* using the above equations to account for blade aeroelasticity in the noise prediction and propagation.

3.4 Noise Propagation

WTNoise has implemented an in-house developed Hamiltonian ray tracing (HRT) propagation method [40]. The inputs to the propagation module are 3-dimensional noise spheres that are created in the *Noise Source Module*. The following sections presents brief information about this noise propagation code. Their details can be found in [40, 60, 61].

3.4.1 Hamiltonian Ray Tracing

The Hamiltonian ray tracing (HRT) propagation method has been implemented in the WTNoise as a noise propagation model based on the work of McBride [40]. The objective is to overcome the setbacks presented by other common approaches and commercial noise code. For example, one of the commercial noise codes, NORD2000, models the wind turbine as a monopole that neglects the actual turbine radiation characteristics. In addition, non-real meteorological conditions

are taken into account. Other assumptions from the common approaches and commercial noise codes include a negligible vertical wind component and absence of spatial speed of sound gradients. These setbacks limit many of the physics needed for accurate noise prediction over long distances. However, HRT is highly capable of handling complicated physical phenomena that leads to high accuracy in the noise propagation. The fundamental of HRT is based on the work of Lighthill [62]. It also address some fundamental issues such as the acoustic wave refraction due to spatial speed of sound gradients, a full Doppler effect formulation resulting from wind velocities in any arbitrary direction, acoustic energy dissipation during propagation, and ground reflections. The HRT that implemented in WTNoise has been validated against other common methods and showed good agreement [40].

The HRT propagation method has two steps. The first one is the computation of the acoustic ray paths that the wind and temperature distributions are accounted for. A set of 3D coupled nonlinear first order differential equations are solved to find the acoustic rays' spatial location and local wave number. In order to propagate a single ray, it initial conditions, initial wavenumber and spatial location, must be known. The initials conditions are the sound sphere computed in the *Noise Source Module*. The final form of the nonlinear set of equations are defined as

$$\begin{aligned}
&\frac{dx}{dt} = c\frac{k_x}{\sqrt{k_x^2+k_y^2+k_z^2}} + V_x \quad \text{and} \quad \frac{dk_x}{dt} = -\sqrt{k_x+k_y+k_z}\frac{\partial c}{\partial x} - k_x\frac{\partial V_x}{\partial x} - k_y\frac{\partial V_y}{\partial y} - k_z\frac{\partial V_z}{\partial z} \\
&\frac{dy}{dt} = c\frac{k_y}{\sqrt{k_x^2+k_y^2+k_z^2}} + V_y \quad \text{and} \quad \frac{dk_y}{dt} = -\sqrt{k_x+k_y+k_z}\frac{\partial c}{\partial y} - k_x\frac{\partial V_x}{\partial x} - k_y\frac{\partial V_y}{\partial y} - k_z\frac{\partial V_z}{\partial z} \\
&\frac{dz}{dt} = c\frac{k_z}{\sqrt{k_x^2+k_y^2+k_z^2}} + V_z \quad \text{and} \quad \frac{dk_z}{dt} = -\sqrt{k_x+k_y+k_z}\frac{\partial c}{\partial z} - k_x\frac{\partial V_x}{\partial x} - k_y\frac{\partial V_y}{\partial y} - k_z\frac{\partial V_z}{\partial z}
\end{aligned} \tag{16}$$

The objective is to solve the spatial components, (x, y, z) that define a single ray's location during propagation, and its corresponding acoustic wavenumber components, (k_x, k_y, k_z). This model accepts all velocity components of the wind (V_x, V_y, and V_z) and variations of speed of sound in any direction. These capabilities lead to high accurate of the ray propagation by supporting 3D wind filed over the desired propagation volume.

The second component of the HRT propagation method corresponds to the characterization of the acoustic wave energy associated to the rays. Tubes that bounded by a bundle of rays are constructed with the energy conservation law applied to them to compute the intensity and sound pressure distributions in the space. However, the cross-sectional area changes depending on the path taken by the bundling rays in each time step during propagation, as well as the intensity. The initial ray tube area and its corresponding initial intensity must be known. In addition, atmospheric attenuation is taken into account of acoustic wave energy calculation. Noise over microphones located on the ground is calculated from ray tubes that have reach the ground. The noise maps then are constructed based on the microphones' data.

For wind turbine noise prediction, the HRT takes the 3D sound sphere that computed at *Noise Source Module* as inputs. The sound sphere contains initial conditions for the HRT ray propagation and acoustic wave energy analysis. Each sphere is constructed by an evenly distributed spherical grid (icosahedron) as Figure 33 shows. Every point over the grid consists of sound pressure level data and initial wavenumber. The initial triangular area with known intensity are defined by the points in the spherical grid. The ray paths propagate according to Equation 93 and tubes consisting of three-ray bundles are constructed. A new area and intensity are calculated for every propagation time-step. Therefore, sound pressure levels can be computed in space for any specified simulation time. In addition, the noise maps around a wind turbine can be constructed by the noise computed from ground reflected bundles of rays. Figure 34 shows the flowchart of using HRT for wind turbine noise predictions.

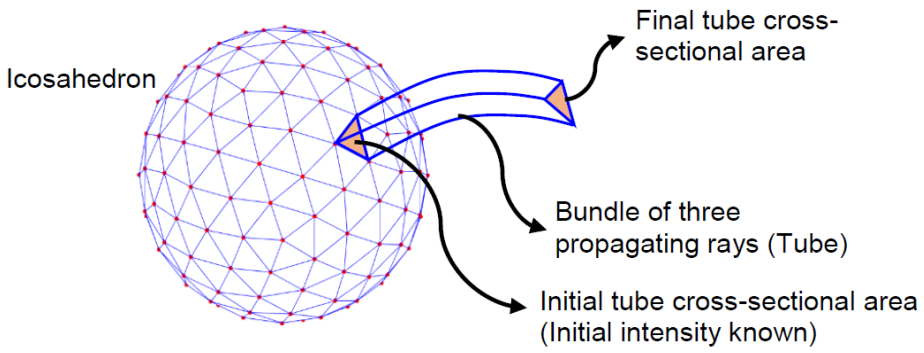

Figure 33: The initial sound sphere that constructed by the spherical grid [40].

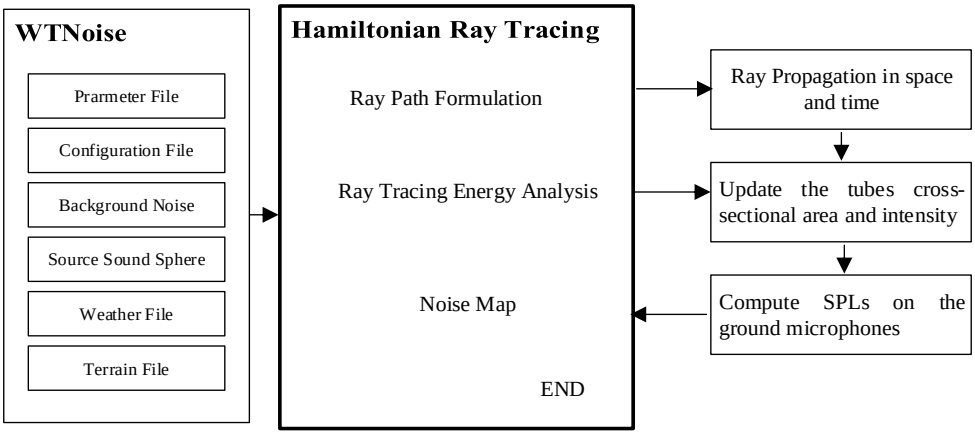

Figure 34: WTNoise and HRT flowchart for the wind turbine noise propagation.

4. Numerical Predictions

This section presents wind turbine noise predictions. To this end, two 3-bladed modern large wind turbines are modeled. They are the NREL 5MW designed by NREL [54] and the Sandia 13.2 MW designed by Sandia National Laboratories [63]. Their blade spans are longer than 50 m to achieve high energy outputs. The NREL 5MW turbine employs a single blade design (referred as NREL-5MW blade). However, the Sandia 13.2MW turbine can accommodate either the SNL100-02 or SNL100-03 blades. In this thesis, only the first two blades are modelled, e.g. NREL 5MW and SNL100-02.

4.1 Wind Turbine Models

This section presents technical information on the two wind turbines used in the simulation as shown in Figure 35. Their rotor sizes are significantly different (126 and 206 m diameters) but the tilt and pre-cone angles are the same. This is due to the fact that Sandia 13.2MW turbine follows the same design principle of the NREL 5MW turbine. The NREL 5MW has been intensively studied in open literature since 2009. The Sandia 13.2 MW is relatively a new developed concept that was published in 2011.

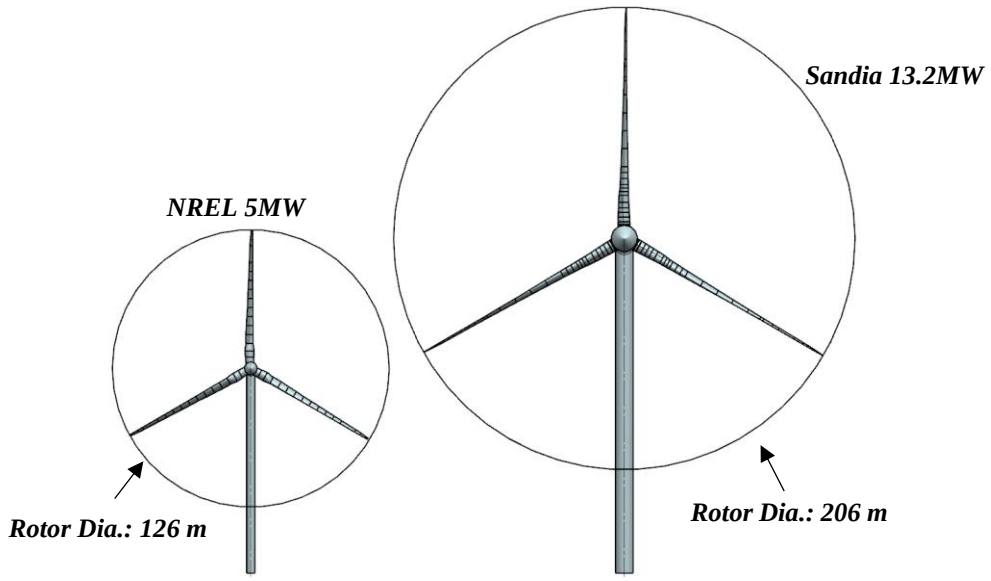

Figure 35: Wind Turbines in this study. Left: NREL 5MW. Right: Sandia 13.2 MW. Note that the hub heights for NREL 5MW and Sandia 13.2MW are 90 m and 146.4 m, respectively.

The three blades, NREL 5MW, SNL100-02, and SNL100-3 are shown in Figure 36. The NREL 5MW blade and SNL100-02 blade both consist of DU and NACA airfoils, but the blade span are 61.5 m and 100 m, respectively. The airfoil distribution along the SNL100-02 blade span is based on the NREL 5MW blade but the chords are scaled-up. However, SNL100-02's structural properties are significantly different due to the blade structure and materials, such the carbon fiber spar, additional shear web, and advanced core materials. The SNL100-03 turbine carried the same blade span and structural design as SNL100-02, but uses flatback airfoils to improve manufacturability and slenderness. ***Since the wind turbine noise code NAFNoise cannot properly handle the flatback airfoil, it is not used in the simulations. However, its properties are still described in here.*** As shown in Figure 36, the SNL100-03 blade is more slender than NREL 5MW and SNL100-02. This leads to dramatic changes in its aeroelastic responses, i.e. the blade deflection is larger than the two other blades. The chord lengths and twist angles along the SNL100-03 blade span are also different from the two other blades.

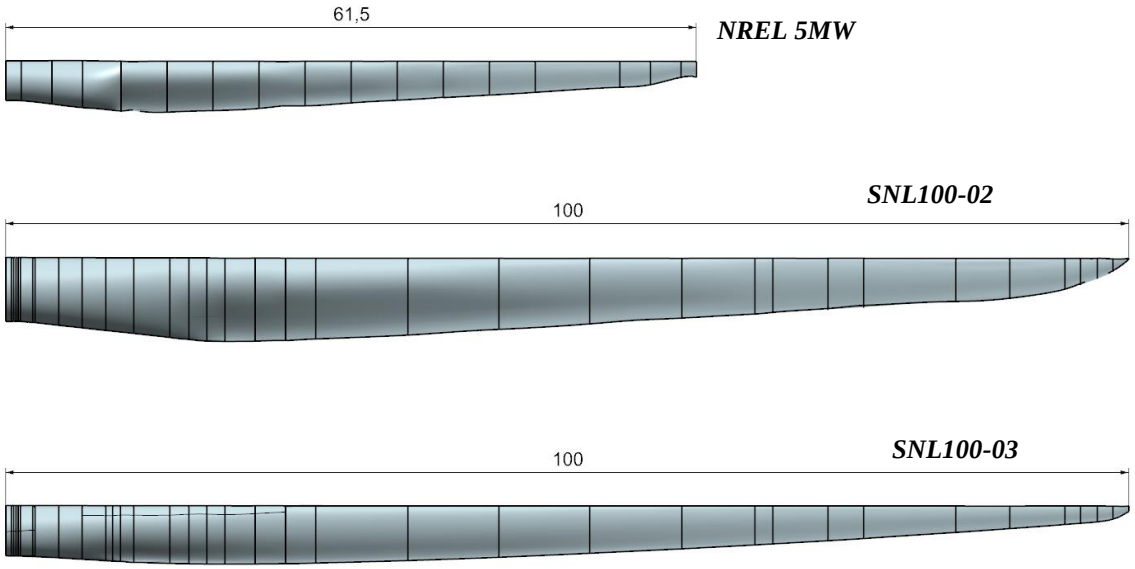

Figure 36: Blade Designs of the NREL 5MW, SNL100-02, and SNL100-03.

The wind turbine models and blades used in this study are available in the public domain, such as the official NREL and Sandia National Laboratories websites. NREL 5MW and Sandia 13.2MW wind turbines are chosen for this thesis because their detailed information and popularity in wind turbine research. Besides the basic wind turbine specification, e.g. rotor diameter, hub diameter and height, rated wind speed, other critical information that is required in this study is also available. The most critical parameters for modeling wind turbine noise are the blade design that contain information about airfoil and sectional properties and the pre-cone and tilt angles.

4.1.1 NREL 5MW wind turbine

The NREL 5-MW is a conventional 3-bladed upwind turbine and has been used extensively by NREL researchers and academics [38, 40, 54]. It has been used as a reference turbine by research teams throughout the world. The design is primarily based on the result of DOWEC project by Hendrick *et.al.*[64]. The goal of DOWEC project was to develop concepts and technology for large wind turbines to be economically feasible. NREL researchers also incorporated designs and test results of two commercial wind turbine, Multibrid M500 and Repower 5M in the NREL 5MW's blade and system design [54]. Thus, the design of NREL 5MW wind turbine consolidated information for academic researchers and turbine manufacturers. Unfortunately, NREL 5MW wind turbine and its blades have not been built yet. Table 7 shows important turbine parameters which will be used in the simulations.

Table 7: The specification of NREL 5-MW.

NREL 5MW Wind Turbine	
Rating	5 MW
Rotor Orientation, Configuration	Upwind, 3 Blades
Rotor Diameter	126 m
Hub Diameter	3 m
Hub Height	90
Rated Wind Speed	11.4 m/s
Rated Rotor Speed	12.1 rpm
Overhang	5 m
Shaft Tilt	-5°
Pre-cone	-2.5°

The NREL 5MW blade has DU family and NACA64 airfoils disturbed along its 61.5 m long blade span. Figure 37a shows the normalized DU family and NACA64 airfoils. These airfoils are

selected based on the research study of DOWEC project [65], and their drag and lift coefficients can be found in [54]. For the aerodynamic analysis, the blade is divided in 19 sections along the span, and each section has an airfoil type, chord length, and structural twist. Figure 37b shows a NREL 5MW blade looking at its pitch axis. The blade starts with airfoils that have cylindrical shapes, DU family airfoils in 16~65%, and NACA in 65~100% of the blade span. The maximum chord length of NREL 5MW blade is 4.65 m at 23% of the span and 1.42 m chord length at the tip. The structural twist of the blade starts with 13.308 ° at the blade root and gradually decreased to zero at the tip. Full table on the blade airfoil and chord properties is listed in Appendix D: The NREL Blade Properties. In addition, the NREL 5MW *AeroDyn* blade input file is constructed based on this information.

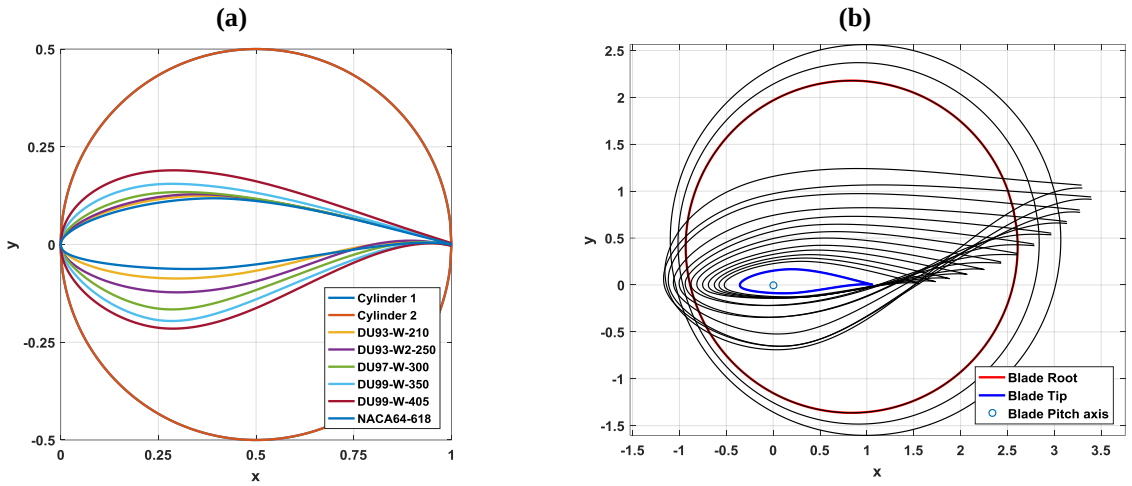

Figure 37: (a) Normalized DU family and NACA64 airfoils **(b)** The NREL 5MW blade in 19 sections looking from the blade pitch axis. Note that the dark lines present the intermediate airfoils.

The NREL 5MW blade structural design carries two shear web design with fiber-glass composite laminates on its panel (with foam core materials), spar cap, leading-edge (LE), and trailing-edge (TE) reinforcement. In other words, it employs the conventional architecture and fiberglass-only composite material. Figure 38 shows an illustration of a two shear web blade structure. The purpose of shear web is not only to create the blade geometry, but also prevent buckling from its weight or operational loads. Shear webs essentially turn a pair of spar caps into an I-beam that strength the blade structure and prevent failures from the surface layers. The LE and TE reinforcement are employed for the blade design to meet the fatigue requirements. It is important to mention that the NREL 5MW blade structural design was not fully defined in the original report

by Jonkman [54], i.e. only the sectional structural properties were given. The above information is based on work of Resor [66], who reversed engineered the NREL blade structural design from information given by NREL and DOWEC project.

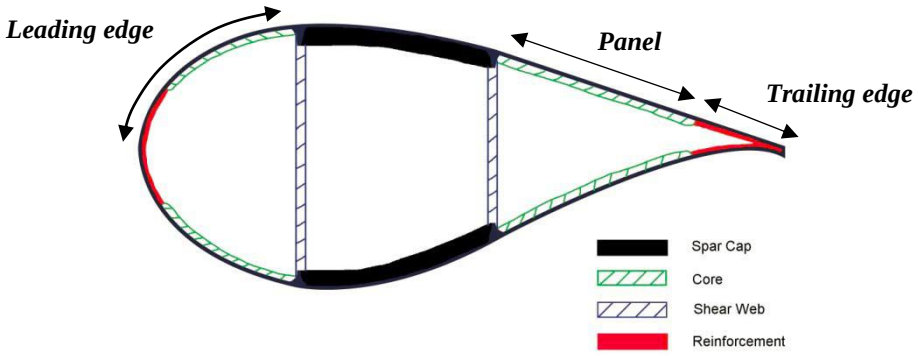

Figure 38: Illustration of the NREL 5MW blade cross-section with two shear webs [67].

Jonkman *et.al* conducted a series of study on the NREL 5MW blade deflection in the steady-state condition. The simulations were carried out by FAST v7.0 and the simulation time was long enough to ensure that all transient behavior had died out. It is important to mention that FAST v7.0 employed a simpler blade dynamic model that yields lower fidelity than FAST v8.0 (which is the simulation tool for this thesis). Figure 39 shows the blade 1 tip deflection, *OoPDefl1*, as a function of the wind speed in uniform flow. *OoPDefl1* represents the out-of-plane tip deflection, i.e. in downwind direction of the rotor, of blade 1 relative to the un-deflected blade-pitch axis. The tip deflection at its rated wind speed, 11.4 m/s, was around 5.5 m. Note that the phenomenon of the blade deflection gradually decreasing with higher wind speeds was due to the blade-pitch actuator. The wind turbine controller changed the blade pitch angle to prevent the large blade deflection that may leads to the blade structural failure. ***In this thesis, the wind turbine control feature is disabled to focus on the effects of blade deflection on wind turbine noise predictions at the turbine rated speed.*** Resor also performed a FAST v7.0 simulation in different operational scenarios [66]. The maximum deflection in the out-of-plane direction was 6.03 m (allowable 7.07m) under extreme coherent gust with change in direction (ECD-R in IEC 61400-1 standards). In ECD-R, a rise in wind speed is assumed to occur simultaneously with a direction change up to 64 degree over six seconds. Detailed are provided in the IEC 61400-1 standards [68].

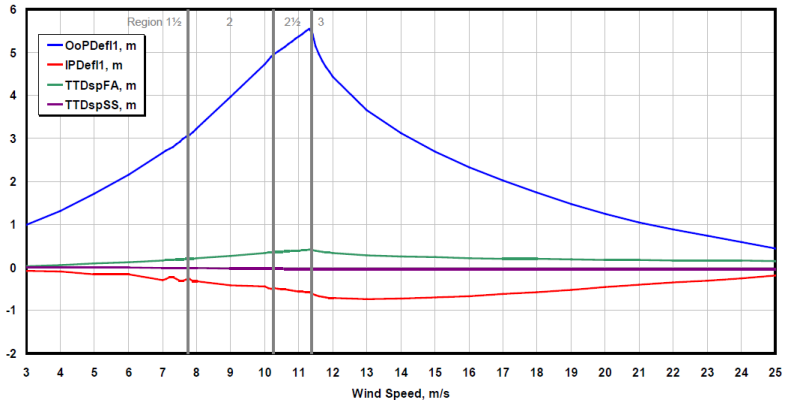

Figure 39: NREL 5MW blade deflection (downwind) *vs.* wind speeds in the steady-state condition [54].

The blade models used by Jonkman and Resor were based on the blade sectional properties provided in [54], which are listed in Appendix D: The NREL Blade Properties. The *BeamDyn* blade input file is also created based on this information. The mass and stiffness matrices of the blade are constructed using Equation 49 and 50. It is important to mention that the flap and edge shear stiffness properties are not defined in [54]. Qi Wang, the lead developer of *BeamDyn*, who provided NREL 5MW blade model, defined these two properties one order of magnitude less than extension stiffness, $K_{ShrFlp} = K_{ShrEdg} = EA/10$, to prevent numerical errors [50]. This approach has yields good agreements in the blade dynamic responses with other blade models in [50, 52, 53]. Therefore, the NREL 5MW *BeamDyn* blade model and other blade models follow the same practice. For the blade aeroelastic analysis in this thesis, a NREL 5MW blade is modeled as one single element with 7 FE nodes (6^{th}-order of the shape function) and 49 stations (49 sectional properties).

The natural frequencies of the blade are critical as the severe vibration would cause damage, malfunction, or mechanical failures of the turbine. Lloyd has suggested that at least the first natural frequency of a rotor blade shall be determined in the flapwise and edgewise directions for turbine certifications [69]. A turbine blade is typically modeled as a cantilevered beam, which the modes are analyzed by FEA. Resor has presented the first 6 mode of a stationary NREL 5MW blade using ANSYS as listed in Table 8 [66]. To benchmark these values, *BModes*, a finite-element code that provides modes for a beam by NREL [70], is used. As shown in Table 8, the results show good agreements with around 5% errors. The natural frequencies of the rotating blade is also predicted at the rated speed, 12.1 rpm. The rotating blade experiences a centrifugal force and a stiffening

effect of the blade and increases the natural frequency compared with the static value [71]. These mode shapes are illustrated by Kim using a laser Doppler vibrometer as shown in Figure 40 [72]. Although the blade is a 1/23 scale of the 750 kW composite turbine blade, the normalized mode shape still gives an insight of how the NREL 5MW blade deflected due to the natural frequencies.

Table 8: NREL 5MW blade modal frequencies and shapes.

	By Resor, 2013	***By BModes***	***By BModes, rotating***	
Mode #	***Frequency , HZ***	***Frequency , HZ***	***Frequency , HZ***	***Description***
1	0.870	0.824	0.853	1st flapwise mode
2	1.06	0.941	0.976	1st edgewise mode
3	2.68	2.42	2.46	2nd flapwise mode
4	3.91	2.90	2.94	2nd edgewise mode
5	5.57	5.14	5.15	3rd flapwise mode
6	6.45	6.37	6.41	1st twist mode
7	*N.A*	7.72	7.76	flapwise-twist mixed mode
8	*N.A*	9.98	9.91	5th flapwise mode
9	*N.A*	11.0	11.1	3rd edgewise mode
10	*N.A*	13.9	14.0	*Not clear*

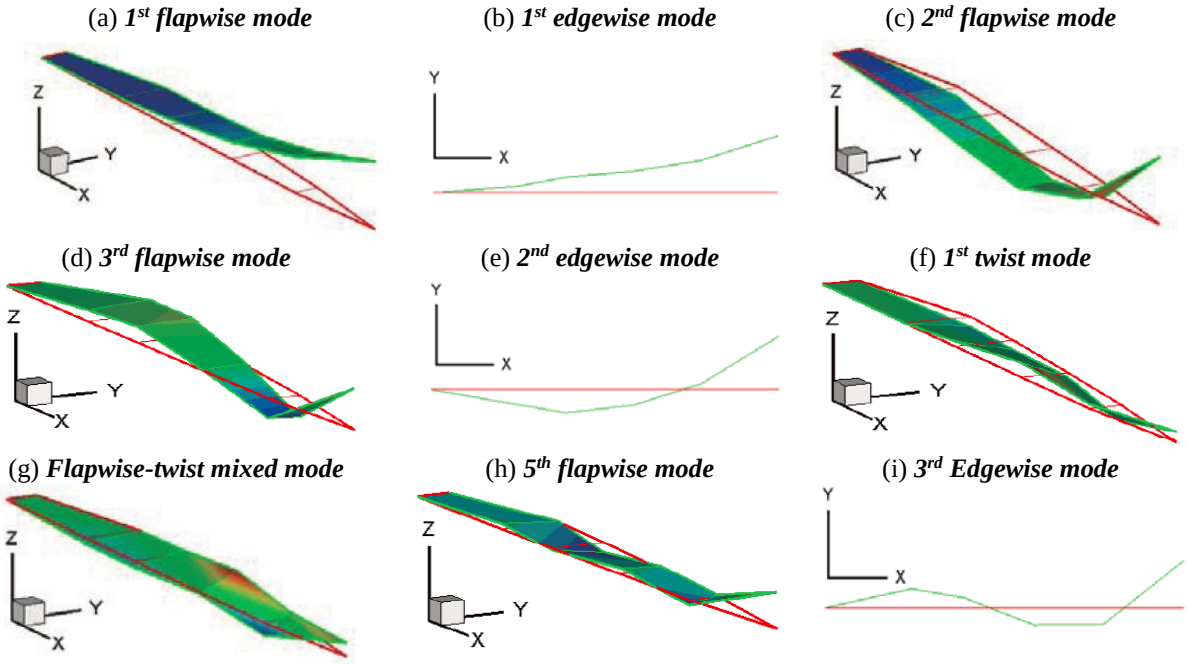

Figure 40: The normalized mode shapes of a wind turbine blade by Kim [72].

The structural damping coefficients play important roles in the blade deflections. The reference NREL 5MW blade model has the damping coefficients equal to 0.001. ***The damping coefficients are given by Wang, who performed BeamDyn validation on the NREL 5MW blade in [52].***

Unfortunately, the reasons for $\mu = 0.001$ was not explained, and the specific values are not defined in the NREL 5MW documents [54, 66]. Figure 41a shows how the blade tip deflection fluctuates with different damping coefficients as a function of time. The wind condition is uniform wind with speed of 10 m/s. The steady-state blade tip displacement with respect to the blade azimuth position is plotted in Figure 41b. For the $\mu \leq 1$ cases, the values are very close to each other's and the fluctuations are around 0.3 m. For the $\mu > 1$ cases, the fluctuations are about 0.05 m. The blade tip deflection fluctuation also influences the aerodynamic parameters as shown in Figure 42. The blade tip AoA fluctuates more than 1.5° for the cases of $\mu < 1$ and around 0.8° for the $\mu > 1$ cases. ***Therefore, the structural damping coefficients for all the blades in this thesis are assumed to be*** $\mu = 1$.

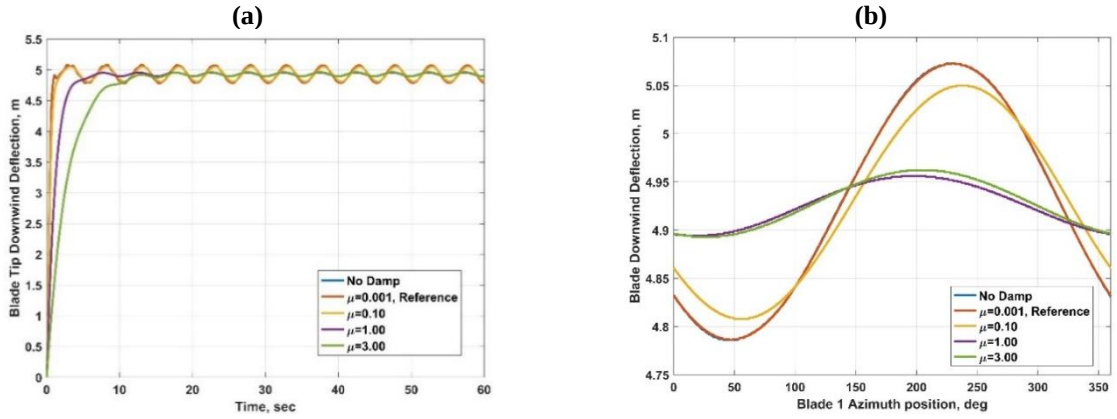

Figure 41: NREL 5MW blade tip deflections with different structural damping coefficients under a 10 m/s uniform wind. **(a)** The full time history plot and **(b)** steady-state blade deflection *vs.* the blade azimuth position.

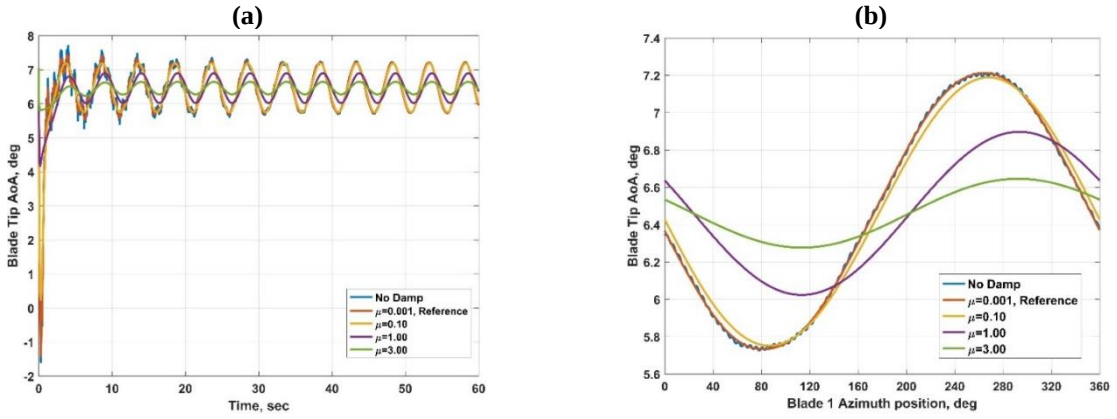

Figure 42: The blade tip AoA with different structural damping coefficients under a 10 m/s uniform wind. **(a)** The full time history plot and **(b)** the steady-state AoA *vs.* the blade azimuth position.

4.1.2 Sandia 13.2MW, SNL100-02 Blade

The Sandia 13.2 MW wind turbine is part of ongoing research and development efforts to create and evaluate modern large wind turbine designs that are more efficient aerodynamically, structurally, and economically. Griffith from Sandia National Laboratories presented a 13.2 MW horizontal axis wind turbine that employed 100 m long blades, which are significantly longer than the largest commercial blades at 2012 [73]. Details on the Sandia 13.2 MW design can be found in [63]. The important specification of the Sandia 13.2 MW turbine is listed in Table 9. It employed the same airfoils and blade structures as the NREL 5MW blade. However, the original SNL100-00 blade encountered many issues, such as buckling and unrealistic heavy weight. The structural modifications were implemented to address these issues in the SNL100-02 blade. ***Therefore, the SNL100-02 has the same geometry as the NREL 5MW blade, but structurally different.*** Unfortunately, the Sandia 13.2MW wind turbine and SNL100-02 blade have not been built yet. The details on the SNL100-02 blade can be found in [74].

Table 9: The specification of Sandia 13.2-MW.

Sandia 13.2-MW Baseline Wind Turbine	
Rating	13.2 MW
Rotor Orientation, Configuration	Upwind, 3 Blades
Rotor Diameter	205 m
Hub Diameter	5 m
Hub Height	146.4
Rated Wind Speed	11.3 m/s
Rated Rotor Speed	7.44 rpm
Overhang	8.16 m
Shaft Tilt	-5°
Pre-cone	-2.5°

The airfoils are distributed along its 100 m long blade span and are scaled-up based on the NREL 5MW blade. For the aerodynamic analysis, the SNL100-02 blade is divided into 20 sections along the span, and each section corresponds with its airfoil type, chord length, and structural twist. Although the number of the sections is different than the NREL 5MW blade, these parameters are identical except for the chord length. The maximum chord length of SNL100-02 is 7.65 m at 19.5% of the span and 1.15 m chord length at the tip. The blade uses cylindrical airfoils in 0~18%, DU family airfoils in 19~60%, and NACA64 in 67~100% of the blade span. The structural twist of the blade starts with 13.308 ° at the blade root and gradually decreased to zero at the tip. Full table on

the blade airfoil and chord properties is listed in Appendix E: The SNL100-02 Blade Properties. In addition, the SNL100-02 *AeroDyn* blade input file is constructed based on this information.

The SNL100-02 blade employs the three shear webs design that starts from the blade span 14.6 m to 60.2 m. An example is shown in Figure 43 at the blade span 19.5 m with the maximum chord 7.65 m. The SNL100-02 is no longer all-fiberglass materials like the NREL 5MW blade. Carbon fiber materials are utilized in the entire SNL100-02 spar cap. The spar cap's thickness and width are re-sized for weight reduction. In addition, the thickness of TE reinforcement and foam core in the shear web and panel laminates are optimized for the weight reduction. The fiberglass foam material is also replaced with advanced core materials, balsa and PET foam. The balsa is used in critical buckling areas (inboard in the tailing edge panels and along the trailing edge reinforcement) and PET foam is used in the less critical bucking area (in the shear webs, leading edge panel, and outboard in the trailing panel). The weight of SNL100-02 was reduced from 114 tons (SNL100-00) to 59 tons. This weight reduction leads the blade design to be more practical and the Sandia 13.2MW more structurally and economically feasible.

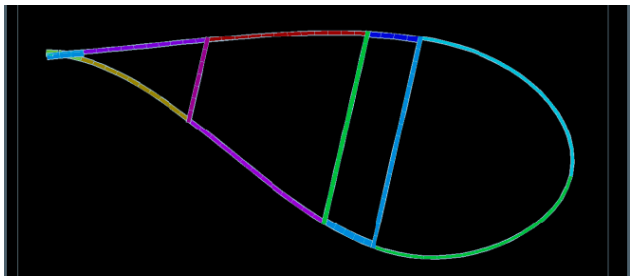

Figure 43: SNL100-02 cross-sectional plot at the blade span 19.5 m [74].

Griffith *et.al* conducted a series of study on the aeroelastic responses of the SNL100-02 in various operational scenarios according to the IEC 61400-1 blade design criteria [74]. The simulations were carried out by FAST v7.0. The result showed the maximum blade deflection is 10.51 m under ECD-R wind condition. For the aeroelastic analysis, the SNL100-02 *BeamDyn* blade is modeled as one single element with 7 FE nodes (6^{th}-order of the shape function) and 34 stations. Full table on the blade structural properties is listed in Appendix E: The SNL100-02 Blade Properties.

The first natural frequency of SNL100-02 has been reported by Griffith using ANSYS[74]. BModes is again utilized to compute other modal frequencies and shapes and a good agreement is shown as listed in Table 10.

Table 10: SNL100-02 modal frequency and shapes.

	By Griffith, 2013	***By BModes***	***By BModes, rotating***	
Mode #	***Frequency , HZ***	***Frequency , HZ***	***Frequency , HZ***	***Description***
1	0.55	0.583	0.604	1st flapwise mode
2	*N.A*	0.723	0.729	1st edgewise mode
3	*N.A*	1.75	1.77	2nd flapwise mode
4	*N.A*	2.58	2.59	2nd edgewise mode
5	*N.A*	3.73	3.75	3rd flapwise mode
6	*N.A*	4.02	4.02	1st twist mode
7	*N.A*	5.98	5.99	flapwise-twist mixed mode
8	*N.A*	6.55	6.58	5th flapwise mode
9	*N.A*	7.69	10.2	3rd edgewise mode

4.1.3 Sandia 13.2MW, SNL100-03 Blade

SNL100-03 blade is the most updated blade design for the Sandia 13.2MW wind turbine [2]. It is also the successor design of SNL100-02, i.e. SNL100-03 employs all the positive design features from SNL100-02, such as advanced core materials, carbon fiber spar caps, and optimized thickness of the blade structure. The motivation of SNL100-03 is to achieve further weight reduction for the blade design to be cost-effective. The design also demonstrates the effect of a new blade geometry using flatback airfoils shown in Figure 44 versus conventional sharp trailing edge airfoils as the SNL100-02. The flatback airfoils are based on the work of Berry in the Sandia BSDS (Blade System Design Study) blade [75]. In addition, the effect of varying blade slenderness is also demonstrated in SNL100-03. The final design has significantly reduced blade chord, resulting in the weight deduction from to 59 tons to 49 tons.

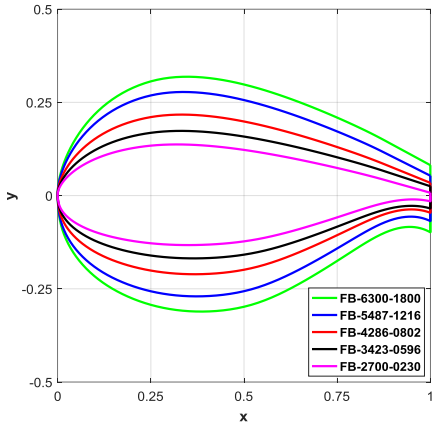

Figure 44: Normalized flatback airfoils in SNL100-03 blade.

The SNL100-03 flatback airfoils have different aerodynamic performance than the DU family airfoils used in the SNL100-02. Figure 45 shows the drag and life coefficients as a function of AoA for FB-4286 and DU-405 airfoils. The plots indicate that FB-4286 has higher aerodynamic coefficients than the DU-405 airfoil employed by SNL100-02. Although the flatback airfoils have better performance than DU airfoils, the aerodynamic performance for the entire blade is slightly less than the SNL100-02.

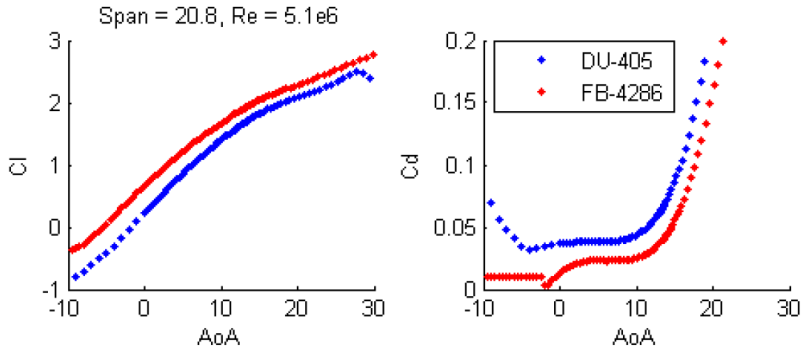

Figure 45: Airfoil polars for DU-405 (in SNL100-02) and FB-4286 (in SNL100-03) [76].

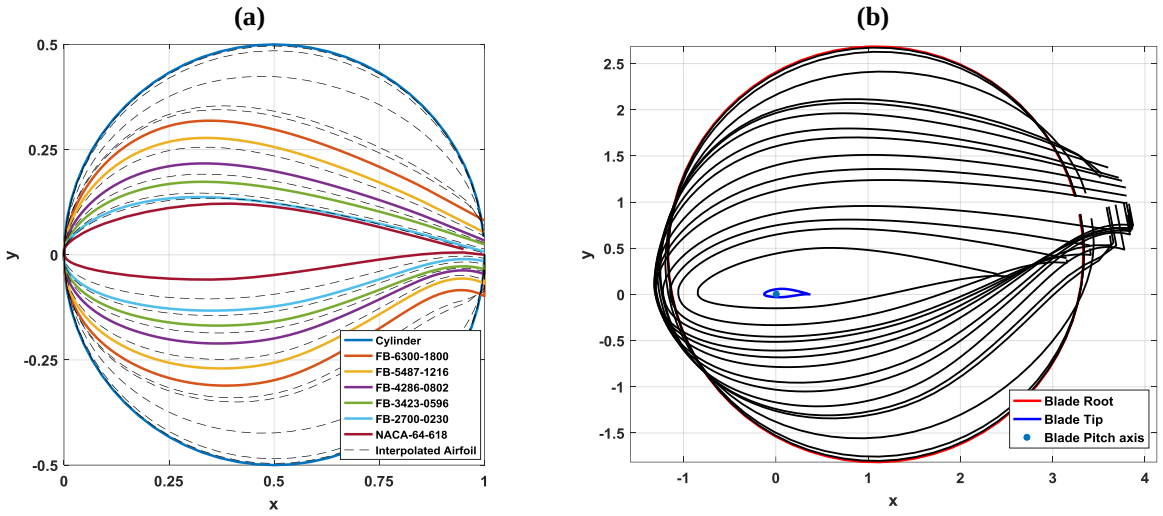

Figure 46: (a) Normalized flatback airfoils and NACA64 airfoil **(b)** SNL100-03 in 18 sections looking from the blade pitch axis. Note that the dark line present the intermediate airfoils.

4.2 Weather and terrain Properties

The weather conditions consist of the non-uniform wind and temperature profiles shown in Figure 47. They were generated by modifying experimentally measured data [77]. There is no vertical wind component in the simulation. The terrain was assumed flat and acoustically hard, e.g. very high uniform flow resistivity.

In the FAST simulations, the non-uniform wind profile shown in Figure 47a is approximated using a power-law function with shear exponent $\alpha = 0.2$ with wind speed 10 m/s at the height of 100m. Uniform wind profiles with the temperature and wind speed at the NREL 5MW and the Sandia 13.2MW hub heights will be used for comparisons, i.e. 10m/s and 16 °C for the NREL 5MW and 14m/s and 15 °C for the Sandia 13.2MW. The wind and temperature profile shown in Figure 47 are also used in the noise propagation model. In Figure 47a, the rotor sizes and hub heights of the two wind turbines are illustrated as the black lines and red dot, respectively.

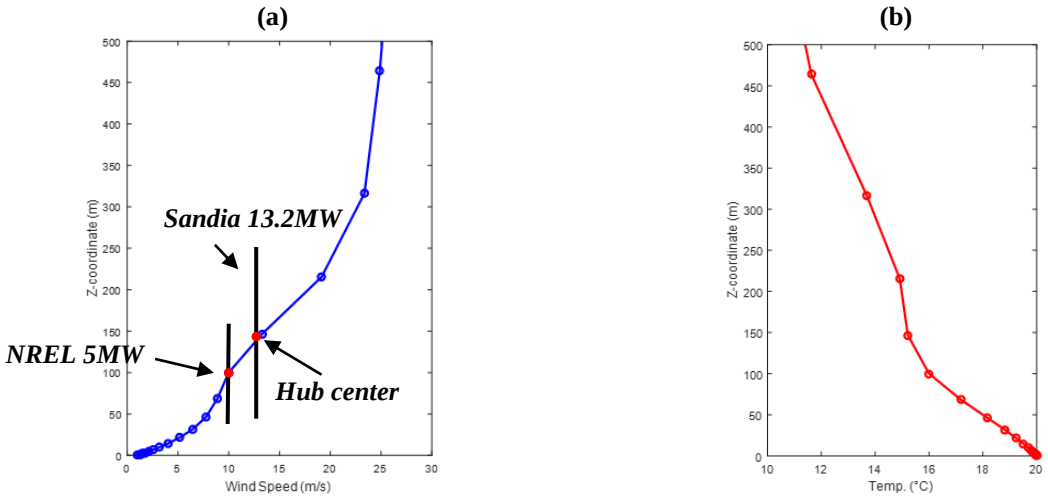

Figure 47: (a) Wind and **(b)** temperature profiles used from experimentally measured data by Slawsky [77].

4.3 Simulation Results

This section presents the simulation results of the wind turbines described in section 4.1. Figure 48a and Figure 48b show isometric views of the NREL 5MW and the Sandia 13.2 MW turbines to demonstrate their size differences. Figure 48c and Figure 48d show side views of the turbines illustrating the cone and tilt angles. The wind turbines are simulated under their rated conditions, e.g. low inflow wind speed and nominal rotor speed (10 rpm for the NREL 5MW and 7 rpm from the Sandia 13.2MW). Flow separation or stall on airfoils is absence due to the low AoAs resulting at these conditions.

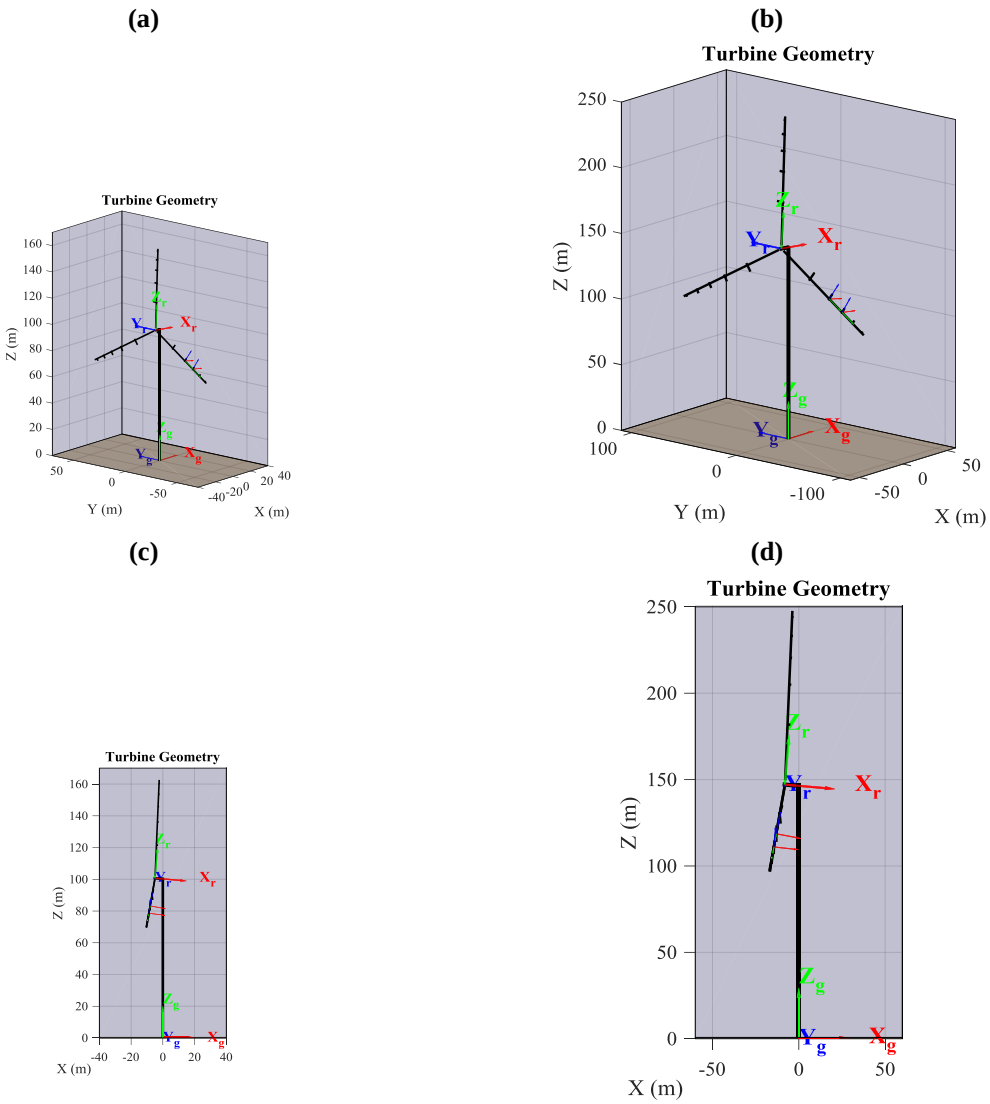

Figure 48: An isometric view of **(a)** a NREL 5MW turbine and **(b)** Sandia 13.2 MW turbine in the WTNoise global coordinates. A side view of **(c)** a NREL 5MW turbine and **(d)** a Sandia 13.2 MW turbine that have tilt and pre-cone angles.

The noise results are computed over a domain 2 km by 2 km by 0.5 km as shown in Figure 49a. The turbine is placed at the center of the domain, i.e. (0,0,0) in the global coordinate system. Although noise is computed over the whole domain, this thesis focuses on the average overall A-weighted noise level (OASPL) prediction on the ground, e.g. the wind turbine noise map as shown in Figure 31f. To this end, an array of 1600 microphones is distributed over a uniform square grid with a 50 m resolution as shown in Figure 49b. All the noise calculations are performed in 1/3rd octave bands. In addition to the noise map, the 1/3rd octave band noise spectrum at selected microphones downwind from the turbine are also investigated. These microphones are located at

$H + D/2$ m (H is the tower height and D is the rotor diameter) according to the IEC 61400 standard and 500 m, which is the typical distance from residents to a turbine.

For the acoustic simulations, the blades were divided in 5 span-wise elements (illustrated in Figure 31d) and rotation accounted for by taking 15 azimuth position for a total of 75 sound source distributed on the rotor plane as shown in Figure 50. *NAFNoise* is used to predict the TBL-TE (pressure side and suction side), SF, and LBL-VS noise components for the 75 sound sources. The TEB-VS is not modeled since modern wind turbine blades have sharp trailing edge designs, so that this noise source is insignificant. The TI noise is not modeled due to absence of turbulences in these simulations. In all the acoustic simulations, there are 10,242 rays emitted per sound source, resulting a total of 768,150 rays emitted from the wind turbine.

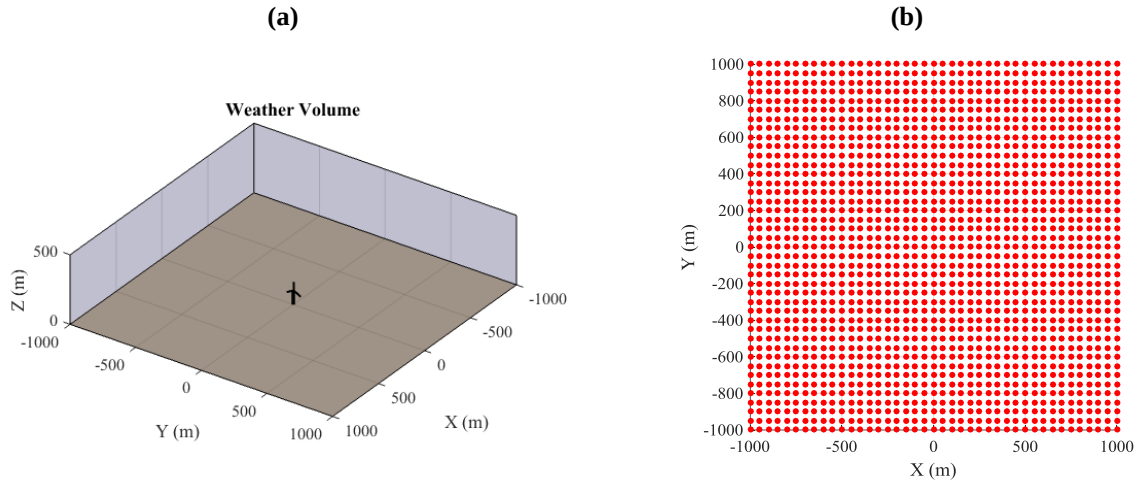

Figure 49: (a) The acoustic simulation domain is a 2 km by 2 km by 0.5 km rectangular cube. **(b)** The microphone grid over the domain. Each dot represents a microphone on the ground uniformly distributed 50 m apart.

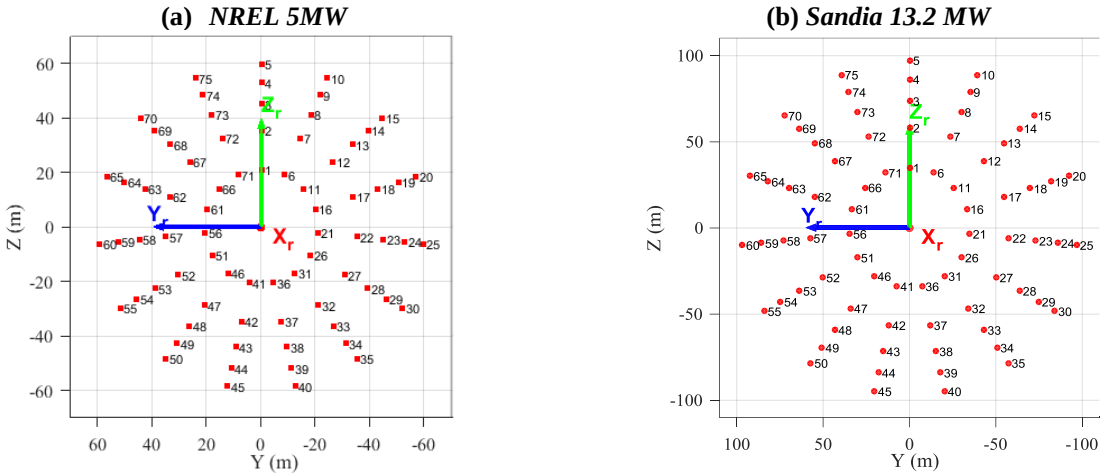

Figure 50: Point sources on **(a)** the NREL 5MW and **(b)** Sandia 13.2 MW rotor planes to compute data for the aerodynamic and noise calculations.

A number of simulations are performed to assess the effects of turbine parameters and blade aeroelasticity as shown in Table 11. The case 0 is referred as the baseline.

Table 11: Noise simulation cases in this thesis.

Case	*Turbine*	*Blade*	*Wind Condition*	*Wind Angle*	*Yaw*	*Tilt*	*Cone*
0	NREL	Rigid	Uniform, 10 m/s	0	0	0	0
1	NREL	Rigid	Non-uniform	0	0	0	0
2	NREL	Rigid	Non-uniform	0	0	5	2.5
3	NREL	Rigid	Non-uniform	0	20	5	2.5
4	NREL	Rigid	Non-uniform	20	0	5	2.5
5	NREL	Flexible	Non-uniform	0	0	5	2.5
6	Sandia	Rigid	Uniform, 14 m/s	0	0	5	2.5
7	Sandia	Rigid	Non-uniform	0	0	5	2.5
8	Sandia	Flexible	Uniform, 14 m/s	0	0	5	2.5
9	Sandia	Flexible	Non-uniform	0	0	5	2.5

4.3.1 Results for Case 0

This case (the NREL 5MW turbine with no cone and tilt) is not realistic due to the uniform wind and absence of temperature gradient. However, it serves the main purpose of illustrating the effect of the weather condition on the noise propagation. The main interest in the aerodynamic result is

the AoA since it is a critical parameter for the noise prediction. Figure 51 shows the AoA distribution on the rotor plane from 30% to 100% of the blade span. The AoA for the blade span less than 30% (cylindrical airfoils) is not shown due to their insignificant noise contribution. As expected, the AoA is axisymmetric and changes radially. The maximum AoA (~6º) occurs close to the blade root and the minimum occurs in the mid region. However, in the most important outer section of the blade the AoA is around ~ 4º.

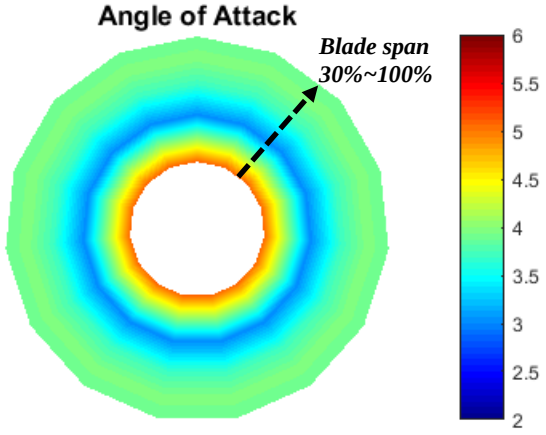

Figure 51: The AoA distribution over NREL 5MW rotor plane for case 0.

Figure 52 shows A-weighed noise spectrums for sources 1 and 5 (see Figure 50a for the locations). The SPLs are computed at 1 m away from the airfoil trailing edge normal to the chord. The TBL-TE (pressure side and suction side) and TBL-TE Sep (turbulent boundary layer separation) components are shown in Figure 52b. The spectrum changes radially along the blade from these two locations because the airfoil, AoA, and relative inflow speed are different along the blade span. The airfoil type changes according to the blade design and the AoA tends to increase towards the blade tip. The relative inflow speed gradually increases from the blade root to tip, resulting in higher SPL at the blade tip, e.g. source 5. In additional, the SPL peak frequency ranges from 100 Hz to 500 Hz with the blade span, *r*, primarily due to the chord length.

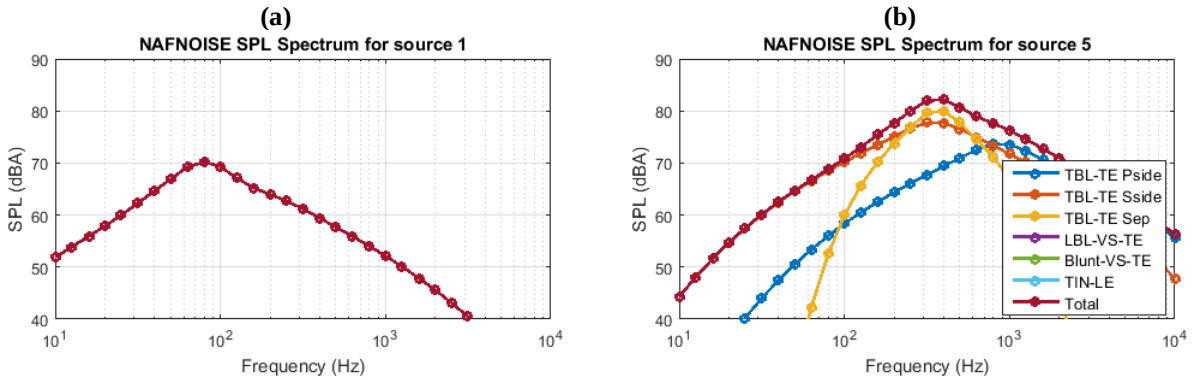

Figure 52: The SPL spectrum of NREL 5MW wind turbine at **(a)** source 1 and **(b)** 5. Note that TEB-VS (indicated as Blunt-VS-TE) and TI (indicated as TIN-LE) noise components are not modeled.

The spectrum for all 75 sources are used to plot the overall A-weighted sound power level distribution over the rotor plane to give an insight of how the turbine radiates sound as shown in Figure 53. The plot shows a radial increase in the noise level over the rotor plane. The overall A-weighted sound power level distribution has the maximum value at the blade tip at 96.8 dBA and the minimum at the 30% blade span at 74.6 dBA.

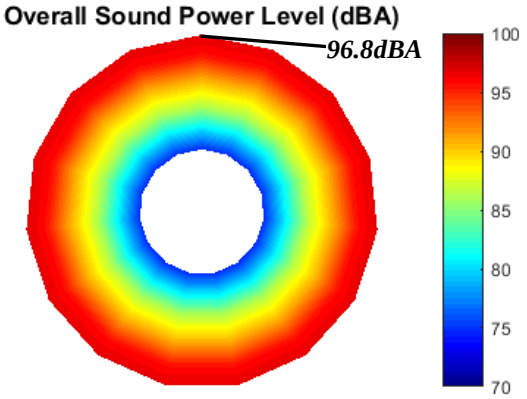

Figure 53: Overall A-weighted sound power level distribution over the NREL 5MW rotor for case 0.

Figure 54 shows the noise sources associated to a rotor position. The plot not only shows the directivity of the noise sources at 500 Hz, but also demonstrates that the noise is radiated mostly in the upwind and downwind directions. Figure 55a shows a side view of the rotor. Notice that for every sound sphere, the SPL is higher in the upwind and downwind directions due to the directivity. Figure 55b provides a better view on how the turbine radiates noise and the directivities of each sound sphere. Figure 55c shows the directivity of source 5 close to the blade tip. It gives more details on how the sound sphere radiates noise.

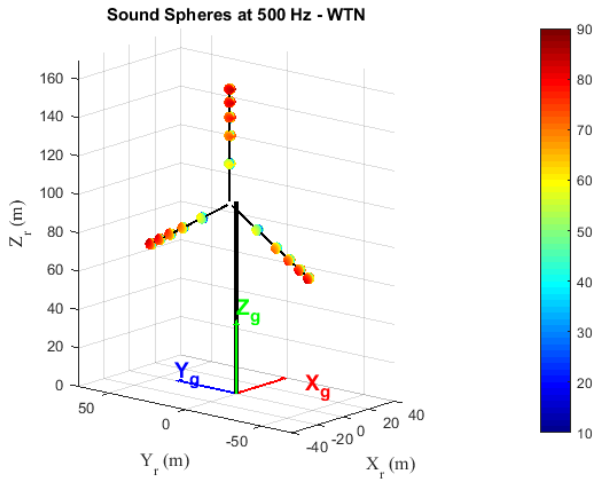

Figure 54: The sound sphere directivity at 500 Hz for the NREL 5MW wind turbine.

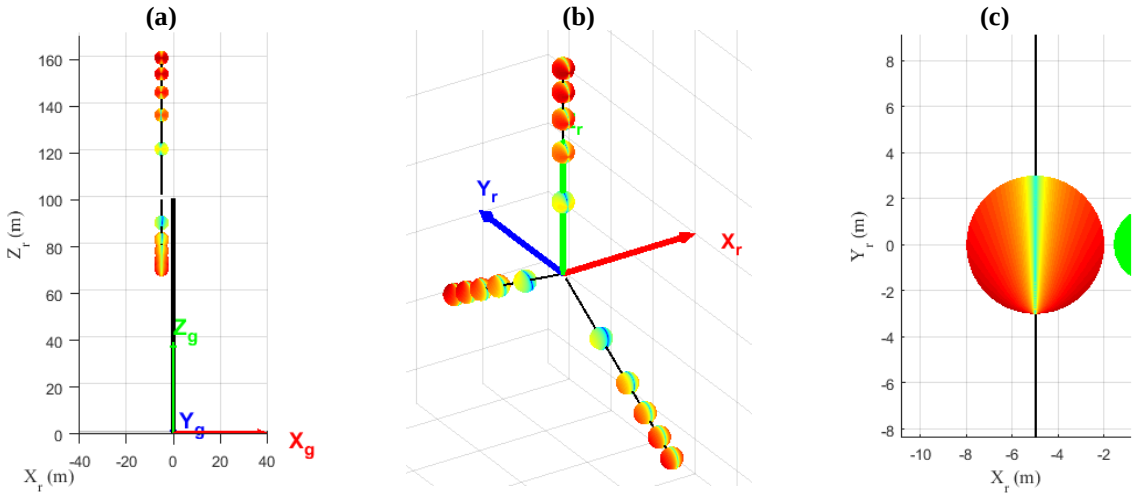

Figure 55: A NREL 5MW turbine and the sound spheres associate with the blades. **(a)** The side view, **(b)** isometric view of the rotor, and **(c)** detailed view of one of the sound spheres near the blade tip.

The noise map is shown in Figure 56. The plot shows that the noise predominately propagates in up and downwind direction, consistent with the sound sphere directivity shown in Figure 55b. The turbine noise propagates nearly the same in the upwind or downwind directions since the uniform wind do not bend the acoustic rays. The SPL spectrums of the two selected downwind microphones are shown in Figure 57. The microphone 4 is located 150 m away from the turbine, which predicts the noise according to the IEC 61400-11 (100 m tower height + 106/2 m rotor radius). The microphone 11 is located 500 m away from the turbine. The maximum SPL from the microphone 4 and 11 are 47.9 dBA and 39.2 dBA, respectively. As expected, the SPL decreased as the microphones are farther away from the turbine.

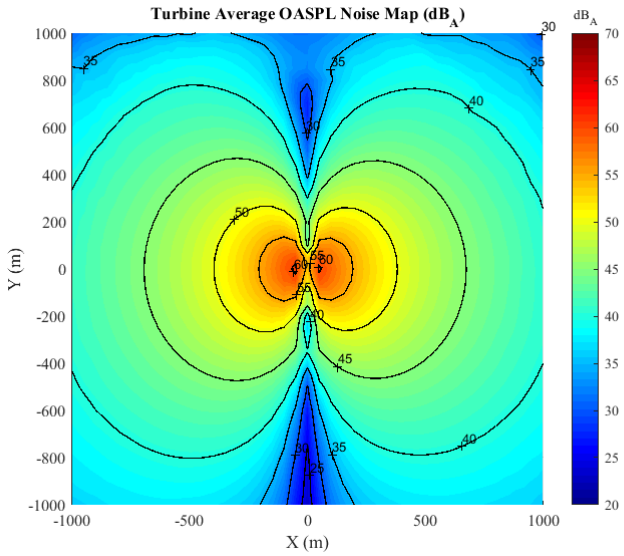

Figure 56: The NREL 5MW turbine OASPL noise map for case 0.

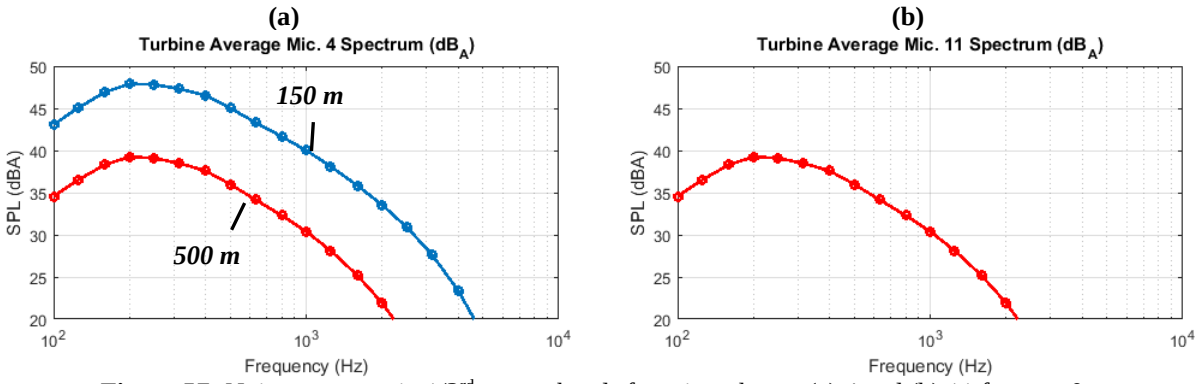

Figure 57: Noise spectrum in 1/3rd octave bands for microphones (a) 4 and (b) 11 for case 0.

4.3.2 Results for Case 1

This case allows to access the effect of non-uniform wind condition. In this non-uniform wind case, the rotor experience wind speed of 11 m/s and 8.2 m/s at top and bottom of the rotor, respectively. This wind profile affects the turbine aerodynamics, e.g. AoA, which also affects the radiated noise.

The AoA distribution over the rotor plane is plotted in Figure 58a. The AoA is no longer axisymmetric on the rotor plane like case 0 (Figure 51). Instead, it has higher AoA at the rotor top due to the higher wind speed (11m/s) compared to the bottom (8.2 m/s). Figure 58b is the overall sound power level distribution over the rotor. Although the difference is not obvious, it has the same trend as the AoA distribution, i.e. the levels are higher at the rotor top position.

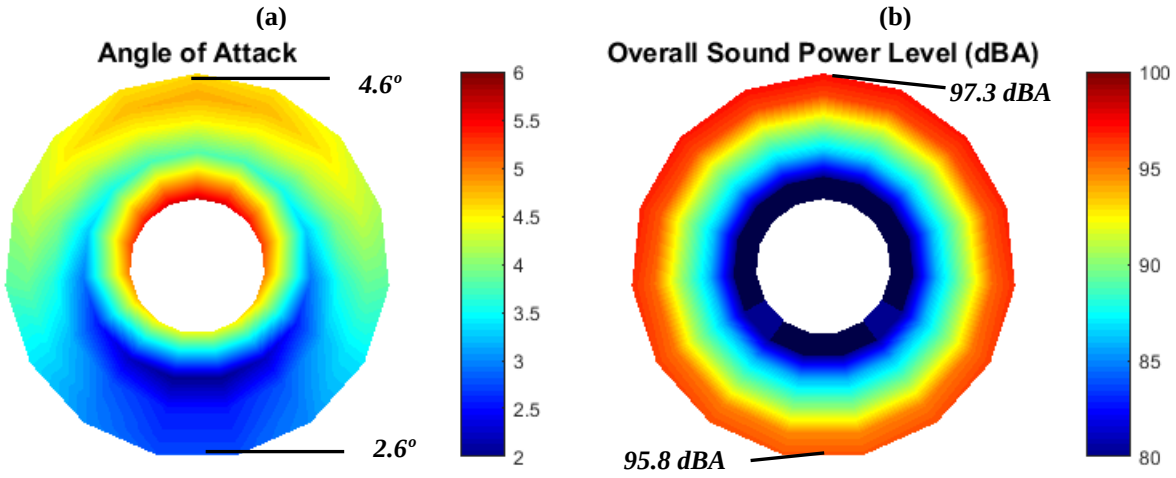

Figure 58: (a) AoA and **(b)** source overall sound power level distributions over the rotor for case 1, NREL 5MW turbine with rigid blades**.**

The non-uniform wind condition has a dramatic effect on the noise propagation. To better illustrate this fact, Figure 59 shows the noise map for cases 0 (same as Figure 56) and 1 side-by-side. For case 0 (uniform wind), all straight rays pointing towards the ground emitted from the turbine will eventually arrive to the ground. However, in the presence of a non-uniform wind and temperature profiles as is case 1, some rays are bent upward in the upwind direction and never reach the ground. The region where sound is not reaching the ground is known as the shadow zone. Similarly, in the downwind direction the acoustic rays are bent down and results in an increase in noise. Another feature in the noise map for case 1 with non-uniform wind is the lack of symmetry in the results with respect to the *y*-*z* plane. The noise levels are higher towards the port side.

The SPL spectrum for microphones 4 and 11 are shown in Figure 60. At microphone 4 location, the non-uniform wind case has lower SPL compared to case 0 (around 1.0 dBA across the frequency range). This reduction in levels is probably due to the lower noise emission when the blade is in the bottom position when is the closest to microphone 4. Though the blade in the top position radiates more noise, it is further away from the microphone and thus it has less of an effect. The difference between the two cases is much smaller for microphone 11 at 500 m.

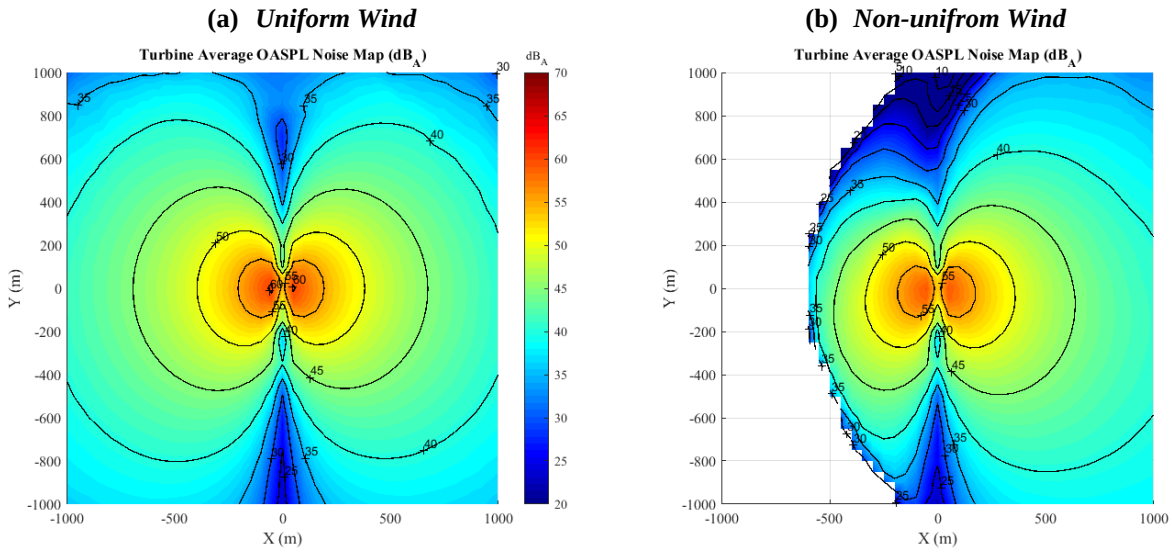

Figure 59: The NREL 5MW turbine OASPL noise map **(a)** for cases 0 and **(b)** 1.

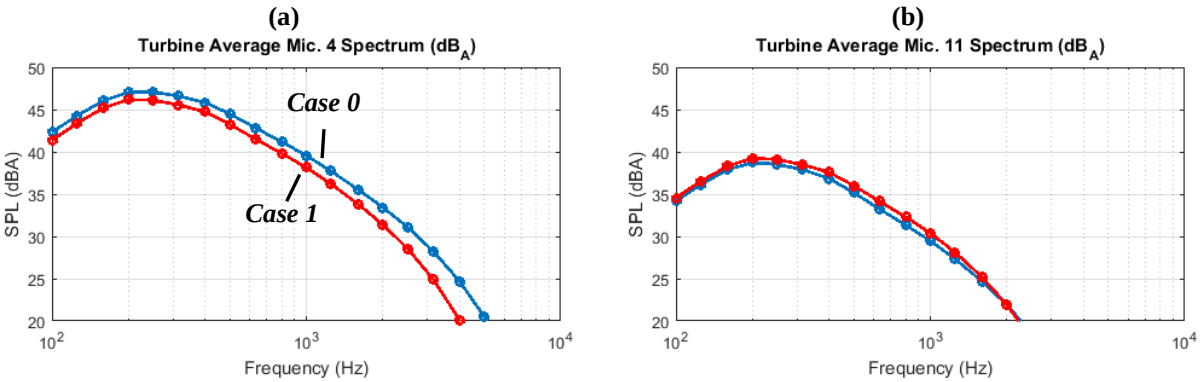

Figure 60: Noise spectrum in 1/3rd octave bands for microphones (a) 4 and (b) 11.

4.3.3 Results for Case 2

This case allows to assess the effect of rotor tilt and pre-cone angles. These parameters are always implemented in large turbine, i.e. they cannot be changed. The tilt and pre-cone angles have influence on the aerodynamic parameters because the blade encounters different axial and tangential wind components as the blade rotates as compared to the baseline (case 0). Figure 61a shows the AoA distribution over the rotor plane. The effect of tilt and pre-cone angles on the AoA change is very small, e.g. comparing Figures 61a to 58a. The overall sound power level distribution on the rotor plane is plotted in Figure 61b. The maximum values at the rotor top and bottom are 97.2 dBA and 95.7 dBA, respectively. The magnitude has no noticeable change compared to case 1 (Figure 58b).

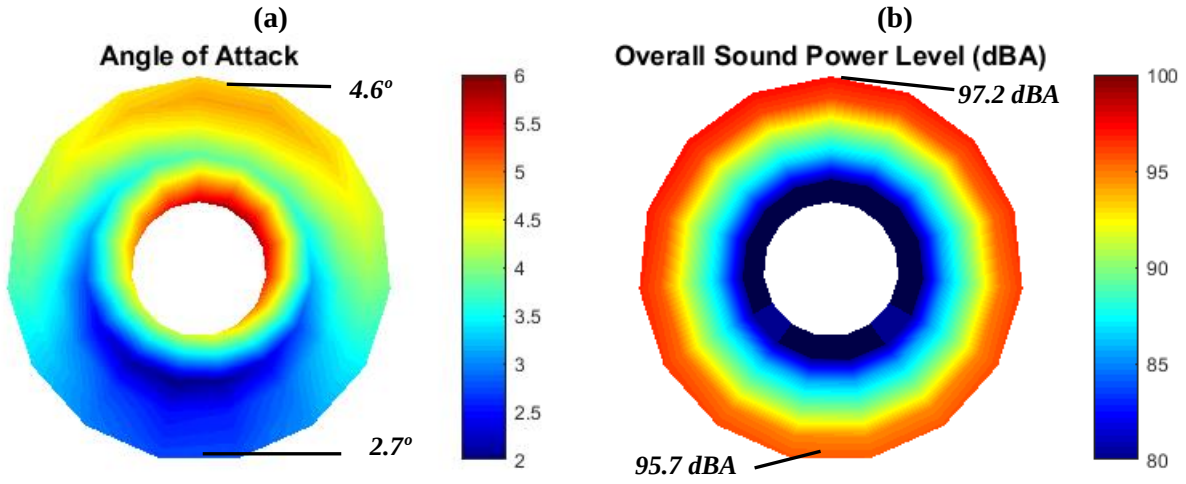

Figure 61: (a) AoA and **(b)** source overall sound power level distributions over the rotor for case 2, NREL 5MW turbine with rigid blades.

These turbine parameters affect the sound sphere placement as shown in Figure 62. The sound sources are rotated slightly depending on its position on the rotor. For example, source 5 get rotated 2.5°down due to the tilt and cone angles. The most dominant radiation direction is now pointing more towards the ground in the downwind direction. On the other hand, the sources at the bottom position of the rotor are rotated 7.5° and also pointing more towards the ground. In short, the sound spheres are placed differently in the global coordinates and the directivity change due to the rotation of the blades through tilt and cone angles. Figure 63 shows the OASPL noise map which reveals small differences as compared to case 1 in Figure 59b. The highest SPL region (> 55 dBA) near the turbine extends over a larger area than for case 1. The SPL spectrum of microphones 4 and 11 are shown in Figure 64. There is no significant change compared to case 1, i.e. the SPL almost overlay on each other throughout all frequencies. Therefore, this case demonstrates that the tilt and pre-cone angles have minor effects on the ground noise.

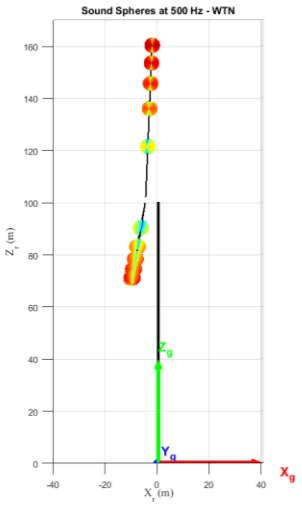

Figure 62: The NREL 5MW turbine configuration and the sound spheres for case 2. The rotor tilt and the blade pre-cone are also shown.

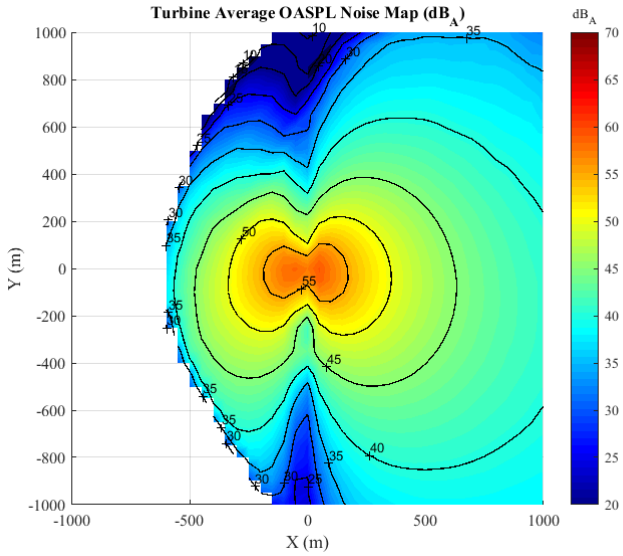

Figure 63: The NREL 5MW turbine OASPL noise map for case 2.

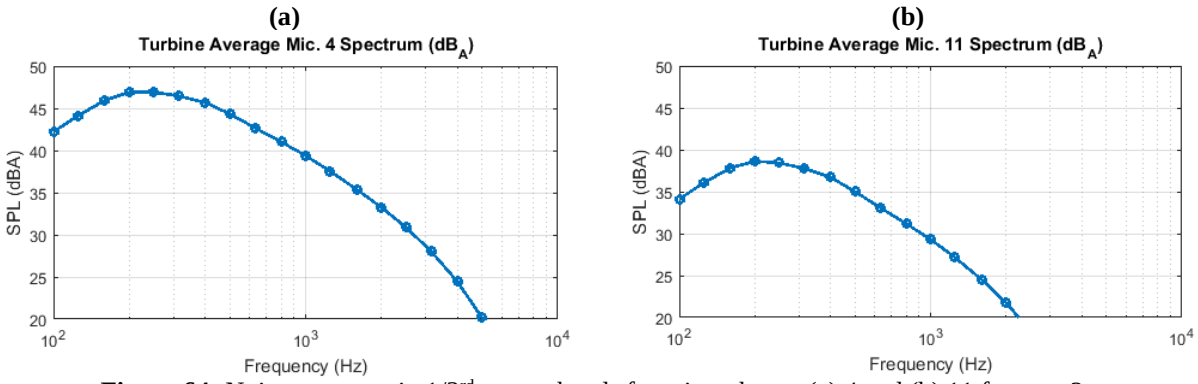

Figure 64: Noise spectrum in 1/3rd octave bands for microphones (a) 4 and (b) 11 for case 2.

4.3.4 Results for Case 3

This case allows to assess the effect of yaw angle, i.e. the turbine is misaligned with the incoming flow. This case leads to significant changes on the AoA distribution over the rotor plane as shown in Figure 65a. The location of the maximum AoA at the blade tip is rotated ~90° compared to case 2 (Figure 61a) and the magnitude is around 1.0° less than case 2. Figure 65b shows the overall sound power level distribution and the maximum SPL occurs at the blade tip as previous cases shown. However, the location of maximum value does not rotate like the AoA distribution does. It is due to the relative inflow that is still the dominating factor over the AoA for the noise prediction. The relative inflow is still highest at the top position even with the yaw angle. The maximum sound power level is only 0.5 dBA higher than case 2 (Figure 61b).

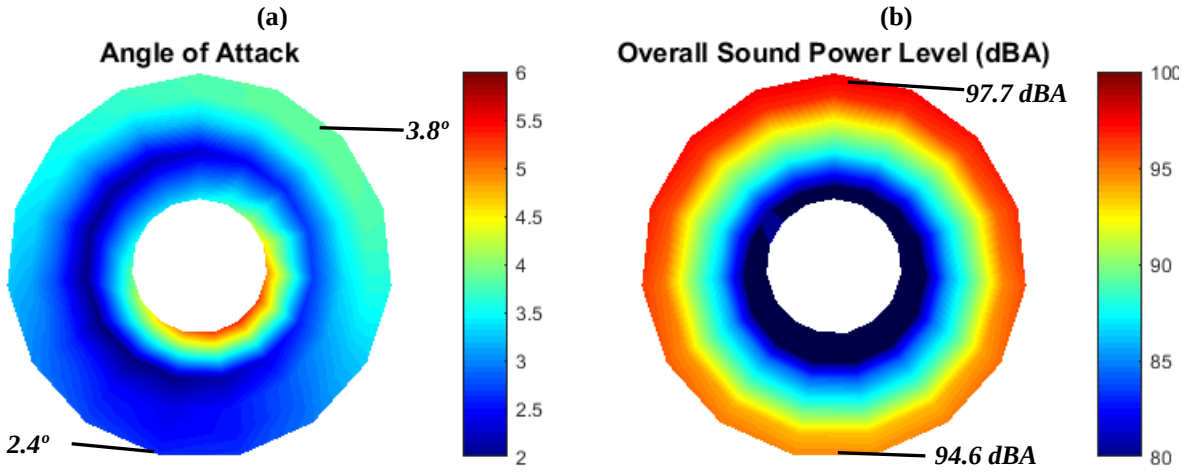

Figure 65: (a) AoA and **(b)** source overall sound power level distributions over the rotor for case 3, NREL 5MW turbine with rigid blades.

The turbine yaw angle affects the sound sphere placement and orientation as shown in Figure 66. The sound sphere directivity is still dominated (highest SPLs) in the directions that are normal to the rotor plane. This effect is very clear in the noise map shown in Figure 67. The noise propagates in the direction that is the resultant vector of the yaw angle and the wind. The result indicates that the yaw angle is a dominant factor. Figure 68 shows the SPL spectrum at microphones 4 and 11 along with the case 2 results. The SPLs are again very similar to case 2 because the turbine radiates very much like a monopole source in the downwind directions. Overall, the effect of the turbine yaw is a rotation of the noise maps.

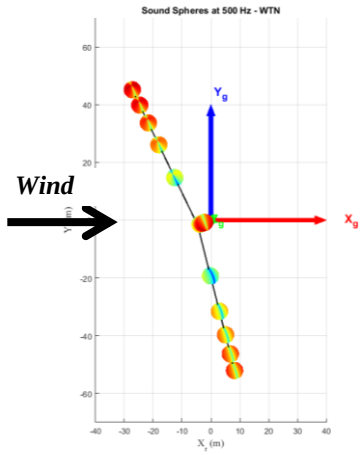

Figure 66: The NREL 5MW turbine top view and the sound spheres for case 3. The yaw, tilt and pre-cone angles are also shown.

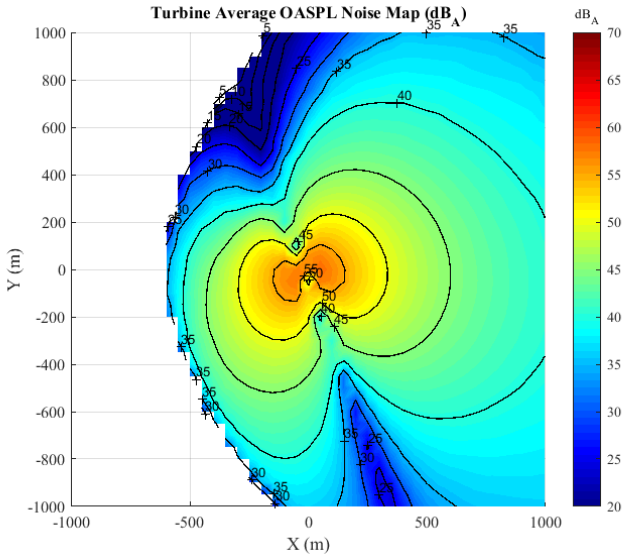

Figure 67: The NREL 5MW turbine OASPL noise map for case 3. The noise no longer propagates in the x direction, as shown in case 2, but propagates at an angle (~< 20°).

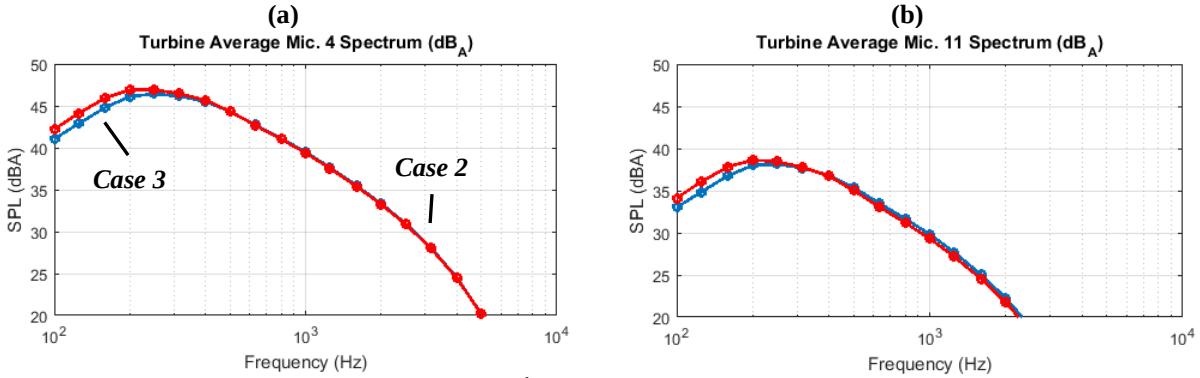

Figure 68: Noise spectrum in 1/3rd octave bands for microphones (a) 4 and (b) 11.

4.3.5 Results for Case 4

In this case, the wind direction is at an angle relative to the rotor axis. Thus, this case is identical to case 3 (the NREL 5MW turbine with 20° yaw) from the aerodynamic point of view, i.e. the inflow and rotor are misaligned by 20°. Therefore, the aerodynamic parameters and noise source levels are the same. The AoA and OASPL distributions over the rotor plane are identical as shown in Figure 65. Figure 69 shows the skewed inflow wind associated with all the noise spheres. Figure 70 shows the resulting noise map. Although the inflow wind comes in at an angle, it has no significant effect on the noise map, i.e. the turbine noise still propagates primarily in the directions that are normal to the rotor plane. In fact, the noise map result (the OASPL and contour regions) is very similar to case 2 (Figure 63), where the yaw angle is also 0°.

The sound spectrum from the microphones 4 and 11 are shown in Figure 71. The results show not much differences compared to case 3. Therefore, this case demonstrates that the wind angle do not have significant effect on the noise propagation.

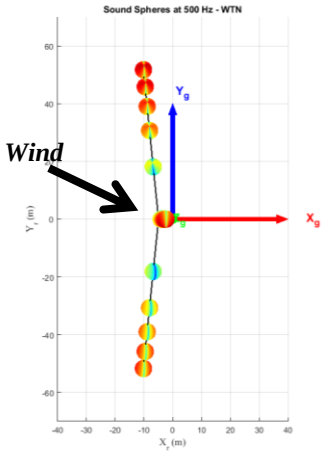

Figure 69: The NREL 5MW turbine top view and the sound spheres for case 4 with the skewed incoming wind.

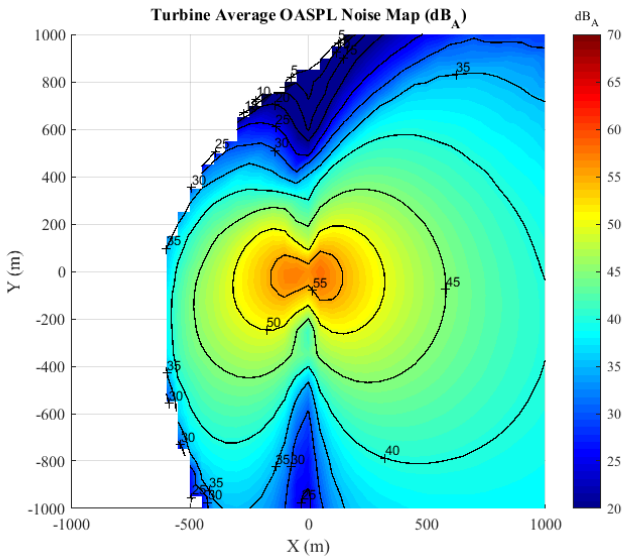

Figure 70: The NREL 5MW turbine OASPL noise map for case 4.

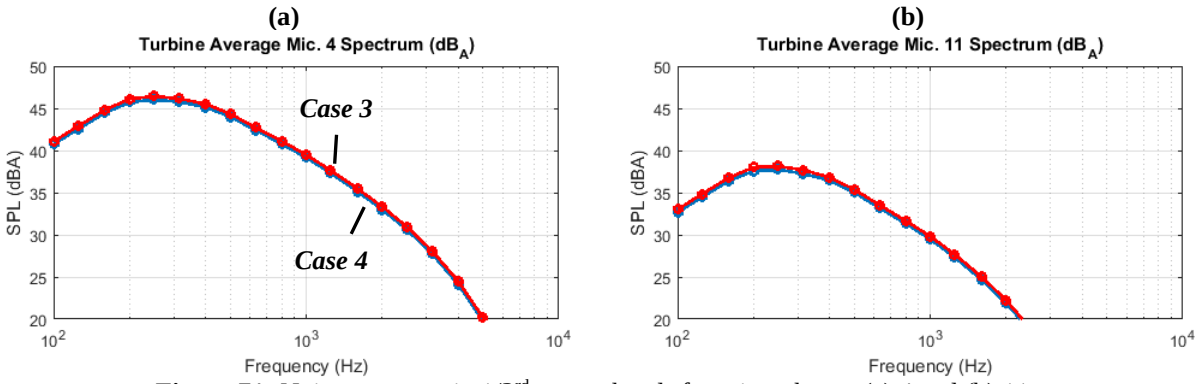

Figure 71: Noise spectrum in 1/3rd octave bands for microphones (a) 4 and (b) 11.

4.3.6 Results for Case 5

This case allows to assess the effect of blades aeroelasticity. The blade deflections influence the aerodynamics, noise source placements, and orientations. In this case, the aerodynamic load varies with respect to the rotor azimuth position due to the non-uniform wind condition, resulting in blade deflection changing over the rotor plane. Figure 72a shows the blade *x*-axis displacement relative to the undeformed blade over a revolution in the steady-state condition. The displacement is non-axisymmetric and increases radially. As expected, the blade behaves as a cantilevered beam that has the highest deflection at the end. The minimum and maximum blade tip displacements occur at the bottom and top positions. The blade deflection angle (rotational displacement about the blade y-axis as illustrated in Figure 18) shown in Figure 72b has the same trend as the blade displacement. The maximum deflection angle at the blade tip is 11.1°. The AoA distribution with

the blade elasticity effects is shown in Figure 72c. The AoA magnitude is lower than case 2 (the rigid blade case, Figure 61a) for around 1° due to the blade deflection. This finding is similar to the work done by Kim [24] that the elastic blade has lower AoA than the rigid blade. The overall sound power level distribution follows the same trend as shown in Figure 72d. The difference is only less than 0.5 dBA lower compared to the case 2 (Figure 61b).

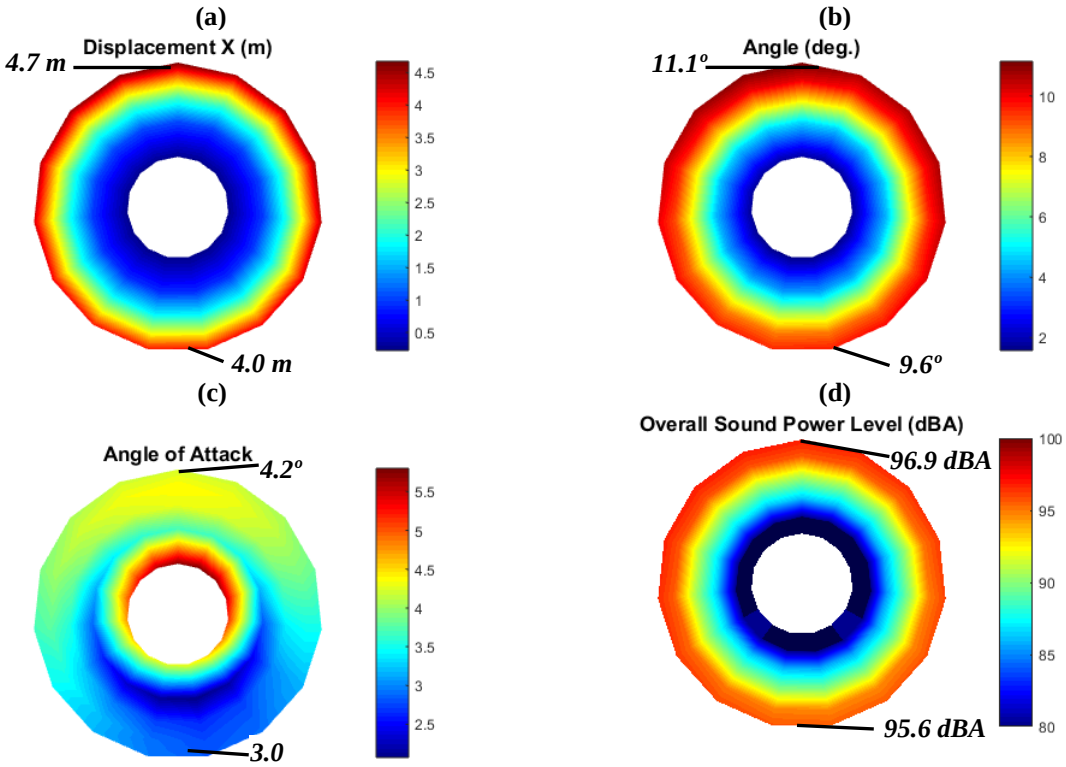

Figure 72: **(a)** The *x*-displacement deformation, **(b)** deflection angle, **(c)** AoA, and **(d)** source overall sound power level distribution over the rotor for case 5: NREL 5MW turbine with elastic blades**.**

Figure 73 shows the un-deformed and deflected blades in the solid and dash lines, respectively. The sound sphere placements and orientations change according to the deflected blades. The outer sound spheres on the deflected blade are being rotated 11.1° down towards the ground in the upper position and up in the bottom position of the rotor. All are moved 4.7 m in the downwind direction relative to the un-deflected blade. Figure 73b shows the deflection angle changes the sound sphere orientations compared to case 2 (Figure 62). Figure 73c shows changes on the noise source placements due to the blade deformation.

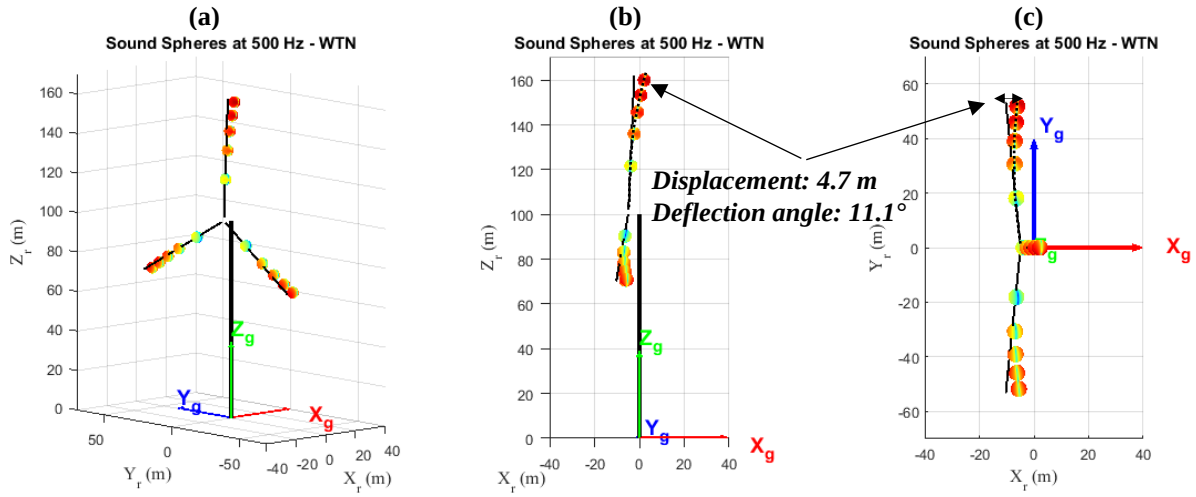

Figure 73: The NREL 5MW turbine and the sound spheres associate with the flexible blades, **(a)** isometric, **(b)** side, and **(c)** top views. The un-deflected blades (rigid) are shown in black solid lines.

The noise map including the blade elasticity is shown in Figure 74. There are no observable differences for the noise level on the ground compared to case 2 (Figure 63). The changes in orientation and placement of the sound spheres do not show strong influences on the noise propagation. The SPL spectrum of cases 2 and 5 for the microphone 4 and 11 are shown in Figure 75. The magnitude has insignificant changes, demonstrating that the blade aeroelasticity does not have a strong influence on the turbine noise.

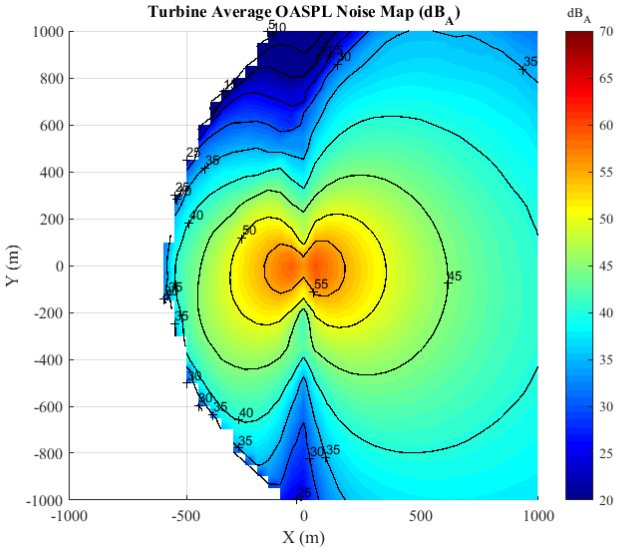

Figure 74: The NREL 5MW turbine OASPL noise map for case 5.

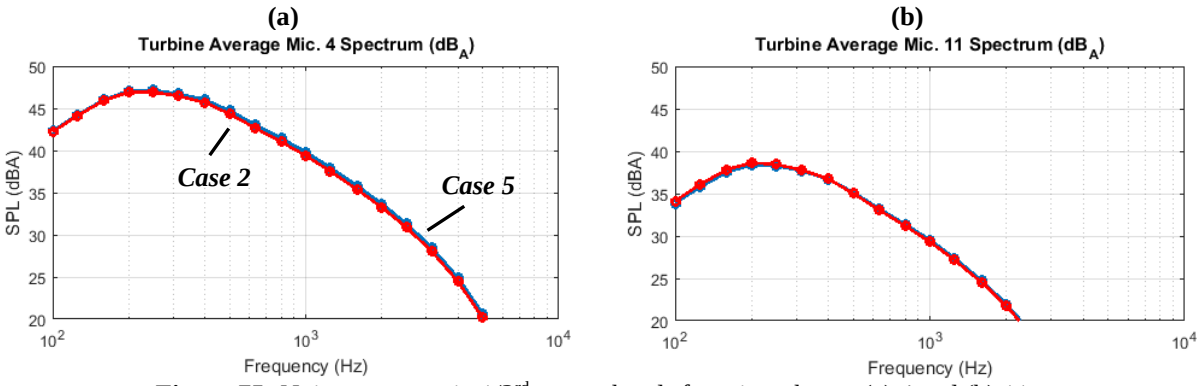

Figure 75: Noise spectrum in 1/3rd octave bands for microphones (a) 4 and (b) 11.

4.3.7 Result for Case 6

This case allows to assess the effect of large rotor size with the Sandia 13.2 MW turbine. The rotor experiences uniform wind with 14 m/s as result of its higher hub height than the NREL 5MW turbine. Figure 76a shows the AoA distribution over the rotor plane from 30% to 100% of the SNL100-20 blade span. The AoA at the blade tip is almost uniformly distributed with a small variation. The variation is because the turbine tilt and pre-cone angles. The overall sound power level distribution is shown in Figure 76b with 103.6 dBA near the blade tip region as result of the AoA and relative inflow speed. Figure 77 shows total noise spectrums of source 1 and 5 (see Figure 50b for the locations). The SPL is higher compared to case 0 (Figure 52) at both source locations for approximately 10.9 dB. The peaks for the Sandia 13.2MW blade also move toward low frequencies as the result of the larger chord length has lower noise frequencies. In particular, the SPL at source 5 is higher than case 0 (Figure 52b) across all frequencies. These findings confirm that the Sandia 13.2MW turbine has high noise emission than the NREL 5MW due to its longer blade span.

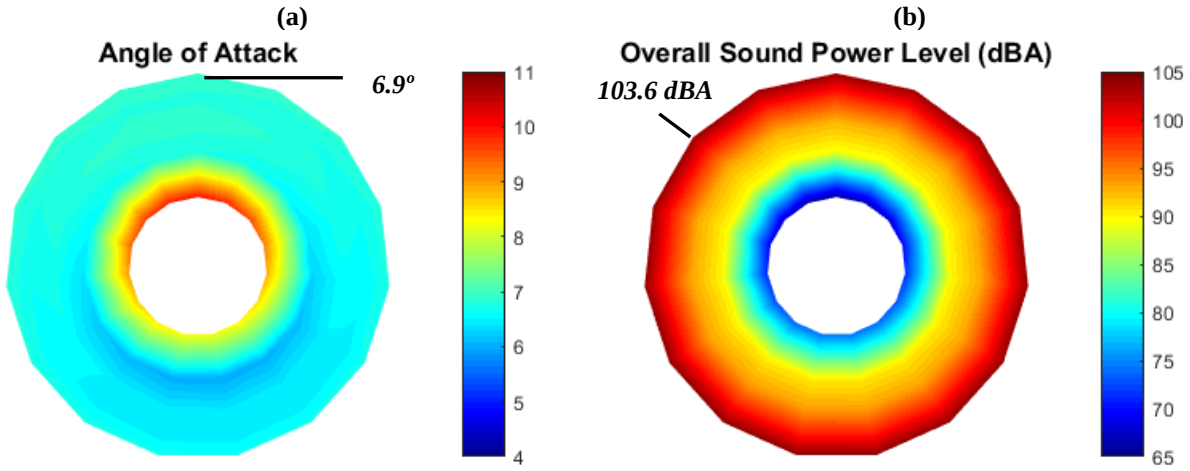

Figure 76: The blade **(a)** AoA and **(b)** source overall sound power level distribution over the rotor for case 6, Sandia 13.2MW turbine with rigid blades.

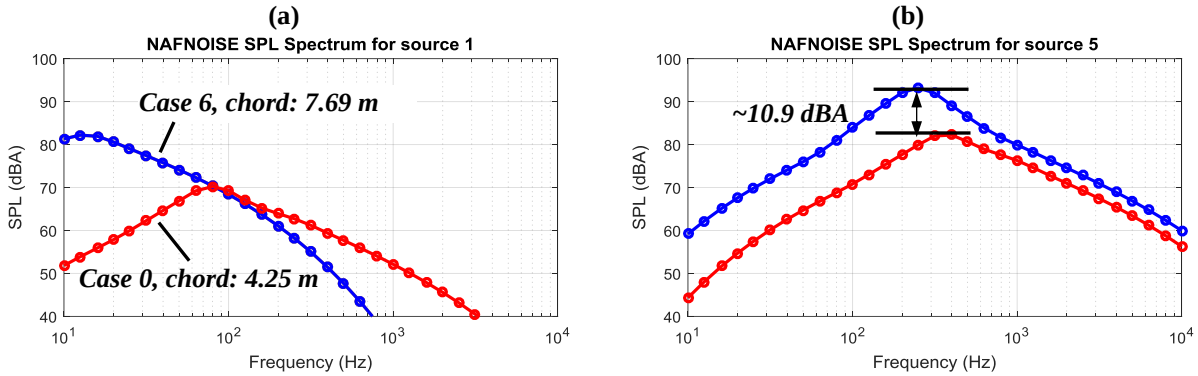

Figure 77: The SPL spectrum of the NREL 5MW and the Sandia 13.2 MW turbines at **(a)** source 1 and **(b)** 5. Only the total noise SPLs are shown.

The noise maps shown in Figure 78 demonstrates the Sandia 13.2 MW turbine generates high noise level, resulting in higher SPL in the upwind and downwind directions. For example, the noise level remains ~50.0 dBA at 1000 m away from the turbine but only ~40.5 dBA for case 0 (Figure 78a). The SPL spectrums of the two selected downwind microphones are shown in Figure 79. Microphone 6 is located 250 m away from the turbine, which predicts the noise according to the IEC 61400-11 (146.4 m tower height + 206/2 m rotor radius). The microphone 11 is at the same location as case 0 (500 m away). The maximum SPL for microphones 6 and 11 are 52.4 dBA and 47.7 dBA, respectively. The SPL spectrum at microphone 11 confirms that case 6 has higher SPL across all frequencies compared to case 0 (Figure 57). Therefore, this case successfully demonstrates that larger rotor size generates higher turbine noise level.

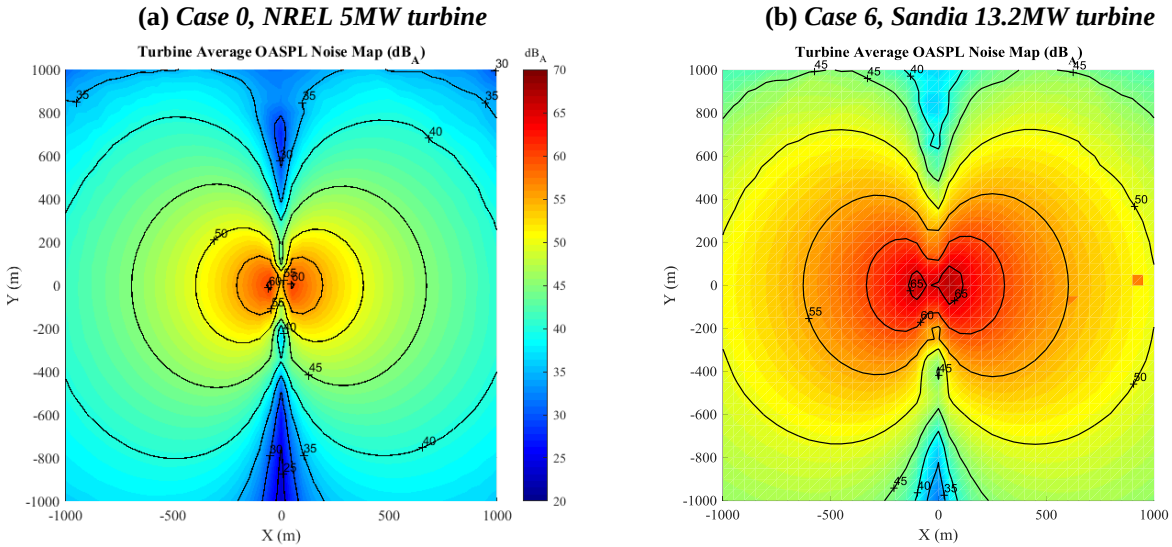

Figure 78: The OASPL noise maps for **(a)** case 0 (the NREL 5MW) and **(b)** case 6 (the Sandia 13.2MW)

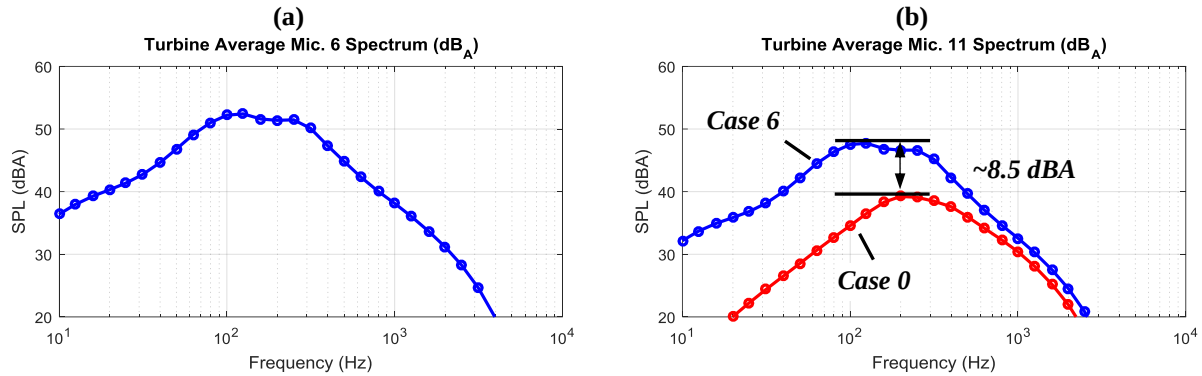

Figure 79: Noise spectrum in 1/3rd octave bands for microphones **(a)** 6 and **(b)** 11.

4.3.8 Result for Case 7

This case allows to assess the effect of large rotor size under the non-uniform wind profile, where the wind speed at the rotor top and bottom are 21 m/s and 8.4 m/s, respectively. As expected, the AoA distribution over the rotor has large variations due to the wind profile as shown in Figure 80a. The magnitude is increased due to the higher wind speed at the rotor top. The overall sound power level distribution is shown in Figure 80b. The case 7 is 6.8 dB higher than case 2 (the NREL 5MW turbine under the same non-uniform wind profile, see Figure 61b). In particular, the SPL at the blade tip are significantly high due to the high relative inflow speed. Total noise spectrums of the source 1 and 5 are shown in Figure 81. At the source 5 location, the magnitude is higher than case 2 across all frequencies. In addition, there is 11.9 dB increase at the peak.

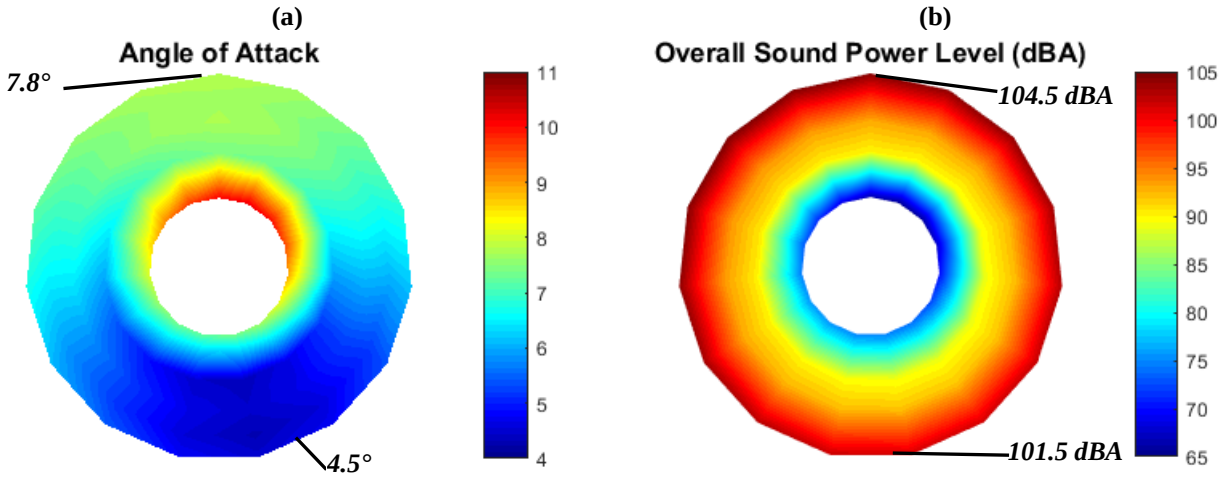

Figure 80: The blade **(a)** AoA and **(b)** source overall sound power level distribution over the rotor for case 7, Sandia 13.2MW turbine with rigid blades**.**

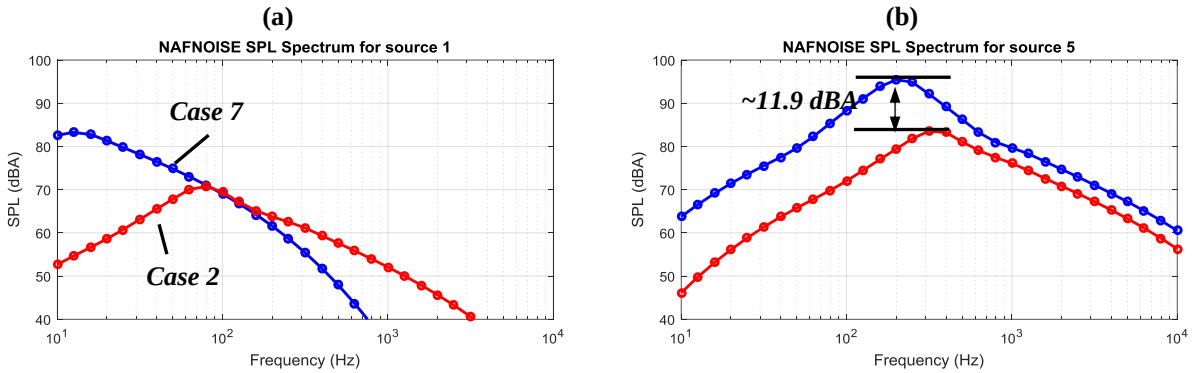

Figure 81: The SPL spectrum of cases 2 and 7 at **(a)** source 1 and **(b)** 5. Only the total noise SPLs are shown.

Figure 82 compared the noise maps for the cases 2 and 7. It is obvious that Sandia 13.2MW generates more noise than NREL 5MW turbine. The noise level for the Case 7 reach up to 65.0 dBA near the turbine and has around 60.0 dBA within 300 m in upwind and downwind directions. In the case 2, the highest SPL is only around 58.0 dBA near the wind turbine. In addition, the shadow zone in this case is smaller than case 2, indicating the noise propagates further in the upwind direction due to its large rotor size. The SPL spectrums of the microphones 6 and 11 are shown in Figure 83. Typically, the SPL decreases 6 dB as the distance doubled. However, as shown in Figure 83c, there is only 4.3 dB decrease between microphone 6 (250 m) and 11 (500 m) because the wind profile bends the rays downward in downwind direction. In addition, the microphone 11 spectrum from cases 2 and 7 are compared in Figure 83d. The case 7 has higher SPL across all frequencies. Therefore, the large rotor size also yields high noise emission in long distances under the non-uniform wind profile.

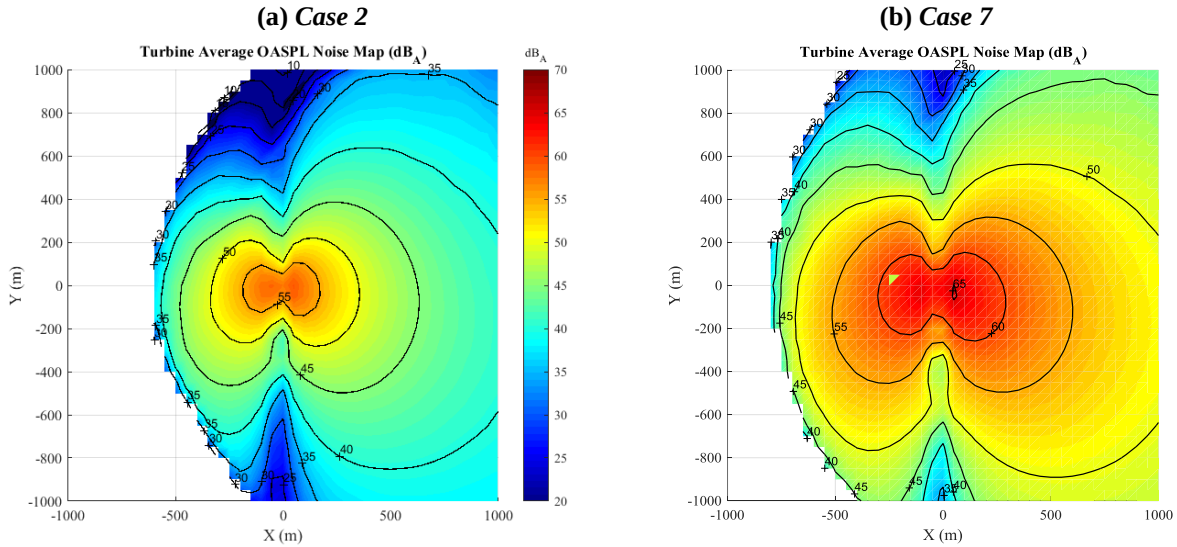

Figure 82: The OASPL noise maps for **(a)** case 2 (the NREL 5MW) and **(b)** 7 (the Sandia 13.2MW).

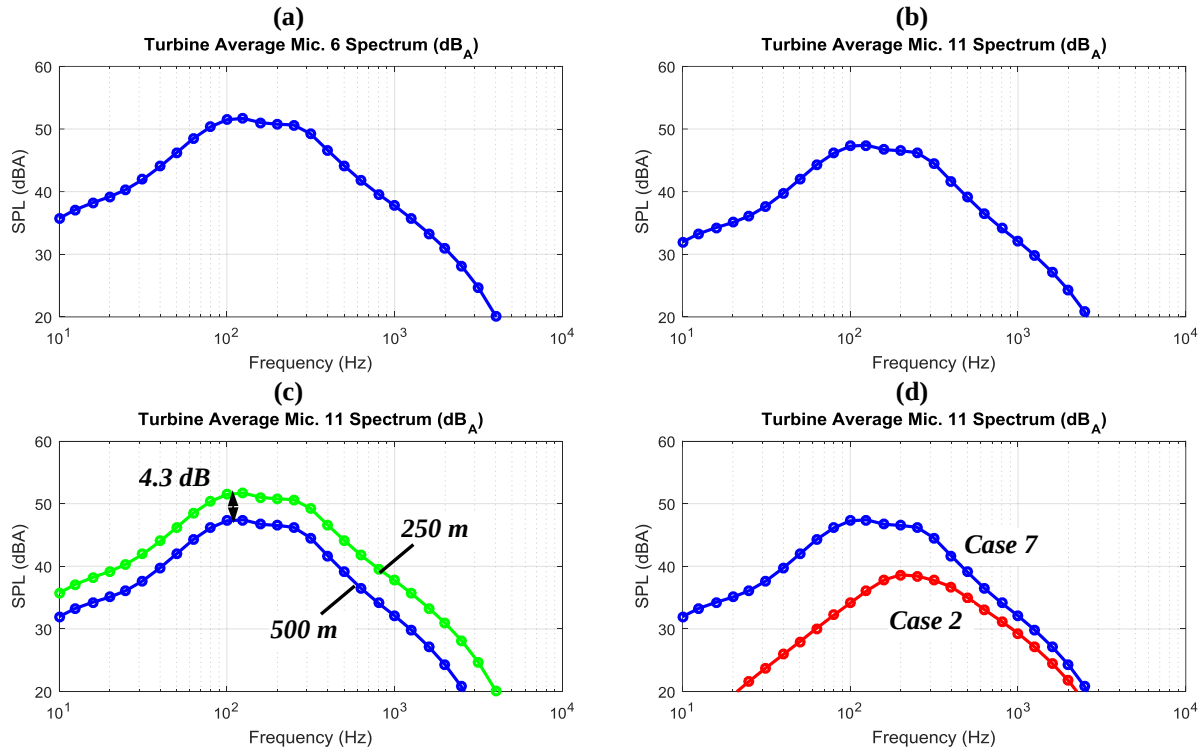

Figure 83: Noise spectrum in 1/3rd octave bands for microphones **(a)** 6 and **(b)** 11 for case 7. **(c)** A comparison of the SPL spectrum of the two microphone locations for case 7. **(d)** A comparison of the SPL spectrum at microphone 11.

4.3.9 Result for Case 8

This case allows to assess the effects of blade aeroelasticity on the large turbine under the uniform wind (14 m/s). Figure 84a shows the blade displacement in the downwind direction over the rotor plane. The blade deflects 6.7 m at the tip as it is nearly axisymmetric. The deflection angle (rotational displacement about the blade y-axis) shows the same trend as illustrated in Figure 84b, around 9.2° at the tip. The AoA distribution is shown in Figure 84c. There are no significant changes in the magnitude as compared to the rigid blade in case 6 (Figure 76a), e.g. AoA increases from 6.9º to 7.1º. The overall sound power level distribution is shown in Figure 84d. There is no change observed compared to case 6 (Figure 76b). In addition, the source noise spectrum at the blade tip, e.g. source 5, overlays with case 6 (Figure 77b), confirming that the blade aeroelasticity has minor effects on the average noise level.

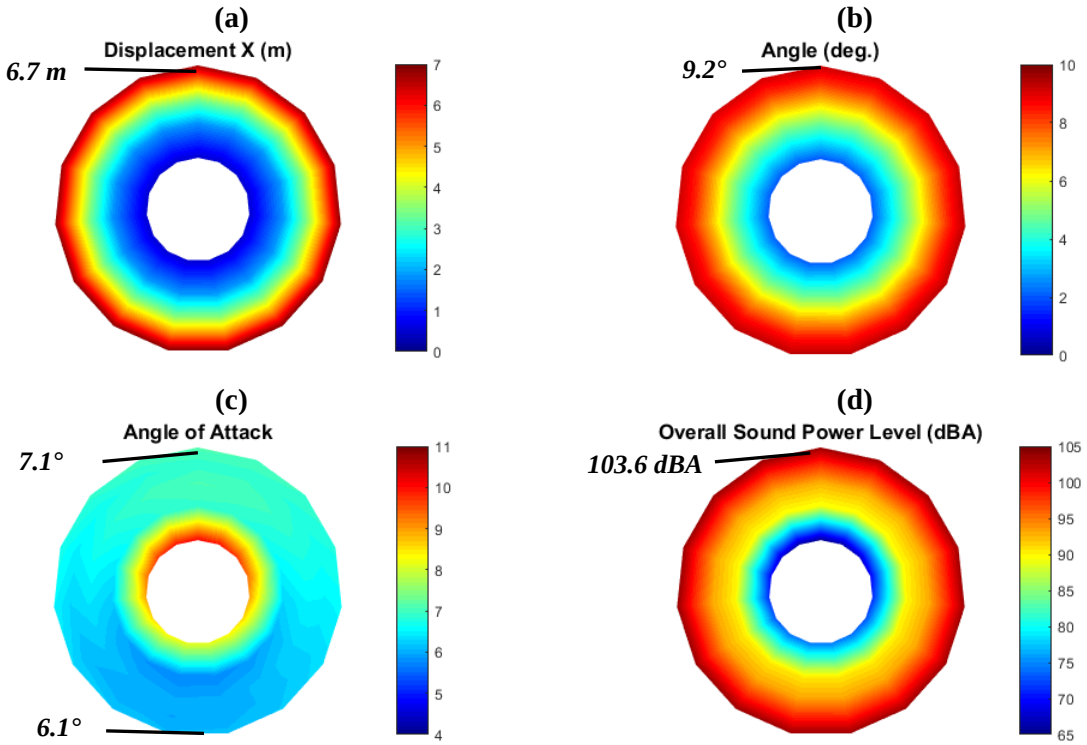

Figure 84: The blade **(a)** *x*-displacement deformation, **(b)** deflection angle, **(c)** AoA, and **(d)** source overall sound power level distribution over the rotor for case 8, Sandia 13.2MW turbine with elastic blades**.**

The OASPL noise map is shown in Figure 85 illustrating no significant changes by comparing the two cases (6 and 8). However, the case 8 shows less noise level near the bottom of the turbine in the downwind direction compared to case 6. Notice that the same trend is shown from the previous

work by Kim (Figure 8) [24]. Also, the case 8 has lower noise level in the upwind direction 100m away for ~3.0 dBA lower than case 6.

The SPL spectrums for the microphone 6 and 11 are shown in Figure 86 and there are significance differences confirming that the blade aeroelasticity has minor effects for the average noise in the downwind.

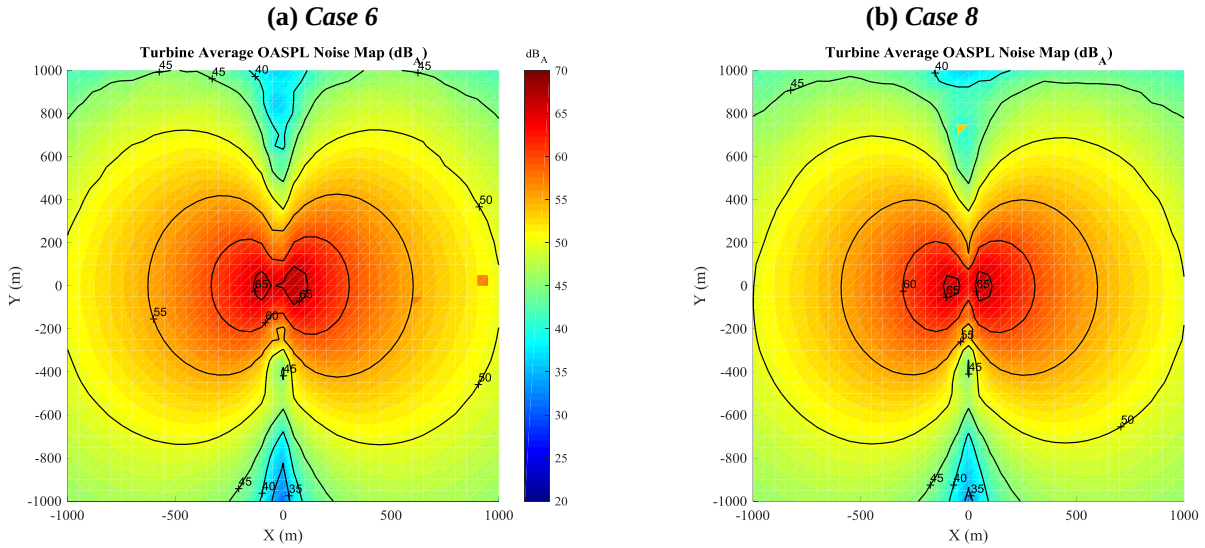

Figure 85: The Sandia 13.2MW turbine OASPL noise maps for **(a)** case 6 (rigid blade2) and **(b)** 8 (flexible blades).

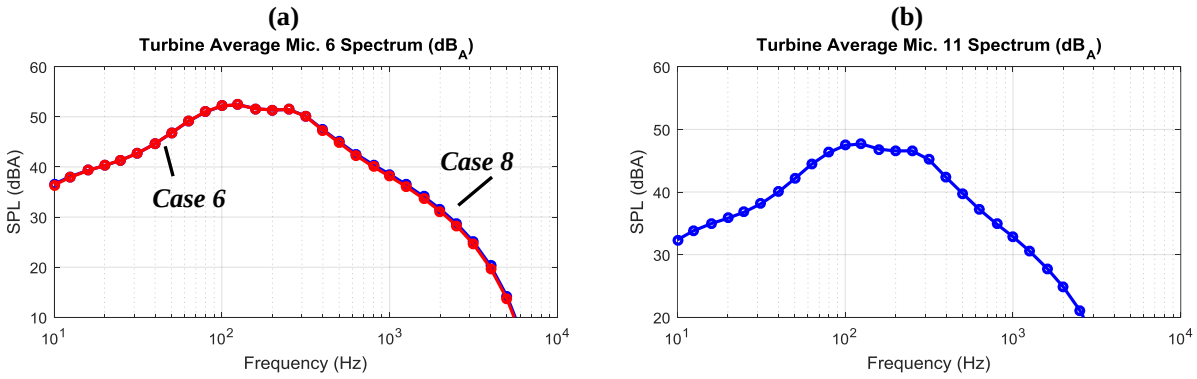

Figure 86: Noise spectrum in 1/3rd octave bands for microphones **(a)** 6 and **(b)** 11.

4.3.10 Result for Case 9

This case allows to assess the effect of blade aeroelasticity on the large wind turbine under the non-uniform wind profile. The blade deflection distribution has large variations over the rotor due

to the different aerodynamic loads at the rotor top (21 m/s) and bottom (8.4 m/s). Figure 87a shows the blade *x*-axis displacement distribution over the rotor in the steady-state condition. The maximum deflection is 7.3 m, which is higher compared to the 4.7m maximum deflection for the NREL 5MW flexible blades in case 5 (Figure 72a). This result is expected not only due to the higher wind speed at the rotor top, but also the longer blade span for the Sandia 13.2MW turbine. The deflection angle (rotational displacement about the blade y-axis) distribution over the rotor is shown in Figure 87b. The angle is 1.3° less than for the NREL turbine (case 5 and Figure 72b). The AoA distribution is shown in Figure 87c. The maximum and minimum AoA are 7.3° and 4.7° at the rotor top and bottom, respectively. There is no noticeable changes in the magnitude under the effect of blade aeroelasticity compared to case 7 (the Sandia 13.2MW with rigid blade assumption, see Figure 80a). The overall sound power level distribution is shown in Figure 87d. It has the same trend as the AoA distribution. The levels are only slightly affected by the blade aeroelasticity (~ -0.2 dB differences).

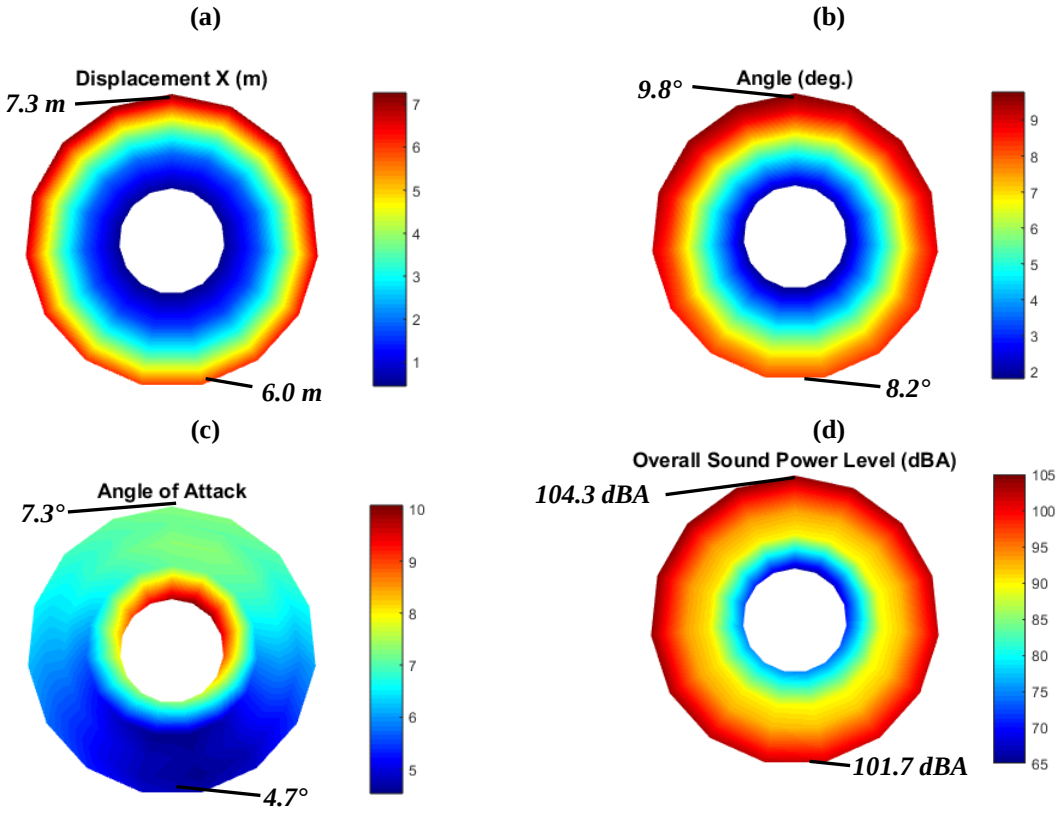

Figure 87: The blade **(a)** *x*-displacement deformation, **(b)** deflection angle, **(c)** AoA, and **(d)** source overall sound power level distribution over the rotor for case 9, Sandia 13.2MW turbine with elastic blades**.**

The noise spectrum for source 5 is shown in Figure 88. The spectrum for the rigid blade (case 7) is also plotted in the same figure The deformation of the blade (case 9) decreases the levels by approximately 2.0 dB as compared to the rigid blade (case 7) at very low frequencies (<150 Hz).

The noise map is shown in Figure 89b while Figure 89a shows the noise map for case 7 (rigid blade). Comparison of these maps shows very small differences. This observation is again confirmed by the nose spectrum of microphones 6 and 11 shown in Figure 90. Therefore, even for a large wind turbine that undergoes large blade deflection, the blade aeroelasticity do not demonstrate a strong influences on the average OASPL noise level.

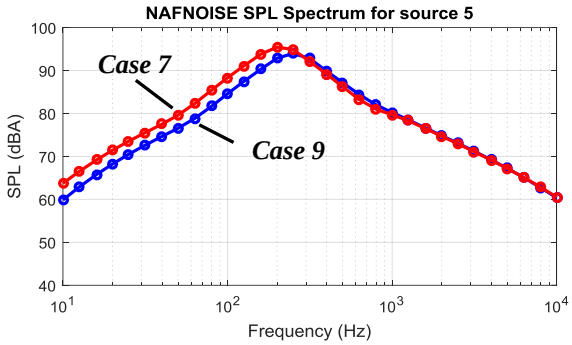

Figure 88: The total noise SPL spectrum at source 5.

(a) ***Case 7*** **(b)** ***Case 9***

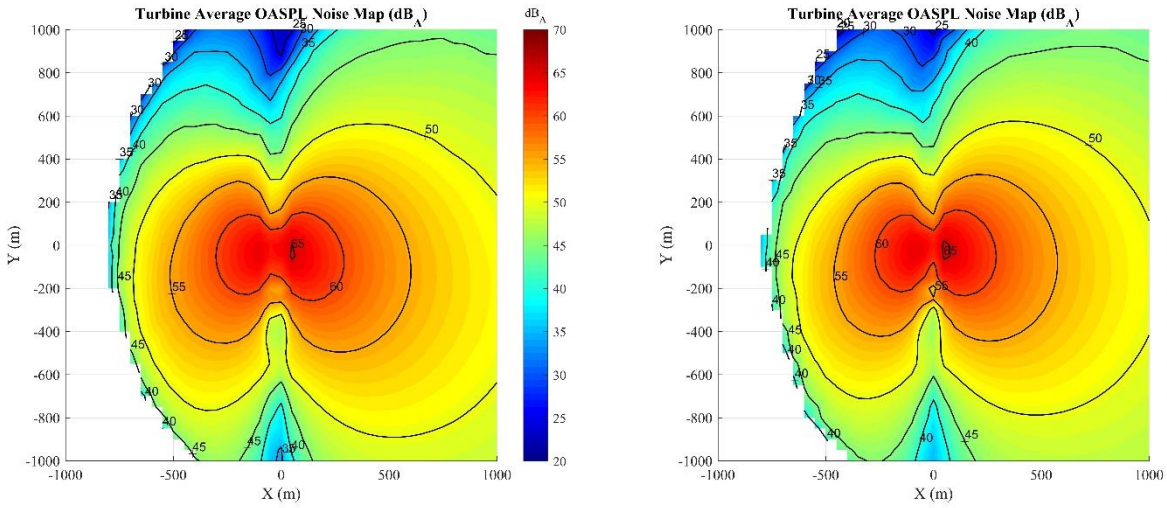

Figure 89: The Sandia 13.2Mw turbine OASPL noise maps for **(a)** case 7 (rigid blades) and **(b)** 9 (flexible blade).

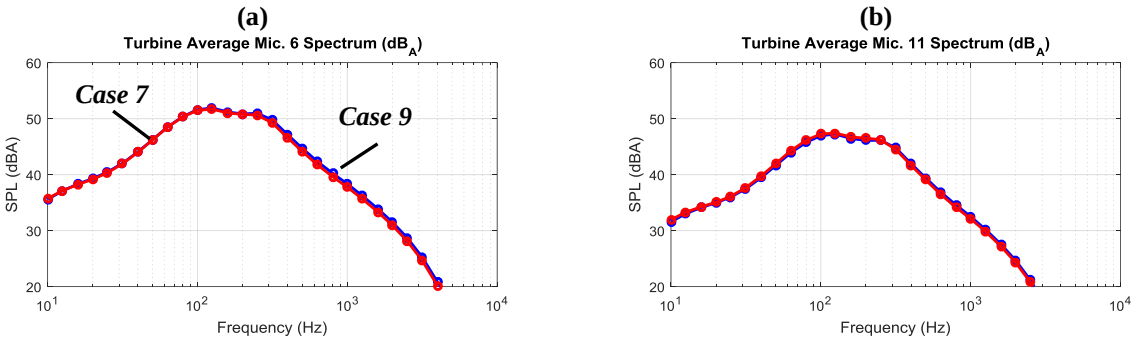

Figure 90: Noise spectrum in 1/3rd octave bands for microphones (a) 6 and (b) 11.

5. Conclusions and Future Work

This section discusses the conclusion and recommended future work of this thesis.

Conclusions

The present work merges a wind turbine aeroelastic code, FAST (Fatigue, Aerodynamics, Structures, and Turbulence) to a wind turbine noise code, WTNoise, to compute turbine noise accounting for blade aeroelasticity. FAST accounts for the blade aeroelastic effects in calculations of the turbine aerodynamic parameters, which are inputs to the WTNoise noise model. The turbine noise predictions are based on the airfoil self-noise model that accounts for the geometric characteristics of the airfoils both in levels and directivity. The noise propagation model is able to account for the actual turbine radiation characteristics and real meteorological conditions (wind and temperature). Using the newly developed simulation tool, the effects of rigid and flexible blades on wind turbine noise are investigated, as well as the effects of the turbine parameters, e.g. wind conditions, rotor size, tilt, yaw, and pre-cone angles. The acoustic results are shown as long term average overall sound power level distribution over the rotor, ground noise map over a large flat terrain (2 km x 2 km), and noise spectrum at selected locations downwind.

The blade deflections in the blade *y* and *z*-axis (e.g. in the rotor plane) are not accounted for due to their insignificant small values. The rotational displacements associated to these two translational displacements are also very small and disregarded. The trailing-edge bluntness vortex shedding and turbulent inflow noise components are not modeled in the airfoil self-noise model due to the sharp trailing edge airfoils and absence of inflow turbulences. In this work, there is no mechanical noise contribution from the turbine. There is no vertical wind component since the terrain is flat.

Two large wind turbine are modeled. The first one is the NREL 5MW turbine that has a rotor diameter of 126 m. The second wind turbine, the Sandia 13.2MW, has a rotor diameter of 206 m. They both employed the same blade geometry design (DU family and NACA 64 airfoils) but the blade spans are 61.5 m and 100 m for the NREL 5MW and Sandia 13.2 MW turbine, respectively. It is also important to mention that the Sandia 13.2 MW has different blade structure than the

NREL 5MW blade, resulting in different blade deflections. The effects of turbine parameters and blade aeroelasticity have been assessed using these two wind turbines.

The results show that the wind condition has strong effects on the noise propagation over long distances, primarily in the upwind direction where shadow zones are present. In general, the turbine parameters have no significant effects on the ***average*** noise level. However, the turbine yaw impacts significantly the noise maps. The rotor size is also a dominating factor in the turbine noise level. For example, under the same non-uniform wind profile, the NREL 5MW turbine has maximum overall sound power level 97.2 dBA at the blade tip, but the Sandia 13.2 MW can reach up to 103.6 dBA. Finally, the blade aeroelasticity has minor effects on the turbine ***average*** noise level. In summary, a comprehensive tool for wind turbine noise prediction including blade aeroelasticity was developed and it was used to address its impact on the large turbine noise emissions.

Future Work

The following are a set of research recommendations for future work. As mentioned before, the study focuses on the wind turbines under nominal wind conditions, e.g. uniform wind or power-law wind profile at low reference wind speeds. In this case, the blades are well behaved aerodynamically with flow always attached over the blades, e.g. no flow separation or stall conditions. In reality, large wind turbines undergo more severe wind conditions, e.g. strong wind gradient or inflow angle that potentially can result in separated flow and a dramatic increases in the turbine noise emissions. The IEC 61400-1 has established multiple operating and extreme wind conditions as wind turbine design requirements. For example, the extreme operating gust (EOG) wind has a wind speed variation from 22m/s to 34 m/s in 10 seconds [10]. Therefore, the turbine noise prediction should be investigated under the IEC 61400-1 wind conditions. In addition, inflow turbulences can be included to investigate the effects on the turbine aerodynamics, noise source level, and propagation.

Another recommendation is to investigate the effect of blade pitch. The modern wind turbine has pitch controls on the blades to reduce aerodynamic loads by changing the blade pitch angle. However, changing the blade pitch affects the AoA of the entire blade. The blade tip AoA may

decrease to negative values and flow separation or stall can occurs. Investigations on the turbine noise under the effects of blade pitch angles should be conducted.

Finally, it is recommended to improve the noise propagation model to capture the turbine wake flow condition, e.g. flow rotational downwind from the rotor or swirl. Therefore, the sound field behind the rotor may be affected by this phenomenon. Capturing this effect will improve the turbine noise prediction in the downwind direction.

References

1. *Ganesh, R., R.C. Ramachandran, and M.R. Aldeman, A review of wind turbine noise measurements and regulations. Wind Engineering, 2016. 40(4): p. 319-342.*
2. *Griffith, D. and P.W. Richards, The SNL100-03 Blade: Design Studies with Flatback Airfoils for the Sandia 100-meter Blade. 2014, ; Sandia National Laboratories (SNL-NM), Albuquerque, NM (United States). p. Medium: ED; Size: 40 p.*
3. *Johan Peeringa, R.B., Ozlem Ceyhan, Wouter Engels, Gerben de Winkel, Upwind 20MW Wind Turbine Pre-Design: Blade Design and Control. December 2011, Energy research Centre of the Netherlands (ECN)*
4. *Griffith, T. Enormous blades could lead to more offshore energy in U.S. 2016 [cited 2016 5 Oct].*
5. *Zayas, J., Wind Overview, in 2014 Sandia's Wind Turbine Blade Workshop. 2014, Sandia National Laboratories.*
6. *Electric, G., The GE Wind Turbine in the Block Island Wind Farm's project. . 2016, Smithsonian.com.*
7. *Jonkman, B. and J. Jonkman, FAST v8.16.00a-bjj. 2016, National Renewable Energy Laboratory.*
8. *Larsen, T.J. and A.M. Hansen, How 2 HAWC2, the user's manual. target, 2015. 2: p. 2.*
9. *Marten, D., et al., Qblade: an open source tool for design and simulation of horizontal and vertical axis wind turbines. International Journal of Emerging Technology and Advanced Engineering (IJETAE), 2013. 3: p. 264-269.*
10. *Manwell, J.F., J.G. McGowan, and A.L. Rogers, Wind energy explained : theory, design and application. 2nd ed. ed. 2009, Chichester, U.K. :: Wiley.*
11. *Møller, H. and C.S. Pedersen, Low-frequency noise from large wind turbines. The Journal of the Acoustical Society of America, 2011. 129(6): p. 3727-3744.*
12. *A C Hansen, a. and C.P. Butterfield, Aerodynamics of Horizontal-Axis Wind Turbines. Annual Review of Fluid Mechanics, 1993. 25(1): p. 115-149.*
13. *Hansen, M.O.L., et al., State of the art in wind turbine aerodynamics and aeroelasticity. Progress in Aerospace Sciences, 2006. 42(4): p. 285-330.*
14. *Kim, T., M.M. Petersen, and T.J. Larsen, A comparison study of the two-bladed partial pitch turbine during normal operation and an extreme gust conditions. Journal of Physics: Conference Series, 2014. 524(1): p. 012065.*
15. *Marten, D. and J. Wendler, QBlade Guidelines. Ver. 0.6, Technical University of (TU Berlin), Berlin, Germany, 2013.*
16. *Moriarty, P., Development and Validation of a Semi-Empirical Wind Turbine Aeroacoustic Code, in 42nd AIAA Aerospace Sciences Meeting and Exhibit. 2004, American Institute of Aeronautics and Astronautics.*
17. *Brooks, T.F., D.S. Pope, and M.A. Marcolini, Airfoil self-noise and prediction. 1989.*
18. *Lowson, M.V., et al., Assessment and prediction of wind turbine noise. 1993, [Harwell, U.K.]: Energy Technology Support Unit.*
19. *Moriarty, P., NAFNoise user's guide. National Wind Technology Center, National Renewable Energy Laboratory, 2005.*
20. *Wagner, S., R. Bareiss, and G. Guidati, Wind turbine noise. Environmental engineering; Environmental engineering (Berlin, Germany). 1996, Berlin ;: Springer.*

21. *Moriarty, P., Semi-empirical aeroacoustic noise prediction code for wind turbines [electronic resource] / P. Moriarty and P. Migliore. NREL/TP ; 500-34478, ed. P.G. Migliore and L. National Renewable Energy. 2003, Golden, Colo: National Renewable Energy Laboratory.*
22. *Zhu, W.J., et al., Modeling of Aerodynamically Generated Noise From Wind Turbines. Journal of Solar Energy Engineering, 2005. 127(4): p. 517-528.*
23. *Son, E., et al., Integrated numerical method for the prediction of wind turbine noise and the long range propagation. Current Applied Physics, 2010. 10(2, Supplement): p. S316-S319.*
24. *Kim, H., et al., Aerodynamic noise analysis of large horizontal axis wind turbines considering fluid–structure interaction. Renewable Energy, 2012. 42: p. 46-53.*
25. *Hodges, D.H., Nonlinear Composite Beam Theory. 2000, Reston, US: American Institute of Aeronautics and Astronautics.*
26. *Arakawa, C., et al., Numerical approach for noise reduction of wind turbine blade tip with earth simulator. Journal of the Earth Simulator, 2005. 2(3): p. 11-33.*
27. *Tadamasa, A. and M. Zangeneh, Numerical prediction of wind turbine noise. Renewable Energy, 2011. 36(7): p. 1902-1912.*
28. *Hand, M., et al., Unsteady aerodynamics experiment phase VI: wind tunnel test configurations and available data campaigns. National Renewable Energy Laboratory, Golden, CO, Report No. NREL/TP-500-29955, 2001.*
29. *Simms, D., et al., NREL unsteady aerodynamics experiment in the NASA-Ames wind tunnel: a comparison of predictions to measurements. National Renewable Energy Laboratory, Golden, CO, Report No. NREL/TP-500-29494, 2001.*
30. *Simms, D., et al., Plans for Testing the NREL Unsteady Aerodynamics Experiment 10m Diameter HAWT in the NASA Ames Wind Tunnel: Minutes, Conclusions, and Revised Text Matrix from the 1st Science Panel Meeting. 1999, National Renewable Energy Lab., Golden, CO (US).*
31. *Wasala, S.H., et al., Aeroacoustic noise prediction for wind turbines using Large Eddy Simulation. Journal of Wind Engineering and Industrial Aerodynamics, 2015. 145: p. 17-29.*
32. *Oerlemans, S., et al., Experimental demonstration of wind turbine noise reduction through optimized airfoil shape and trailing-edge serrations. 2001, Nationaal Lucht-en Ruimtevaartlaboratorium.*
33. *Lee, S., D. Lee, and S. Honhoff, Prediction of far-field wind turbine noise propagation with parabolic equation. The Journal of the Acoustical Society of America, 2016. 140(2): p. 767-778.*
34. *Gabriel, J., et al. Amplitude modulation and complaints about wind turbine noise. in 5th International Conference on Wind Turbine Noise. 2013.*
35. *Plovsing, B. and B. Sondergaard, Wind turbine noise propagation: Comparison of measurements and predictions by a method based on geometrical ray theory. NOISE CONTROL ENGINEERING JOURNAL, 2011. 59(1): p. 10-22.*
36. *Heimann, D., Y. Kasler, and G. Gross, The wake of a wind turbine and its influence on sound propagation. METEOROLOGISCHE ZEITSCHRIFT, 2011. 20(4): p. 449-460.*
37. *Prospathopoulos, J.M. and S.G. Voutsinas, Application of a ray theory model to the prediction of noise emissions from isolated wind turbines and wind parks. Wind Energy, 2007. 10(2): p. 103-119.*

38. *McBride, S., R. Burdisso, and J.D. Parra, An Efficient Noise Modeling Tool for Wind Turbines Including Sound Propagation in Arbitrary Weather Conditions, in 23rd International Congress on Sound and Vibration. 2016: Athens, Greece.*
39. *Jonkman J.M., G.J. Hayman, and B.J. Jonkman, AeroDyn v15 User's Guide and Theory Manual. 2016, National Renewable Energy Laboratory.*
40. *McBride, S. and R. Burdisso, A Comprehensive Hamiltonian Ray Tracing Technique for Wind*

Turbine Noise Propagation Under Arbitrary Weather Conditions, in 7th International Conference on Wind Turbine Noise. 2017: Rotterdam, Netherlands.

41. *Moriarty., P.J. and A.C. Hansen, AeroDyn Theory Manual. 2005, National Renewable Energy Laboratory: Golden, CO, USA.*
42. *Ning, S.A., et al. Development and Validation of a New Blade Element Momentum Skewed-Wake Model within AeroDyn. in AIAA Science and Technology Forum and Exposition. 2015.*
43. *Jonkman, J.M. and M.L. Buhl Jr, FAST user's guide. National Renewable Energy Laboratory, Golden, CO, Technical Report No. NREL/EL-500-38230, 2005.*
44. *Jonkman, J. BeamDyn: Convert Wiener-Milenkovic to rotation matrix. 2016; Available from: https://wind.nrel.gov/forum/wind/viewtopic.php?f=4&t=1564.*
45. *Platt Andy, Jonkman Bonnie, and J. Jason, InflowWind User's Guide. 2016, National Wind Technology Center.*
46. *Jonkman, J. and L. Kilcher, TurbSim User's Guide: Version 1.06. 00. 2012, National Renewable Energy Laboratory.*
47. *Glauert, H., Airplane Propellers, in Aerodynamic Theory: A General Review of Progress Under a Grant of the Guggenheim Fund for the Promotion of Aeronautics. 1935, Springer Berlin Heidelberg: Berlin, Heidelberg. p. 169-360.*
48. *Ning, S.A., A simple solution method for the blade element momentum equations with guaranteed convergence. Wind Energy, 2014. 17(9): p. 1327-1345.*
49. *Hansen, C., AirfoilPrep: an Excel workbook for generating airfoil tables for AeroDyn and WT_Perf. 2014.*
50. *Wang, Q., et al., BeamDyn User's Guide and Theory Manual. 2016: National Renewable Energy Laboratory.*
51. *Wang, Q., M.A. Sprague, and J.M. Jonkman, Nonlinear Legendre Spectral Finite Elements for Wind Turbine Blade Dynamics, in 32nd ASME Wind Energy Symposium. 2014, American Institute of Aeronautics and Astronautics.*
52. *Wang, Q., et al., BeamDyn: A High-Fidelity Wind Turbine Blade Solver in the FAST Modular Framework, in 33rd Wind Energy Symposium. 2015, American Institute of Aeronautics and Astronautics.*
53. *Wang, Q., M.A. Sprague, and J.M. Jonkman, Partitioned nonlinear structural analysis of wind turbines using BeamDyn, in 34th Wind Energy Symposium. 2016, American Institute of Aeronautics and Astronautics.*
54. *Jonkman, J., et al., Definition of a 5-MW reference wind turbine for offshore system development [electronic resource] / J. Jonkman ...[et al.]. NREL/TP ; 500-38060., ed. J.M. Jonkman and L. National Renewable Energy. 2009, Golden, Colo: National Renewable Energy Laboratory.*
55. *Branner, K., et al., Anisotropic beam model for analysis and design of passive controlled wind turbine blades. 2012, DTU Wind Energy.*

56. *Malcolm, D.J. and D.L. Laird, Extraction of equivalent beam properties from blade models. Wind Energy, 2007. 10(2): p. 135-157.*
57. *Drela, M. and H. Youngren, XFOIL 6.94 User Guide. 2001, Massachusetts Institute of Technology: Cambridge, Massachusetts.*
58. *Devenport, W., et al., Aeroacoustic Testing of Wind Turbine Airfoils. 2010.*
59. *Migliore, P. and S. Oerlemans. Wind tunnel aeroacoustic tests of six airfoils for use on small wind turbines. in 42nd AIAA Aerospace Sciences Meeting and Exhibit. 2004.*
60. *Burley, C. and D.S. Pope, APET User Guide. February 11, 2014.*
61. *Page, J., et al., Advanced Acoustic Model Technical Reference and User Manual. May 2009.*
62. *Lighthill, M.J.S., Waves in fluids. 1978, New York;Cambridge [Eng.];: Cambridge University Press.*
63. *Griffith, D.T. and T.D. Ashwill, The Sandia 100-meter all-glass baseline wind turbine blade: SNL100-00. Sandia National Laboratories, Albuquerque, Report No. SAND2011-3779, 2011.*
64. *Hendriks, H., et al. Application of an advanced cost model in the different design phases of an offshore wind turbine. in European Wind Energy Conference (EWEC 2001), Copenhagen (Denmark). 2001.*
65. *Kooijman, H., et al., DOWEC 6 MW Pre-Design: Aero-elastic modeling of the DOWEC 6 MW pre-design in PHATAS. Energy Research Center of the Netherlands, Technical Report No. DOWEC 10046_009, 2003.*
66. *Resor, B.R., Definition of a 5MW/61.5 m wind turbine blade reference model. Albuquerque, New Mexico, USA, Sandia National Laboratories, SAND2013-2569 2013, 2013.*
67. *Griffith, D.T., The SNL100-01 blade: carbon design studies for the Sandia 100-meter blade. Sandia National Laboratories Technical Report, SAND2013-1178, 2011.*
68. *Commission, I.E., IEC 61400-1: Wind Turbine Generator Systems-Part 1: Safety Requirements. International Standard, 1999: p. 1400-1.*
69. *Lloyd, G. and G. Hamburg, Guideline for the certification of wind turbines. July 1st, 2010.*
70. *Bir, G.S., User's guide to BModes (Software for computing rotating beam coupled modes). 2007: National Renewable Energy Laboratory Golden, CO.*
71. *Xiong, L., et al., Dynamic response analysis of the rotating blade of horizontal axis wind turbine. Wind Engineering, 2010. 34(5): p. 543-559.*
72. *Kim, S.-W., et al., Structural performance tests of down scaled composite wind turbine blade using embedded fiber Bragg grating sensors. International Journal Aeronautical and Space Sciences, 2011. 12(4): p. 346-353.*
73. *Griffith, D.T., B.R. Resor, and T.D. Ashwill. Challenges and opportunities in large offshore rotor development: Sandia 100-meter blade research. in AWEA WINDPOWER 2012 Conference and Exhibition. 2012.*
74. *Griffith, D.T., The SNL100-02 Blade: Advanced Core Material Design Studies for the Sandia 100-meter Blade. Sandia National Laboratories Technical Report, SAND2013-10162, 2013.*
75. *Berry, D.S. and D. Berg, Blade system design studies phase II: final project report. Sandia Report SAND2008-4648, 2008.*
76. *Griffith, D.T. and P.W. Richards, Investigating the effects of flatback airfoils and blade slenderness on the design of large wind turbine blades. European Wind Energy Association, 2014: p. 1-8.*

77. *Slawsky, L.M., et al., Observed thermal impacts of wind farms over northern illinois. Sensors, 2015. 15(7): p. 14981-15005.*
78. *Wilson, R.E., P.B. Lissaman, and S.N. Walker, Aerodynamic performance of wind turbines. Final report. 1976, Oregon State Univ., Corvallis (USA). Dept. of Mechanical Engineering.*
79. *Hansen, M.O.L., Aerodynamics of wind turbines. 2015, New York, NY: Routledge.*
80. *de Vries, O., Fluid Dynamic Aspects of Wind Energy Conversion. NTIS Report Ad-A076 315, 1979.*
81. *Buhl, M.L., Jr., New Empirical Relationship between Thrust Coefficient and Induction Factor for the Turbulent Windmill State. 2005, ; National Renewable Energy Laboratory (NREL), Golden, CO. p. Medium: ED; Size: 12 pp.*
82. *Bauchau, O.A., Flexible Multibody Dynamics. 2011: Springer Netherlands.*
83. *Yu, W. and M. Blair, GEBT: A general-purpose nonlinear analysis tool for composite beams. Composite Structures, 2012. 94(9): p. 2677-2689.*
84. *Chung, J. and G.M. Hulbert, A Time Integration Algorithm for Structural Dynamics With Improved Numerical Dissipation: The Generalized-α Method. Journal of Applied Mechanics, 1993. 60(2): p. 371-375.*
85. *Amiet, R.K., Acoustic radiation from an airfoil in a turbulent stream. Journal of Sound and Vibration, 1975. 41(4): p. 407-420.*
86. *Yildiz, M., On the Diffraction of Multipole Fields by a Semi-Infinite Rigid Wedge. The Journal of the Acoustical Society of America, 1960. 32(12): p. 1685.*
87. *Meecham, W.C., Diffraction of dipole sound by the edge of a rigid baffle. The Journal of the Acoustical Society of America, 1981. 70(5): p. 1531.*

Appendix A: Classical BEM and AeroDyn v15

This section presents the classical BEM formulation and the BEM solving algorithm in the AeroDyn.

Classical BEM and solving algorithm

BEM is a combination of Momentum theory and Blade element theory, so it is necessary to understand these two theories. First, momentum theory is explained and followed by blade element theory.

The following reviews momentum theory without rotation effect, and then extended to wake rotation. The one-dimensional momentum theory assumes that the loss of pressure or momentum in a rotor plane is caused by the work done by the airflow passing through the rotor plan. It implies a control volume analysis of the forces at the blade based on the conservation of linear and angular momentum as shown in Figure 91. This analysis follows two key assumptions: (1) no frictional drag (2) no rotational velocity component in the wake.

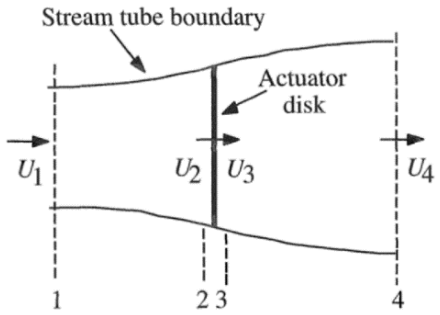

Figure 91: Momentum theory actuator disc model; *U*, air velocity; 1, 2, 3, and 4indiciate locations [10].

From the conversation of linear momentum of this control volume, the thrust, *T*, is equal and opposite to rate of change of momentum of the air stream:

$$T = U_1(\rho AU)_1 - U_4(\rho AU)_4 = \dot{m}(U_1 - U_4) \tag{17}$$

Note that thrust is positive when $U_1 > U_4$, which indicates the rotor generates thrust. Thrust can be also expressed as the net sum of forces from pressure drop over the rotor and that is:

$$T = A_2 \Delta p = A_2 (p_2 - p_3) \tag{18}$$

Since there is no work done on either side of the rotor (no external force acts on the up- or downstream of the rotor), Bernoulli equation is valid and used in both side of the actuator disc. The upstream of the disc is:

$$p_1 + \frac{1}{2}\rho U_1^2 = p_2 + \frac{1}{2}\rho U_2^2 \tag{19}$$

The downstream of the disc is:

$$p_3 + \frac{1}{2}\rho U_3^2 = p_4 + \frac{1}{2}\rho U_4^2 \tag{20}$$

It is assumed that far upstream and far downstream pressures are equal ($p_1 = p_4$) and that velocity across the disc remains the same ($U_2 = U_3$). By solving $(p_2 - p_3)$ using Equations (19) and (20) and substitutes into Equation (18), it yields,

$$T = \frac{1}{2}\rho A_2 (U_1^2 - U_4^2) \tag{21}$$

Since Equation (18) and (21) equal to each other, and the mass flow rate is also $\rho A_2 U_2$, then air velocity at location 2 becomes,

$$U_2 = \frac{U_1 - U_4}{2} \tag{22}$$

Define the axial induction factor, *a*, as the fractional decrease in wind velocity between the freestream and the rotor plan as,

$$a = \frac{U_1 - U_2}{U_1} \tag{23}$$

$$U_2 = U_1(1-a) \tag{24}$$

Rearrange Equation (22) and (24), the air velocity at far downstream becomes,

$$U_4 = U_1(1-2a) \tag{25}$$

The axial thrust of an ideal rotor without rotation wake then can be derived from Equation (21), (24), and (25). Notes that $U = U_1$, is the freestream air velocity.

$$T = \frac{1}{2}\rho A U^2 \left[4a(1-a)\right] \tag{26}$$

$$C_T = \frac{T}{\frac{1}{2}\rho A U^2} = \frac{\text{Thrust force}}{\text{Dynamic force}} \tag{27}$$

Previous analysis uses linear momentum theory without rotation imparted to the flow. Now, it is extended to consider rotating rotor generates angular momentum, which related to rotor toque.

This analysis is based on the use of an annular stream tube with a radius, *r*, and a thickness, d*r*, with a cross-sectional area equals to, $2\pi r\mathrm{d}r$, as Figure 92 shows. The pressure, wake rotation, and inductions factors become functions of radius. Under the assumption that angular velocity imparted to the flow stream, ω , is small compared to the angular velocity, Ω, of the rotor, the pressure in the far wake (location 4) is equal to the pressure in the free stream [78].

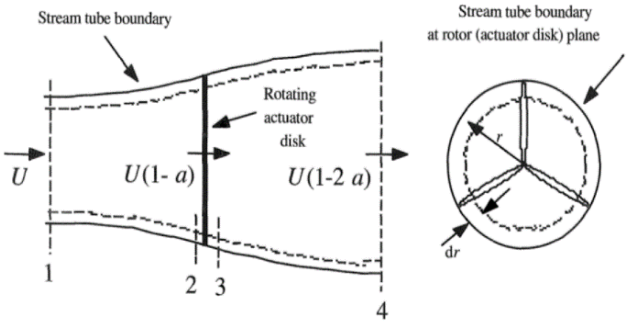

Figure 92: Schematic of the momentum theory with wake rotation [10].

The energy equation is applied in the sections before and after the blades to derive an expression for the pressure difference across the blades as a control volume moves with the angular velocity of the blade. The angular velocity of the flow relative to the blade increase from Ω (at location 2) to $\Omega+\omega$ while axial component of the velocity remains constant. The result of pressure difference between location 2 and 3 is [47]

$$p_2 - p_3 = \rho(\Omega + \frac{1}{2}\omega)\omega r^2 \tag{28}$$

Thrust on an annular element, *dT*, becomes,

$$dT = (p_2 - p_3)dA = \left[\rho(\Omega + \frac{1}{2}\omega)\omega r^2\right] 2\pi r dr \tag{29}$$

Define angular induction factor, $a' = \omega/2\Omega$, and rearrange Equation (29). The thrust expression becomes,

$$dT = 4a'(1+a')\frac{1}{2}\rho\Omega^2 r^2 2\pi r dr \tag{30}$$

Or using Equation (26) to express thrust on the annular element with axial induction factor, *a*

$$dT = 4\pi r\rho U^2 a(1-a)dr \tag{31}$$

The torque exerted on the rotor, *Q*, can be derive by applying the conservation of angular momentum which is that the torque must equal to the change in the angular momentum of the wake. The torque on each annular element is,

$$dQ = d\dot{m}(\omega r)(r) = \left(\rho U_2 2\pi r dr\right)\left(\omega r\right)\left(r\right) \tag{32}$$

Note that $\dot{m}$ equals $\rho A_2 U_2$, where A_2 is $2\pi r dr$. Using definitions of U_2 and a', Equation (32) is reduced to,

$$dQ = 4\pi r^3 \rho U \Omega (1-a) a' dr \tag{33}$$

The following section explains the blade element theory that assumes blades can be divided into small elements that act independently from other elements as shown in Figure 93. Each element operates aerodynamically as 2D airfoils whose aerodynamic forces can be calculated based on the local flow condition .To summarize these key assumption:

- No aerodynamic interaction between elements
- Forces on blades are determined from lift and drag characteristics of the airfoil geometry.

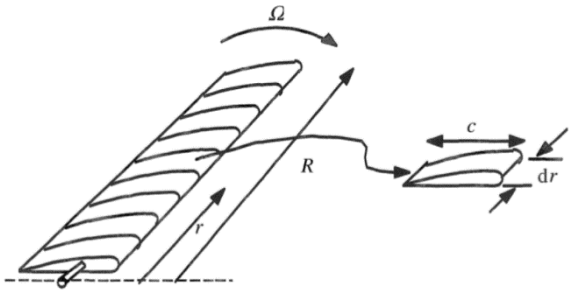

Figure 93: Blade elements; c, airfoil chord length; *dr*, riadial lenght of element, *r*, radius; *R*, rotor radius; Ω, angular velocity of rotor [10].

To analyze the forces on the blade section, lift and drag forces on the airfoils are perpendicular and parallel to the relative wind. The vector of relative wind is the sum of the wind velocity at the rotor $U(1-a)$, and the wind velocity due to the rotation. The rotational component vector is sum of the blade section velocity, Ωr, and the induced angular velocity at blade from conservation of angular momentum [10], $\omega r/2$,

$$\Omega r + (\omega/2)r = \Omega r + \Omega a' r = \Omega r(1+a') \tag{34}$$

Once the relative wind vector is determined, a 2D force analysis on one of elements can be constructed as Figure 94 shows.

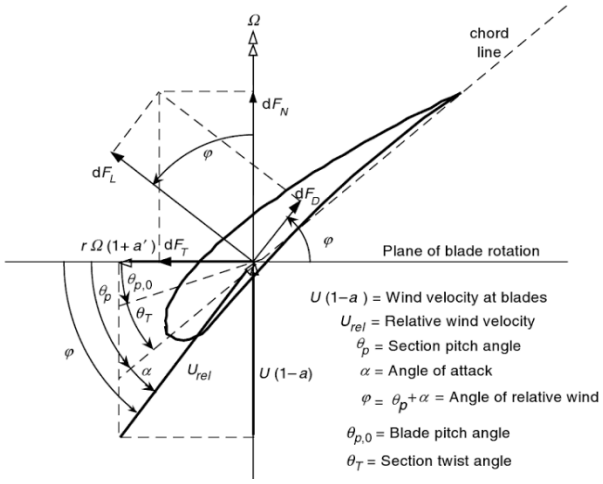

Figure 94: Sectional blade geometry analysis of a wind turbine rotor [10].

Based on Figure 94, the following relationships are determined:

$$\varphi = \theta_p + \alpha \tag{35}$$

$$\tan\varphi = \frac{U(1-a)}{\Omega r(1-a')} = \frac{1-a}{(1-a')\lambda_r} \tag{36}$$

$$U_{rel} = U(1-a)/\sin\varphi \tag{37}$$

$$dF_L = C_l \frac{1}{2}\rho U_{rel}^2 c dr \tag{38}$$

$$dF_D = C_D \frac{1}{2}\rho U_{rel}^2 c dr \tag{39}$$

$$dF_N = dF_L\cos\varphi + dF_D\sin\varphi \tag{40}$$

$$dF_T = dF_L\cos\varphi - dF_D\sin\varphi \tag{41}$$

The rotor has *B* blades and the forces on the section at a distance, *r*, from the center is:

$$dF_T = B\frac{1}{2}\rho U_{rel}^2(C_l\cos\varphi + C_d\sin\varphi)cdr = B\frac{1}{2}\rho U_{rel}^2 C_n c dr \tag{42}$$

Where $C_n = C_l\cos\varphi + C_d\sin\varphi$ and the normal force, dF_T, is the same as the thrust, dT. The torque due to the tangential force is,

$$dQ = BrdF_T = B\frac{1}{2}\rho U_{rel}^2 (C_l \cos\varphi - C_d \sin\varphi) crdr = B\frac{1}{2}\rho U_{rel}^2 C_t crdr \quad (43)$$

where $C_t = C_l \cos\varphi - C_d \sin\varphi$. Rearrange Equation (42) and (43) using Equation (37), they become,

$$dT = \sigma' \pi \rho \frac{U^2 (1-a)^2}{\sin^2 \varphi} C_n r dr \quad (44)$$

$$dQ = \sigma' \pi \rho \frac{U(1-a)\Omega r(1-a')}{\sin\varphi \cos\varphi} C_t r^2 dr \quad (45)$$

where σ' is the local solidity, defined as $\sigma' = Bc/2\pi r$.

The following section explain BEM theory which is the fundamental part of AeroDyn. The most important equations of BEM are Equation (31), (33) from the momentum theory and Equation (44), (45) from the blade element theory. By equaling thrust equations, Equation (31) and (44), from the momentum theory and blade element theory, the axial induction factor *a* is obtained as:

$$a = 1/\left(4\sin^2 \varphi / \sigma' C_n + 1\right) \quad (46)$$

Then equalize Equation (33) and (45) to obtain the tangential induction factor, a' , as:

$$a' = 1/\left(4\sin\varphi\cos\varphi / \sigma' C_n - 1\right) \quad (47)$$

Since all the necessary equation for the BEM model have been derived, the iterative solution algorithm for induction factors can be summarized below. Each element can be calculated independently and the solution can be found before solving for other blade elements [79].

1. Guess initial *a* and a' . Typically $a = a' = 0$.
2. Compute the flow angle, φ , from Equation (36)
3. Compute the local angle of attack, α , from Equation (35)
4. Using the local angle of attack to determine C_l and C_d from airfoil data
5. Compute C_n and C_t
6. Calculation *a* and a' from Equation (46) and (47)

7. If the change of *a* and a' more than a certain tolerance, go back to Step 2 or else finish.
8. Compute the local loads on the segment of the blades

Two corrections must be applied to obtain good result from BEM, and they are Prandtl's tip loss factor [80] and Glauert empirical correction derived by Buhl [81]. Prandtl's tip loss factor corrections the assumption of an infinite number of blade from BEM. It is due to the vortex system in the wake is different from a rotor with an infinite number of blades (assumption from the momentum theory) than a rotor with a finite number of blades. Prandtl derived a correction factor *F* to Equation (31) and (33), and yielded,

$$dT = 4\pi r \rho U^2 a(1-a)Fdr \tag{48}$$

$$dQ = 4\pi r^3 \rho U^2 \Omega(1-a)a'Fdr \tag{49}$$

where $F = \frac{2}{\pi}\cos^{-1}(e^{-f})$ and $f = \frac{B}{2}\frac{R-r}{r\sin\varphi}$. Equation (48) and (49) replace Equation (31) and (33) in derivation of *a* and a'. Then expressions of induction factors become,

$$a = \frac{1}{\frac{4F\sin^2\varphi}{\sigma' C_n} + 1} \tag{50}$$

$$a' = \frac{1}{\frac{4F\sin\varphi\cos\varphi}{\sigma' C_t} - 1} \tag{51}$$

Equation (50) and (51) replace Equation (46) and (47) in Step 6 of the BEM algorithm and an extra step after Step 2 to compute Prandtl's tip loss factor, *F*. The derivation of Prandtl's tip loss factor is complicated and out of scope of this study, but a detailed explanation can be found in [47].

The second correction is the Glauert empirical correction for induction factor, a, greater than 0.4. The momentum theory becomes invalid at this high value of induction factor because the flow patterns through the wind turbine becomes more complex than predictions from the momentum theory as shown in Figure 95.

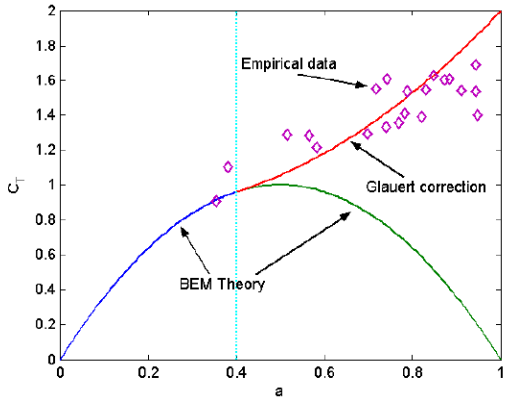

Figure 95: Glauert empirical correction with Prandtl's correction, F = 1.0 [41].

Buhl (2004) derived a modification to the Glauert empirical relation that includes the Prandtl's correction,

$$C_T = \frac{8}{9} + (4F - \frac{40}{9})a + (\frac{50}{9} - 4F)a^2 \tag{52}$$

Rearrange the equation to solve the induction factor,

$$a = \frac{18F - 20 - 3\sqrt{C_T(50 - 36F) + 12F(3F - 4)}}{36F - 50} \tag{53}$$

If $a > 0.4$, Equation (53) replaces Equation (46) in Step 7 of the BEM algorithm.

AeroDyn BEM solving algorithm

An overview of Ning's algorithm is the following:

1. Specify the local inflow angle
2. Computed the local angle of attack from Equation (35)
3. Estimate the lift and drag coefficient from airfoil data
4. Compute normal and tangential force coefficients, C_n and C_t
5. Compute the induction factors, a and a'
6. Check the error in the governing equation
7. Try another value of the local inflow angle until the residual approaches zeros (using a root-finding method).

The key reason is that induction factors always require specifying the inflow condition, but simplification in this procedure is possible by making the local inflow angle and magnitude unknown. Since lift and drag coefficients are also functions of the local inflow angle, they can be updated without any knowledge of the induction factors.

Based on Equation (44), the local thrust coefficient predicted by blade element theory is,

$$C_T = \left(\frac{1-a}{\sin\varphi} \right)^2 C_n \sigma' \tag{54}$$

The local thrust coefficient from the momentum theory with Prandtl's correction is,

$$C_T = 4a(1-a) \tag{55}$$

Ning equates the local thrust coefficients of an annular element from two theory, Equation (54) and (55), to solve axial induction factor as function of inflow angle.

$$a(\varphi) = \frac{\kappa(\varphi)}{1+\kappa} \tag{56}$$

where κ is defined as,

$$\kappa(\varphi) \equiv \frac{\sigma' C_n(\varphi)}{4F(\varphi)\sin^2\varphi} \tag{57}$$

Applying Buhl's correction on the local thrust coefficient, Equation (52) for axial inductor factor, $a > 0.4$, the axial induction factor can be express as,

$$a(\varphi) = \frac{\kappa(\varphi)}{\kappa(\varphi)-1} \tag{58}$$

The tangential induction factor follows the similar procedure by equating torque equation from the momentum theory and blade element theory and yields,

$$a'(\varphi) = \frac{\kappa'(\varphi)}{1-\kappa'(\varphi)} \tag{59}$$

where κ' is defined as,

$$\kappa'(\varphi) \equiv \frac{\sigma' C_t}{4F \sin\varphi \cos\varphi} \tag{60}$$

Since the inductions factors become functions of the local inflow angle, φ , relationship between three variable, φ , ▯,and a' can be related based on Equation (36). Ning suggests to form a residual function so singularities occur at the predefined location ($\varphi = 0, \pm\pi$), and that is,

$$f(\varphi) = \frac{\sin\varphi}{1-a} - \frac{\cos\varphi}{\lambda_r(1+a')} = 0 \tag{61}$$

Ning's work reduced the solution approach of the BEM equation from a 2D fixed-point algorithm to 1D root-finding algorithm. The detailed derivation of Ning's work is out of scope of this study, but a completed description can be found in [48].

Once the induction factors are determined from above approach using BEM, the angle of attack, the inflow angle (computed from Equation (35) and (36)), the lift coefficient, and the drag coefficients (determined based on the airfoil data using the angle of attack) are the necessary inputs for the noise model.

Appendix B: *BeamDyn* GEBT Theories

This section explains BeamDyn theory and has three topics: GEBT governing equations, numerical implementation with LSFE, and generalized-α time integrator. The intentions is to briefly explain the mathematics of each theories. Details derivation and formulation can be found in [25, 52, 82, 83].

The full derivations and formulations of GEBT and cross-sectional analysis are long and complex. As shown in Figure 96, a beam analysis using GEBT first requires formulations of the governing equations that are based on the concept of decomposition of the rotation tensor (DRT) and a beam cross-sectional analysis, such as VABS (variational-asymptotic beam sectional analysis developed by Hodges [25]), to compute the sectional properties. These sectional properties and the loads are inputs of the 1D GEBT beam model to compute the resultant 3D sectional displacements and responses using the recovery relations. The formulation of GEBT is not within the scope of this study. Therefore, the following sections only review the governing equations of GEBT and the implementation of LSFEs. It first explains the kinematic of a beam and then the GEBT governing equations. Finally, the numerical implementation with Legendre spectral finite elements is covered.

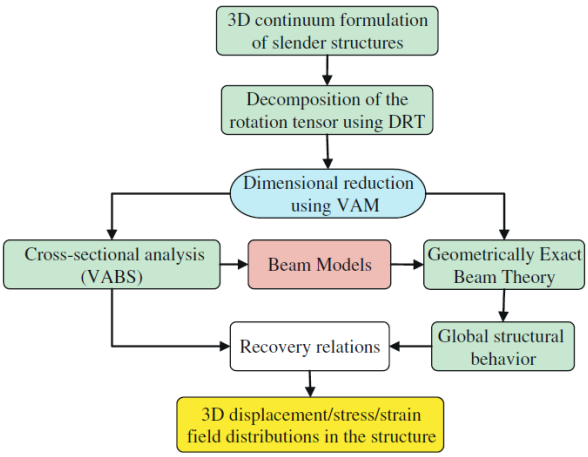

Figure 96: GEBT schematics; DRT is the rotation tensor; VAM is a mathematical method for asymptotical analysis of the governing variation statement. VABS is a cross-sectional analysis code developed by Hodges [83].

The kinematic of a beam follows Hodges's work [25]. The curvilinear coordinate x_1 defines the beam reference line, ***r***, e.g. beam axis. A point on the undeformed beam reference line is located by the position vector ***r(x₁)***. At each point along ***r*** has a frame $\boldsymbol{b}_i$ with unit vector $\boldsymbol{b}_2(x_1)$ and $\boldsymbol{b}_3(x_1)$ that are tangent to the coordinate curves x_2 and x_3 at ***r***, and $\boldsymbol{b}_1$ is tangent to ***r***. Each value of x_1 specifies not only a point on ***r,*** but also a reference cross-section at that point as the dark grey area shown in Figure 97. The position vector is defined as $\xi = x_2 b_2 + x_3 b_3 = x_\alpha b_\alpha$ for an arbitrary point within a particular cross-section relative to the point in that cross-section, in where ***r*** intersected. A particle of the beam located from a fixed point is defined by the position vector $\hat{\mathrm{r}}(x_1, x_2, x_3) = \mathrm{r} + x_\alpha b_\alpha = \mathrm{r} + \xi$. The curvilinear coordinate ***S*** defines the deformed beam line, ***R***. The locus of points belonging to the initially plane reference cross-section of the undeformed beam has undergone a rigid-body translation and rotation. The rigid body translation is along the vector $u(x_1^*)$, which is the position vector from the point on undeformed beam reference line at $x_1 = x_1^*$, to the point on the deformed beam reference line at $s = s(x_1^*)$. At each point along ***R*** exists a frame $\boldsymbol{B}_i$ with $\boldsymbol{B}_1(x_1^*)$ normal to the cross-section plane and $\boldsymbol{B}_\alpha(x_1^*)$ laying in it. However, $\boldsymbol{B}_2(x_1^*)$ and $\boldsymbol{B}_3(x_1^*)$ are not necessarily tangent to ***R***. The notation $\underline{\bullet}$ denotes a vector, $\bar{\bullet}$ denotes unit vector, and $\underline{\underline{\bullet}}$ denotes a tensor in the following analysis.

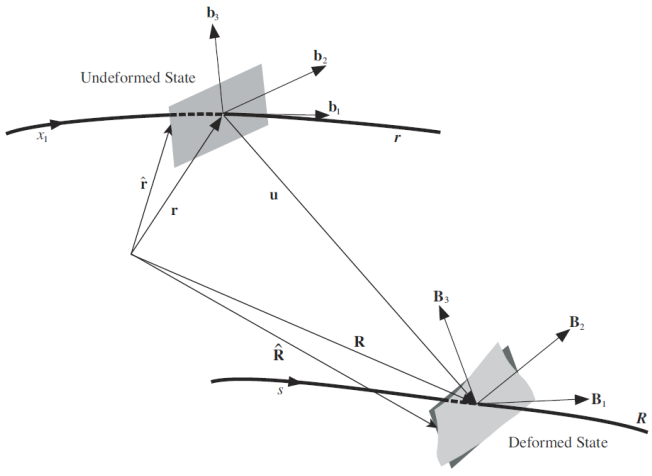

Figure 97: Beam in undeformed and deformed state [25].

Through matrix formulation, principle of virtual work, and variation of the kinetic energy, Bauchau derives the governing equations of motion for geometrically exact beam theory as (See Appendix B for derivation of the GEBT equations of motion.),

$$\dot{\underline{h}} - \underline{F}' = \underline{f} \tag{62}$$

$$\dot{\underline{g}} - \tilde{\dot{u}}\underline{h} - \underline{M}' + (\tilde{x}_0' + \tilde{u}_0')^T \underline{F} = \underline{m} \tag{63}$$

where $\underline{h}$ and $\underline{g}$ are linear and angular momenta resolved in the inertial coordinate system, respectively; $\underline{F}$ and $\underline{M}$ are the beam sectional force and moment resultants, respectively. $\underline{u}$ is 1D displacement of a point on the reference line; $\underline{x}_0$ is the positon vector of a point along the beam reference line; $\underline{f}$ and $\underline{m}$ are the distributed force and moment applied to the beam structure. The notation $(\bullet)'$ indicate a derivative with respect to beam axis x_1 and $(\dot{\bullet})$ indicate a derivative with respect to time. The tilde operator $(\tilde{\bullet})$ is a skew-symmetric tensor to a vector,

$$\tilde{n} = \begin{bmatrix} 0 & -n_3 & n_2 \\ n_3 & 0 & -n_1 \\ -n_2 & n_1 & 0 \end{bmatrix}$$

The constitutive equations relate the velocities to the momenta and the 1D strain measure to the sectional resultant as,

$$\begin{Bmatrix} \underline{h} \\ \underline{g} \end{Bmatrix} = \underline{\underline{\mathcal{M}}} \begin{Bmatrix} \dot{\underline{u}} \\ \underline{\omega} \end{Bmatrix} \tag{64}$$

$$\begin{Bmatrix} \underline{F} \\ \underline{M} \end{Bmatrix} = \underline{\underline{C}} \begin{Bmatrix} \underline{\varepsilon} \\ \underline{\kappa} \end{Bmatrix} \tag{65}$$

where $\underline{\underline{\mathcal{M}}}$ and $\underline{\underline{C}}$ are the 6×6 sectional mass and stiffness matrices, respectively. These sectional beam properties are the byproduct of 2D analysis over the beam cross-section. However, the cross-sectional analysis is out of scope of this study. More details can be found from [25]. The $\underline{\varepsilon}$ and $\underline{\kappa}$ are the 1D strain and curvature, respectively. $\underline{\omega}$ is the angular velocity vector that is defined by

the rotation tensor $\underline{\underline{R}}$ as $\underline{\omega} = axial\left(\dot{\underline{\underline{R}}}\underline{\underline{R}}^T\right)$. The axial vector $\underline{a}$ associated with a second-order $\underline{\underline{A}}$ is denoted $\underline{a} = axial(\underline{\underline{A}})$ and its components are defined as,

$$\underline{a} = axial(\underline{\underline{A}}) = \begin{Bmatrix} a_1 \\ a_2 \\ a_3 \end{Bmatrix} = \frac{1}{2}\begin{Bmatrix} A_{32} - A_{23} \\ A_{13} - A_{31} \\ A_{21} - A_{12} \end{Bmatrix}$$

The 1D strain measure is defined as,

$$\begin{Bmatrix} \underline{\varepsilon} \\ \underline{\kappa} \end{Bmatrix} = \begin{Bmatrix} \underline{x}_0' + \underline{u}' - \left(\underline{\underline{R}}\underline{\underline{R}}_0\right)\underline{\bar{i}}_1 \\ \underline{k} \end{Bmatrix} \tag{66}$$

A full mathematical description of elasticity beam is provided through Equations (62), (63), (64), (65) and (66). Bauchau presents full details on the formulation and derivation in [82].

For a displacement-based finite element implementation, there are six DoFs at each node (three translational and three rotational). The elemental displacement is defined as $\underline{q} = \begin{bmatrix} \underline{u}^T & \underline{p}^T \end{bmatrix}$ where $\underline{u}$ is the displacement and $\underline{p}$ is the rotation-parameter vector. The acceleration array is defined as $\underline{a} = \begin{bmatrix} \underline{u}^T & \dot{\underline{\omega}}^T \end{bmatrix}$. The discretized and incremental forms of displacement velocity and acceleration for a nonlinear finite-element analysis are,

$$\underline{q}(x_1) = \underline{\underline{N}}\hat{\underline{q}} \quad \Delta\underline{q}^T = \begin{bmatrix} \Delta\underline{u}^T & \Delta\underline{p}^T \end{bmatrix} \tag{67}$$

$$\underline{v}(x_1) = \underline{\underline{N}}\hat{\underline{v}} \quad \Delta\underline{v}^T = \begin{bmatrix} \Delta\dot{\underline{u}}^T & \Delta\underline{\omega}^T \end{bmatrix} \tag{68}$$

$$\underline{a}(x_1) = \underline{\underline{N}}\hat{\underline{a}} \quad \Delta\underline{a}^T = \begin{bmatrix} \Delta\ddot{\underline{u}}^T & \Delta\dot{\underline{\omega}}^T \end{bmatrix} \tag{69}$$

where $\underline{\underline{N}}$ is the shape function matrix and $\hat{(\bullet)}$ denotes a column matrix of nodal values. The displacement filed in an element are approximated as,

$$\underline{u}(s) = h^k(s)\hat{\underline{u}}^k \tag{70}$$

$$\underline{u}'(s) = h^{k\prime}(s)\hat{\underline{u}}^k \tag{71}$$

Where $h^k(s)$, the component of shape function matrix $\underline{\underline{N}}$, is the p^{th}-order polynomial Lagrangian-interpolant shape function of k ($k = \{1, 2, ..., p+1\}$), $\underline{\hat{u}}^k$ is the k^{th} nodal valuie, and $\underline{s}$ is the element natural coordinates. Due to the errors in BeamDyn rotational displacement outputs, the 3D rotational field are not presented here. More detail can be found in [51, 52, 82]. In LSFE approach, the shape functions are p^{th}-order Lagrangian interpolants, where nodes are located at the $p+1$ Gauss-Lobatto-Legendre points as Figure 98 shows.

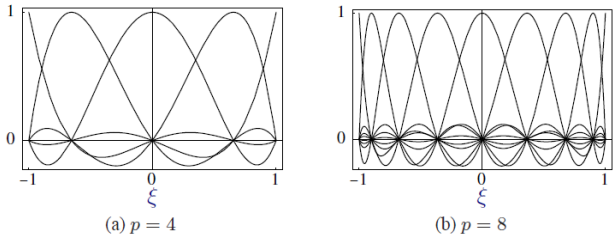

Figure 98: Representative p+1Lagranigant shape functions in the element natural coordinates for **(a)** fourth- and **(b)** eight-order LSFEs, where nodes are located at the Gauss-Lobatto-Legendre points [51].

The nonlinear governing Equations (62) and (63) are linearized and solved by the Newton-Raphson method. Time integration is performed using the generalized-α scheme which is second-order accurate and unconditionally stable for linear structural dynamics problems [84].

In summary, BeamDyn is based on the state-space form of GEBT using time integrators for first-order form ODEs. Implementation of LSFEs provides exponential convergence rates. Many validations on cantilevered beam and actual rotor blades have been done in references and yielded good results in [51, 52].

GEBT governing equations

Figure 99 shows an initially curved and twisted beam of length *L*, with an arbitrary cross section shape and area, *A*. The dashed line in the figure is the beam reference line. Curvilinear coordinate α_1 defines the intrinsic parameterization of this line (it measures the length along the beam reference line). Point **B** intersected the reference line with the plane of the cross-section. Point **P** is the material point on the cross-section.

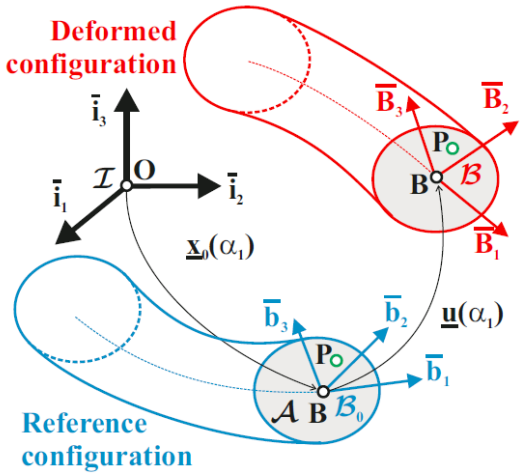

Figure 99: Schematic of a curved beam in reference and deformed configuration [82].

In the reference configuration, an orthonormal basis, $\mathcal{B}_0\ (\alpha_1) = (\bar{b}_1, \bar{b}_2, \bar{b}_3)$ is defined at point **B** ($\bar{b}_1$ is the unit tangent vector to the reference line at that point, and $\bar{b}_2$ and $\bar{b}_3$ define the cross-section plane). An inertial reference frame, $\mathrm{F}^{\mathrm{I}} = [\mathrm{O}, \mathrm{I} = (\bar{i}_1, \bar{i}_2, \bar{i}_3]$, is defined, and the components of the rotation tensor that bring basis I to $\mathcal{B}_0$ are denoted $\underline{\underline{R}}_0(\alpha_1)$. Then, Bauchau defines their position vector as $\underline{x}_0(\alpha_1)$, and $\underline{x}(\alpha_1, \alpha_2, \alpha_3) = \underline{x}_0\alpha_1 + \alpha_2\bar{b}_2 + \alpha_3\bar{b}_3$ for point B and P, respectively. α_2 and α_3 are the material coordinates along unit vector $\bar{b}_2$ and $\bar{b}_3$, respectively.

In the deformed configuration, all the points on a cross-section of the beam moved to new position, from $\mathcal{B}_0$ to $\mathcal{B}$. This motion is decomposed into a rigid body motion and a warping displacement field. The rigid body motion consists of a translation of the cross-section, characterized by displacement vector $\underline{u}(\alpha_1)$ of reference point **B**, and of a rotation of the cross-section, which brings basis $\mathcal{B}_0$ to $\mathcal{B}\ (\alpha_1) = \left(\bar{B}_1, \bar{B}_2, \bar{B}_3\right)$. The components of the rotation tensor that bring basis $\mathcal{B}_0$ to $\mathcal{B}$, resolved in basis I, are denoted $\underline{\underline{R}}(\alpha_1)$. Neglecting warping of the cross-section, the position vector point **P** in the deformed configuration becomes,

$$\underline{X}(\alpha_1, \alpha_2, \alpha_3) = \underline{X}_0 + \alpha_2\bar{B}_2 + \alpha_3\bar{B}_3 \tag{72}$$

Using the definition of deformed point **B**, $\underline{X}_0(\alpha_1) = \underline{x}_0 + \underline{u}$, and $\bar{B}_i = \underline{\underline{R}}\bar{b}_i = \left(\underline{\underline{R}}\underline{\underline{R}}_0\right)\bar{i}_i$, Equation (72) becomes,

$$\underline{X}(\alpha_1, \alpha_2, \alpha_3) = \underline{x}_0 + \underline{u} + \left(\underline{\underline{R}}\underline{\underline{R}}_0\right)\left(\alpha_2\bar{i}_2 + \alpha_3\bar{i}_3\right) \tag{73}$$

The 1D strain measure are defined as,

$$\begin{Bmatrix} \underline{\varepsilon} \\ \underline{\kappa} \end{Bmatrix} = \begin{Bmatrix} \underline{x}_0' + \underline{u}' - \left(\underline{\underline{R}}\underline{\underline{R}}_0\right)\bar{i}_1 \\ \underline{k} - \underline{\underline{R}}\underline{k}_i \end{Bmatrix} \tag{74}$$

where $\underline{k} = axial\left(\underline{\underline{R}}'\underline{\underline{R}}_0^T\right)$ are the components of the sectional curvature vector resolved in the inertial basis, $\mathcal{F}^{\mathrm{I}}$. $\underline{k}_i$ are the components of the corresponding curvature vector in the reference configuration. The notation $(\bullet)'$ indicate a derivative with respect to α_1 and $(\bullet)^*$ indicates the components of vectors and tensors resolved in the material basis, $\mathcal{B}$.

The principle of virtual work of this deformed beam states,

$$\int_0^L \left(\delta\underline{\varepsilon}^{*T}\underline{N}^* + \delta\underline{\kappa}^{*T}\underline{M}^*\right)d\alpha_1 = \delta W_{ext} \tag{75}$$

where $\underline{N}^*$ and $\underline{M}^*$ are the beam's sectional forces and moments, respectively. The sectional constitutive law relates the sectional strain measure to sectional loads is

$$\begin{Bmatrix} \underline{N}^* \\ \underline{M}^* \end{Bmatrix} = \underline{\underline{C}}^* \begin{Bmatrix} \underline{\varepsilon}^* \\ \underline{\kappa}^* \end{Bmatrix} \Rightarrow \begin{Bmatrix} \underline{N} \\ \underline{M} \end{Bmatrix} = \underline{\underline{C}} \begin{Bmatrix} \underline{\varepsilon} \\ \underline{\kappa} \end{Bmatrix} = \left(\underline{\underline{\mathcal{R}}}\underline{\underline{\mathcal{R}}}_0\right)\underline{\underline{C}}^* \begin{Bmatrix} \underline{\varepsilon}^* \\ \underline{\kappa}^* \end{Bmatrix} \tag{76}$$

Where C is the 6×6 sectional stiffness matrices, one of the byproducts of 2D analysis over the beam cross-section.

Using Equation (74), the variations in strain components are expressed as,

$$\delta\underline{\varepsilon}^* = \left(\underline{\underline{R}}\underline{\underline{R}}_0\right)^T\left[\delta\underline{u}' + (\tilde{x}_0' + \tilde{u}')\delta\underline{\psi}\right], \tag{77}$$

$$\delta\underline{\kappa}^* = \left(\underline{\underline{R}}\underline{\underline{R}}_0\right)^T\delta\underline{\psi}' \tag{78}$$

where $\delta\underline{\psi} = axial(\delta\underline{\underline{R}}\underline{\underline{R}}^T)$ is the virtual rotation vector. The principle of virtual work then becomes,

$$\int_0^L \left(\left[\delta \underline{u}'^T + \delta \underline{\psi}^T (\tilde{x}_0' + \tilde{u}')^T \right] \underline{N} + \delta \underline{\psi}'^T \underline{M} \right) d\alpha_1 = \delta W_{ext} \tag{79}$$

where $\underline{N} = \left(\underline{\underline{R}} \underline{\underline{R}}_0 \right) \underline{N}^*$ and $\underline{M} = \left(\underline{\underline{R}} \underline{\underline{R}}_0 \right) \underline{M}^*$ are the beam internal forces and moment resolved in the inertial basis, respectively. The virtual work done by external forces is expressed as $\delta W_{ext} = \int_0^L \left[\delta \underline{u}^T \underline{f} + \delta \underline{\psi}^T \underline{m} \right]$, where $\underline{f}$ and $\underline{m}$ are the externally applied forces and moments per unit span of the beam, respectively.

Now, the governing equations can be extended from static to dynamic problem by its kinetic energy and principle Hamilton's principle. First, the inertial velocity need to be determined by taking a time derivative of its inertial position vector, Equation (73), and it becomes,

$$\underline{v} = \dot{\underline{u}} + \dot{\underline{\underline{R}}} \underline{\underline{R}}_0 \underline{s}^* = \dot{\underline{u}} + \left(\underline{\underline{R}} \underline{\underline{R}}_0 \right) \tilde{\omega}^* \underline{s}^* = \dot{\underline{u}} + \left(\underline{\underline{R}} \underline{\underline{R}}_0 \right) \tilde{s}^{*T} \underline{\omega}^* \tag{80}$$

where $\underline{s}^{*T} = \{0, \alpha_2, \alpha_3\}$. Notation $(\dot{\bullet})$ indicates a derivative with respect to time and $\underline{\omega}^*$ are the components of the angular velocity in the material system, $\underline{\omega}^* = \left(\underline{\underline{R}} \underline{\underline{R}}_0 \right)^T \underline{\omega}$, where $\underline{\omega} = axial(\dot{\underline{\underline{R}}} \underline{\underline{R}}_0)$.

The components of the inertial velocity vector of a material point resolved in the material frame now becomes,

$$\underline{v}^* = \left(\underline{\underline{R}} \underline{\underline{R}}_0 \right)^T \underline{v} = \left(\underline{\underline{R}} \underline{\underline{R}}_0 \right)^T \dot{\underline{u}} + \tilde{s}^{*T} \underline{\omega}^* \tag{81}$$

The total inertial velocity of a material point has two components: the first term, $\left(\underline{\underline{R}} \underline{\underline{R}}_0 \right)^T \dot{\underline{u}}$, due to the translation of the cross-section, and the second term $\tilde{s}^{*T} \underline{\omega}^*$, due to its rotation.

The kinetic energy, *K*, of the beam is

$$K = \frac{1}{2} \int_0^L \int_A \rho \underline{v}^{*T} \underline{v}^* dA d\alpha_1 \tag{82}$$

where ρ is the mass density of the material per unit volume in the reference configuration. Substituting Equation (81) for the velocity yields,

$$K = \frac{1}{2}\int_0^L \int_A \rho \left[\underline{\dot{u}}^T \left(\underline{\underline{R}}\underline{\underline{R}}_0 \right) + \underline{\omega}^{*T} \tilde{\underline{s}}^* \right] \left[\left(\underline{\underline{R}}\underline{\underline{R}}_0 \right)^T \underline{\dot{u}} + \tilde{\underline{s}}^{*T} \underline{\omega}^* \right] dA d\alpha_1 \tag{83}$$

Define sectional mass constants as,

$$m = \int_A \rho dA, \quad \underline{\eta}^* = \frac{1}{m}\int_A \rho \underline{s}^* dA, \quad \underline{\underline{\zeta}}^* = \int_A \rho \tilde{\underline{s}}^* \tilde{\underline{s}}^{*T} dA \tag{84}$$

where *m* is the mass of the beam per unit span, $\underline{\eta}^*$ the components of the position vector of the sectional center of mass with respect to point **B**, and $\underline{\underline{\varrho}}^*$ the components of the sectional tensor of inertia per unit . span, resolved in material basis. The kinetic energy equation after integration over the beam's cross-section becomes

$$\begin{aligned} K &= \frac{1}{2}\int_0^L \left[m\underline{\dot{u}}^T \underline{\dot{u}} + 2m\underline{\dot{u}}^T \left(\underline{\underline{R}}\underline{\underline{R}}_0 \right) \tilde{\underline{\eta}}^{*T} \underline{\omega}^* + \underline{\omega}^{*T} \underline{\underline{\varrho}}^* \underline{\omega}^* \right] d\alpha_1 \\ &= \frac{1}{2}\int_0^L \underline{V}^{*T} \underline{\underline{\mathcal{M}}}^* \underline{V}^* d\alpha_1 \end{aligned} \tag{85}$$

where the sectional mass matrix of the cross-section, $\underline{\underline{\mathcal{M}}}^*$, resolved in the material basis is,

$$\underline{\underline{\mathcal{M}}}^* = \begin{bmatrix} m\underline{\underline{I}} & m\tilde{\underline{\eta}}^{*T} \\ m\tilde{\underline{\eta}}^* & \underline{\underline{\varrho}}^* \end{bmatrix} \tag{86}$$

And the sectional velocities, $\underline{V}^*$, resolved in the material basis, are defined as,

$$\underline{V}^* = \begin{Bmatrix} \left(\underline{\underline{R}}\underline{\underline{R}}_0 \right)^T \underline{\dot{u}} \\ \underline{\omega}^* \end{Bmatrix} = \begin{bmatrix} \left(\underline{\underline{R}}\underline{\underline{R}}_0 \right)^T & \underline{\underline{0}} \\ \underline{\underline{0}} & \left(\underline{\underline{R}}\underline{\underline{R}}_0 \right)^T \end{bmatrix} \begin{Bmatrix} \underline{\dot{u}} \\ \underline{\omega}^* \end{Bmatrix} = \left(\underline{\underline{\mathcal{R}}}\underline{\underline{\mathcal{R}}}_0 \right) \underline{V} \tag{87}$$

where $\underline{V}^T = \left\{ \underline{\dot{u}}^T \quad \underline{\omega}^T \right\}$. Then, the components of the sectional linear and angular momenta resolved in the material system, denoted $\underline{h}^*$ and $\underline{g}^*$, respectively are,

$$\underline{P}^* = \begin{Bmatrix} \underline{h}^* \\ \underline{g}^* \end{Bmatrix} = \underline{\underline{\mathcal{M}}}^* \underline{V}^* \tag{88}$$

Finally, the constitutive equation relate the sectional velocities to the momenta resolved in the inertial system, denoted $\underline{h}$ and $\underline{g}$ are,

$$\underline{P} = \begin{Bmatrix} \underline{h} \\ \underline{g} \end{Bmatrix} = \left(\underline{\underline{\mathcal{R}}} \underline{\underline{\mathcal{R}}}_0 \right) \underline{P}^* \Rightarrow \begin{Bmatrix} \underline{h} \\ \underline{g} \end{Bmatrix} = \underline{\underline{\mathcal{M}}} \begin{Bmatrix} \underline{\dot{u}} \\ \underline{\omega} \end{Bmatrix} \tag{89}$$

Variation of the kinetic energy is $\delta K = \int_0^L \delta \underline{V}^{*T} \underline{\underline{\mathcal{M}}} \delta \underline{V}^* d\alpha_1$, where the variation in velocities are $\delta \left[\underline{\dot{u}}^T \left(\underline{\underline{R}} \underline{\underline{R}}_0 \right) \right] = (\delta \underline{\dot{u}}^T + \delta \underline{\psi} \dot{\tilde{u}}^T) \left(\underline{\underline{R}} \underline{\underline{R}}_0 \right)$ and $\delta \underline{\omega}^{*T} = \delta \underline{\psi}^T \left(\underline{\underline{R}} \underline{\underline{R}}_0 \right)$. So the kinetic energy equation can be recast as,

$$\delta K = \int_0^L \left[(\delta \underline{\dot{u}}^T + \delta \underline{\psi} \dot{\tilde{u}}^T) \left(\underline{\underline{R}} \underline{\underline{R}}_0 \right) \underline{h}^* + \delta \underline{\psi}^T \left(\underline{\underline{R}} \underline{\underline{R}}_0 \right) \underline{g}^* \right] d\alpha_1 \tag{90}$$

Using Equation (89), the variation in kinetic energy can be expressed as,

$$\delta K = \int_0^L \left[(\delta \underline{\dot{u}}^T \underline{h} + \delta \underline{\psi}^T \dot{\tilde{u}}^T \underline{h} + \delta \underline{\psi}^T \underline{g} \right] d\alpha_1 \tag{91}$$

Using Equation (79) and (91) the governing equations of motions are obtained from Hamilton's principle, $\int_{t_0}^{t_f} \left[\delta W_{ext} + \delta K - \delta U \right] dt = 0$,where U is the elastic energy from left side of Equation (79). The equations of Hamilton's principle becomes,

$$\begin{aligned} &\int_{t_i}^{t_f} \int_0^L \left\{ \left(\delta \underline{\dot{u}}^T + \delta \underline{\psi}^T \dot{\tilde{u}}^T \right) \underline{h} + \delta \underline{\psi} \underline{g} - \left(\delta \underline{u}'^T + \delta \underline{\psi}^T \left(\tilde{x}_0' + \tilde{u}' \right) \right) \underline{N} \right. \\ &\left. - \delta \underline{\psi}'^T \underline{M} + \delta \underline{u}^T + \delta \underline{\psi}^T \underline{m} \right\} d\alpha_1 dt = 0 \end{aligned} \tag{92}$$

Integration by parts to yield the GEBT governing equations of motion,

$$\dot{h} - F' = f \tag{93}$$

$$\dot{g} + \dot{\tilde{u}} \underline{h} - M' + (\tilde{x}_0' + \tilde{u}_0')^T \underline{F} = \underline{m} \tag{94}$$

Finally a full mathematical description of a elasticity problem using GEBT is provided via Equation (65), (67), (80), (84) and (85).

Appendix C: *NAFNoise* Noise Code

The wind turbine noise predication part of WTNoise is carried by *NAFNoise*. It computes airfoil-self noise sources based on work from Brooks, Pope and Marcolini [17]. The results are used as inputs for a noise propagation model, which is presented in later sections.

The *NAFNoise* predicts the noise of any airfoil shape for five different types of airfoil self-noise: TBL-TE, separated flow noise, LBL-VS, TEB-VS, and turbulent inflow noise (TI). These noise models are also mentioned in Chapter 1.2 from work of Moriarty [21] and Table 2. The first four noise source are based on empirical models that originally developed by Brooks, Pope and Marcolini [17]. The turbulent inflow noise is predicted by an empirical model based on the work of Amiet [85]. However, the TI noise is not presented here due to the no turbulence inflow assumption in the numerical predictions. The formulation and implementation of the noise models in NAFNoise is out of scope of this study, but details can be found in [19, 21].

All five noise sources are assumed to be uncorrelated, i.e. each noise source independently generate their own noise signature. This is due to the idea of the mechanisms for each noise source is fundamentally different from each other. In addition, they may occur in different locations along a turbine blade, so that no interferences occur. Due to the uncorrelated noise source assumption, the total noise spectrum emitted from a wind turbine is computed by superimposing all the noise sources. The following subsections describes each noise source and its mechanism.

Turbulent Boundary Layer Tailing Edge Noise and Separated Flow Noise

TBL-TE noise is a common source of noise from an airfoil due to the interaction between the turbulent boundary layer and the trailing edge of the airfoil. In addition, it is the main source of high frequency noise. Airfoils develop a boundary layer over their surface and a transition from laminar to turbulent occurs at certain chord-wise position. The eddies in a turbulent boundary layer that is developed over a surface are inefficient sound sources. However, they become more efficient sources as they scatter on the trailing edge due to the shape edge in the vicinity. Thus, the trailing edge of an airfoil intensifies the noise level of the turbulences convecting along the airfoil. An illustration of TBL-TE noise is shown in Figure 100a. Trailing edge noise is perceived by people as a swishing sound. It is of broadband nature having the peak frequency typically in the range of 500 to 1500 Hz depending on the airfoil. The factors that influence trailing edge noise are the convection speed of the eddies and the structure of the boundary layer turbulence close to the edge. The exact shape of the trailing-edge is thought to be of importance only for relatively high frequencies (Wagner et al., 1996).

Mechanism of separated flow noise mainly depends on the angle of attack, α. As the angle of attack increases, the size of the turbulent boundary layer on the suction side of the airfoil increases. Stall conditions also occur at a certain point causing a substantial level of unsteady flow around the airfoil. At stall conditions, separated flow noise radiates from the unsteady flow over the entire chord of the airfoil and becomes the dominated noise source from trailing edge. Since wind turbine blades operate at a high angle of attack for significant portions of time, separated flow noise becomes critical. An illustration of separated flow noise is shown in Figure 100b.

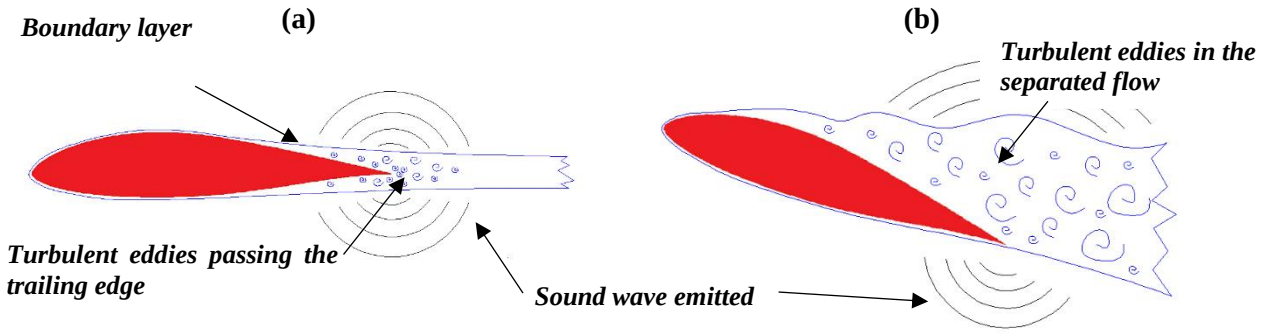

Figure 100: Illustration of **(a)** turbulent-boundary-layer—trailing-edge noise and **(b)** separated flow noise

TBL-TE and SF noise were both assumed to be caused by turbulent effects. Brooks et al. (1989) approach was to model these noise mechanisms individually. Therefore, the total sound pressure level (SPL) from the interaction of the turbulent boundary layer with trailing edge is determined through summation of three noise components: pressure side, suction side, and separated flow.

Laminar Boundary Layer Vortex Shedding Noise (LBL-VS)

For an airfoil that operates at relatively low Reynolds numbers, the laminar flow regions may extend to the trailing edge. A resonant interaction of the trailing edge noise with the unstable laminar-turbulent transition can then occur. An upstream traveling acoustic wave couples with the instabilities resulting in tonal noise. The aforementioned instabilities can lead to separation bubbles generating noise. High levels of noise can occur if the instabilities are triggered by the acoustic field and vice versa [20]. This interaction is schematically represented in Figure 101. The LBL-VS noise most likely occur on the pressure side of the airfoil and is tonal noise in nature.

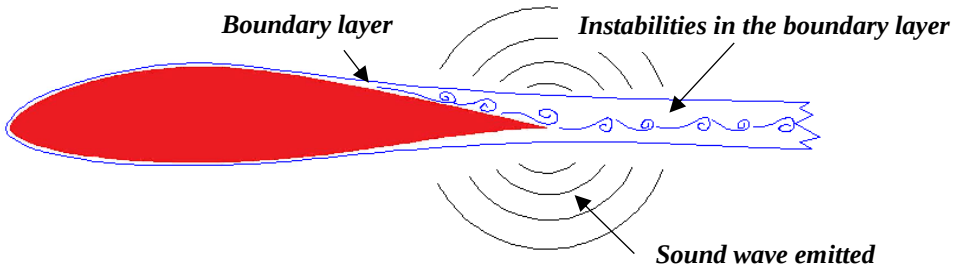

Figure 101: Illustration of laminar-boundary-layer—vortex-shedding noise.

Trailing Edge Bluntness Vortex Shedding Noise (TEB-VS)

This noise mechanism is based on the noise emission by von Karman type vortex shedding from the trailing edge. The frequency and amplitude are also determined by the geometry of the trailing edge. The alternating vortices produces pressure fluctuations in the trailing edge zone as shown in Figure 102a. According to Wagner, TEB-VE noise source will dominate the total radiated noise if the thickness of the trailing edge is significantly larger than the thickness of the boundary layer at the trailing edge [20]. The frequency of the spike originated depends on the flow conditions, the trailing edge thickness, *b*, and displacement thickness ratio, b/δ^* . The smaller the trailing edge thickness to displacement thickness ratio the higher is the shedding frequency. Therefore, if the trailing edge is sharp enough, the spike will be displaced to high frequency region in which noise is not audible for humans. As consequences, the empirical relation to predict SPL of TEB-VS also contains functions dependent on the trailing edge thickness.

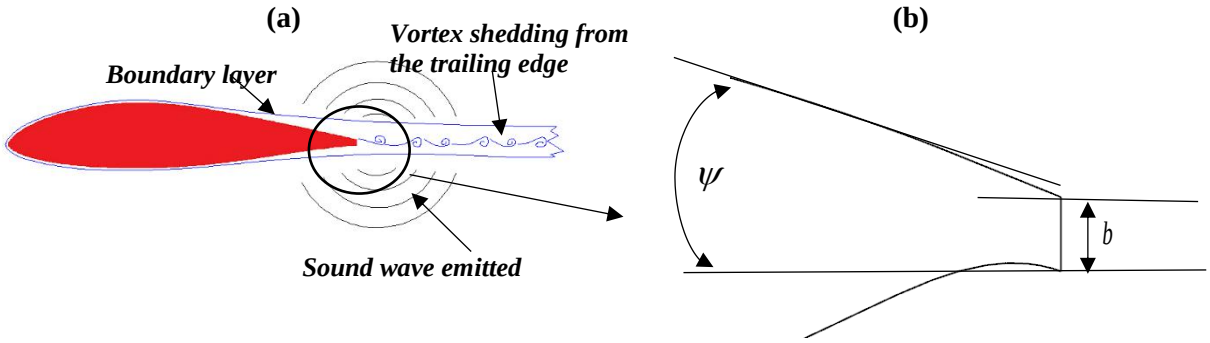

Figure 102: (a) Illustration of trailing-edge-bluntness—vortex-shedding noise. **(b)** Schematic view of trailing edge of a flatback airfoil. ***b*** is the trailing edge thickness. ψ is the angle between airfoil pressure and suction side.

Directivity

The directivity functions in the empirical noise models are presented here. They are function of directivity angles and account for the attenuation or amplification produced by the convective effect depending on the direction of propagation considered. Furthermore, there are two directivity functions based on the acoustic wavelengths. An important aspect in the understanding of the noise emitted by wind turbines is the radiation directivity characteristics of trailing edge noise. This noise is usually modeled as a dipole source located at the trailing edge [86, 87]. The trailing edge noise emission behaves as a baffled dipole when the acoustic wavelengths are much shorter than the chord length of the airfoil. When the acoustic wavelengths are comparable to the airfoil's chord, the noise emitted follows a pure dipole directivity behavior [17]. Equations describing the baffled-dipole and pure-dipole directivities were presented in the work of Brooks et al. (1989). Note that noise sources of TBL-TE, LBL-VS, TEB-VS and separated flow are assumed to originate at the trailing edge of the airfoil and have baffled-dipole behaviors.

Appendix D: The NREL Blade Properties

Table 12: NREL 5-MW blade airfoil and chore properties used in *AeroDyn* [54].

Blade Span (m)	***Blade Twist, deg***	***Blade Chord, m***	***Airfoil***
0.000	13.308	3.542	Cylinder_1
1.367	13.308	3.542	Cylinder_1
4.100	13.308	3.854	Cylinder_1
6.833	13.308	4.167	Cylinder_2
10.25	13.308	4.557	DU99-W-405
14.35	11.48	4.652	DU99-W-350
18.45	10.162	4.458	DU99-W-350
22.55	9.011	4.249	DU97-W-300
26.65	7.795	4.007	DU91-W2-250
30.75	6.544	3.748	DU91-W2-250
34.85	5.361	3.502	DU93-W-210
38.95	4.188	3.256	DU93-W-210
43.05	3.125	3.010	NACA-64-618
47.15	2.319	2.764	NACA-64-618
51.25	1.526	2.518	NACA-64-618
54.67	0.863	2.313	NACA-64-618
57.40	0.37	2.086	NACA-64-618
60.13	0.106	1.419	NACA-64-618
61.50	0	1.419	NACA-64-618

Table 13: NREL 5-MW blade structure properties used in BeamDyn [54].

Blade Span	***Structural Twist***	m	i_{Edg}	i_{Flp}	EA	K_{Edg}	K_{Flp}	GJ
(m)	Degree °	*kg/m*	*kg·m*	*kg·m*	$N{\cdot}m^2$	$N{\cdot}m^2$	$N{\cdot}m^2$	*N*
0.000	13.308	678.94	973.04	972.86	9729.48E+6	1.81E+10	1.81E+10	5.564E+09
1.200	13.308	773.36	1066.38	1091.52	1.08E+10	1.96E+10	1.94E+10	5.432E+09
3.200	13.308	740.04	1099.75	873.81	9.87E+09	1.98E+10	1.53E+10	4.667E+09
5.200	13.308	450.28	641.49	456.76	5.49E+09	1.02E+10	7.23E+09	2.324E+09
7.200	13.308	400.64	547.18	351.61	4.49E+09	8.06E+09	5.53E+09	1.570E+09
9.200	13.308	399.66	503.86	303.60	4.04E+09	7.01E+09	4.94E+09	1.002E+09
11.200	13.181	416.82	569.90	246.57	4.08E+09	7.27E+09	3.95E+09	6.723E+08
13.201	12.192	381.42	546.56	187.11	3.67E+09	6.24E+09	2.93E+09	4.488E+08
15.200	11.072	349.48	453.76	148.56	3.01E+09	4.95E+09	2.39E+09	3.114E+08
18.201	10.232	339.33	398.18	124.61	2.61E+09	4.50E+09	2.05E+09	2.610E+08
22.200	9.110	321.99	335.01	94.36	2.15E+09	4.00E+09	1.59E+09	2.008E+08
26.200	7.932	294.73	263.87	62.67	1.63E+09	3.45E+09	1.10E+09	1.445E+08
30.200	6.711	263.34	196.41	37.34	1.17E+09	2.73E+09	6.81E+08	8.119E+07
34.200	5.546	241.67	162.43	22.16	9.23E+08	2.33E+09	4.09E+08	5.745E+07
38.201	4.401	200.29	116.30	13.30	6.48E+08	1.58E+09	2.39E+08	3.598E+07
42.200	3.320	165.09	98.93	7.30	5.31E+08	1.18E+09	1.26E+08	2.090E+07
46.200	2.503	138.94	69.96	5.19	3.76E+08	7.98E+08	9.09E+07	1.628E+07
50.200	1.730	107.26	45.44	3.36	2.44E+08	5.18E+08	6.11E+07	9.070E+06
54.200	0.954	90.25	34.09	2.11	1.82E+08	3.95E+08	3.94E+07	7.080E+06
56.200	0.574	72.91	20.15	1.69	1.09E+08	3.05E+08	3.04E+07	5.750E+06
57.700	0.319	66.26	17.11	1.34	9.22E+07	2.62E+08	2.38E+07	4.940E+06
58.700	0.216	55.91	9.77	0.89	5.33E+07	1.38E+08	1.60E+07	3.660E+06
59.700	0.140	49.11	6.82	0.56	3.69E+07	1.02E+08	1.01E+07	2.640E+06
60.700	0.062	41.64	4.01	0.25	2.13E+07	6.43E+07	4.60E+06	1.580E+06
61.50	0	10.32	0.680	0.020	3.530e6	5.010e6	0.170e6	0.190e6

**See Equation 49 and 50 for the properties definitions*

Appendix E: The SNL100-02 Blade Properties

Table 14: SNL100-02 blade airfoil and chore properties used in *AeroDyn* [74].

Blade Span (m)	*Blade Twist, deg*	*Blade Chord, m*	*Airfoil*
0.00	13.308	5.694	Cylinder
0.50	13.308	5.694	Cylinder
0.70	13.308	5.694	Transition
0.90	13.308	5.694	Transition
1.10	13.308	5.694	Transition
1.30	13.308	5.694	Ellipse
2.40	13.308	5.792	Ellipse
2.60	13.308	5.811	Ellipse
4.70	13.308	6.058	Transition
6.80	13.308	6.304	Transition
8.90	13.308	6.551	Transition
11.40	13.308	6.835	Transition
14.60	13.308	7.215	Transition
16.30	13.177	7.404	Transition
17.90	13.046	7.552	Transition
19.50	12.915	7.628	DU99-W-405
22.20	12.133	7.585	DU99-W-405
24.90	11.350	7.488	DU99-W-350
27.60	10.596	7.347	DU99-W-350
35.80	9.166	6.923	DU97-W-300
43.90	7.688	6.429	DU91-W2-250
52.00	6.180	5.915	DU93-W-210
60.20	4.743	5.417	DU93-W-210
66.70	3.633	5.019	NACA-64-618
68.30	3.383	4.920	NACA-64-618
73.20	2.735	4.621	NACA-64-618
76.40	2.348	4.422	NACA-64-618
84.60	1.380	3.925	NACA-64-618
89.40	0.799	3.619	NACA-64-618
94.30	0.280	2.824	NACA-64-618
95.70	0.210	2.375	NACA-64-618
97.20	0.140	1.836	NACA-64-618
98.60	0.070	1.208	NACA-64-618
100.00	0.000	0.100	NACA-64-618

Table 15: SNL100-02 blade structure properties used in *BeamDyn* [74].

Blade Span	***Structural Twist***	m	i_{Edg}	i_{Flp}	EA	K_{Edg}	K_{Flp}	GJ
(m)	*Degree °*	*kg/m*	*kg·m*	*kg·m*	$N{\cdot}m^2$	$N{\cdot}m^2$	$N{\cdot}m^2$	*N*
0.000	13.308	3600	14070.0	14260.0	5.31E+10	2.07E+11	2.10E+11	1.08E+11
0.500	13.308	2970	11680.0	11850.0	4.38E+10	1.72E+11	1.75E+11	8.98E+10
0.700	13.308	2596	10220.0	10270.0	3.83E+10	1.50E+11	1.53E+11	7.80E+10
0.900	13.308	2223	8767.0	8710.0	3.27E+10	1.28E+11	1.29E+11	6.63E+10
1.100	13.308	1854	7318.0	7204.0	2.74E+10	1.06E+11	1.08E+11	5.48E+10
1.300	13.308	1692	6646.0	6525.0	2.55E+10	9.62E+10	1.02E+11	4.96E+10
2.400	13.308	1744	6306.0	6262.0	2.48E+10	9.06E+10	9.56E+10	4.53E+10
2.600	13.308	1628	5860.0	5815.0	2.28E+10	8.32E+10	8.81E+10	4.14E+10
4.700	13.308	1601	6021.0	5269.0	2.24E+10	8.32E+10	8.10E+10	3.84E+10
6.800	13.308	1612	6400.0	4847.0	2.34E+10	8.79E+10	7.91E+10	3.71E+10
8.900	13.308	1365	5909.0	3481.0	2.17E+10	8.19E+10	6.72E+10	2.67E+10
11.400	13.308	1195	5331.0	2577.0	2.09E+10	7.35E+10	5.74E+10	1.99E+10
14.600	13.308	780.5	3233.0	1345.0	1.80E+10	4.13E+10	4.68E+10	6.88E+10
16.300	13.177	765	3301.0	1112.0	1.80E+10	4.35E+10	4.04E+10	5.66E+09
17.900	13.046	747.3	3196.0	929.4	1.87E+10	4.12E+10	3.64E+10	4.39E+09
19.500	12.915	750.3	3140.0	811.6	2.05E+10	4.07E+10	3.54E+10	3.38E+09
22.200	12.133	735.4	3042.0	695.7	2.03E+10	3.98E+10	3.06E+10	2.96E+09
24.900	11.350	710.8	2845.0	581.7	2.02E+10	3.78E+10	2.63E+10	2.47E+09
27.600	10.596	672.7	2537.0	476.9	1.89E+10	3.22E+10	2.13E+10	2.08E+09
35.800	9.166	624.9	2065.0	305.9	1.85E+10	2.70E+10	1.44E+10	1.34E+09
43.900	7.688	522.2	1257.0	188.5	1.74E+10	1.40E+10	9.43E+09	8.13E+08
52.000	6.180	479.8	940.3	118.5	1.70E+10	1.09E+10	6.12E+09	5.18E+08
60.200	4.743	433.9	701.8	74.5	1.58E+10	8.41E+09	3.91E+09	3.30E+08
66.700	3.633	388	539.2	47.5	1.47E+10	6.62E+09	2.49E+09	2.18E+08
68.300	3.383	372.3	505.5	41.1	1.38E+10	6.21E+09	2.12E+09	1.95E+08
73.200	2.735	337	416.1	30.5	1.19E+10	5.13E+09	1.53E+09	1.52E+08
76.400	2.348	292.2	351.1	23.9	9.17E+09	4.40E+09	1.08E+09	1.36E+08
84.600	1.380	221.6	231.8	13.7	5.47E+09	2.96E+09	4.90E+08	9.74E+07
89.400	0.799	195.2	178.7	10.1	4.45E+09	2.30E+09	3.30E+08	7.68E+07
94.300	0.280	147.3	85.1	4.5	3.17E+09	1.11E+09	1.37E+08	3.67E+07
95.700	0.210	111	48.6	2.5	2.60E+09	6.55E+08	7.96E+07	2.14E+07
97.200	0.140	85.79	22.4	1.1	2.01E+09	3.02E+08	3.58E+07	9.57E+06
98.600	0.070	56.44	6.4	0.3	1.32E+09	8.58E+07	9.53E+06	2.53E+06
100.000	0.000	4.672	0.0	0.0	1.09E+08	4.45E+04	3.32E+03	1.16E+03

**See Equation 49 and 50 for the properties definitions*